Direction-of-arrival Estimation of Wideband Sources Using Sensor Arrays

A Thesis
Presented to
The Academic Faculty

by

Yeo-Sun Yoon

In Partial Fulfillment
of the Requirements for the Degree
Doctor of Philosophy

School of Electrical and Computer Engineering
Georgia Institute of Technology
July 2004

Direction-of-arrival Estimation of Wideband Sources Using Sensor Arrays

Approved by:

Dr. James H. McClellan, Adviser

Dr. Lance M. Kaplan

Dr. Douglas B. Williams

Date Approved: 9 July 2004

To my family.

My father and mother.

Especially, to my beloved wife Ji-Hyun

and my precious Catherine.

ACKNOWLEDGEMENTS

When I came to Georgia Tech, I used to imagine the moment when I graduate and thought that it would take forever to finish my graduate work. Since then, five years passed fast and I have finished my thesis. While I was writing this thesis, I could not help thinking that it would not be possible to finish my PhD work if it were not for help from my family, my advisors and my friends. I owe them everything that I could have done during my years at Georgia Tech.

First of all, I'd like to thank my advisor Prof. James McClellan. He is not only the best advisor that I have seen but also a role model as a researcher and a teacher to me. His intuition to see and solve a problem was amazing to me and it was a big pleasure to be advised by him. Prof. Lance Kaplan, my co-advisor, was always there to help me when I was in trouble or when I don't know what to do. He was always willing to help me and waited for me patiently until I found solutions by myself. Thank you, Dr. Kaplan. I also would like to thank the other committee members: Prof. Douglas Williams, Prof. Waymond Scott Jr., and Prof. Guillermo Goldsztein for all of their support.

When I worked at the Center for Signal and Image Processing (CSIP) of Georgia Tech, I was lucky enough to have all those good colleagues. Volkan Cevher. I used to share hotel rooms with him whenever we went to conference. Mubashir Alam. He helped me a lot for acoustic data processing. Sam Li. He always smiled at me and was willing to help me. Matt Cobb. I used his program in the first work that I did here. Seung-mok Oh. He and I graduated from same undergraduate school in Korea. He helped me in everything when I settle down. Sometimes, I used to waste his time by asking a favor. I'd like to thank him here. Greg Showman, Qiang Le, Rajbabu

Velmurugan, Ryan Hersey, Suhow Lim, and Ali Cafer Gurbuz. Thank you for your friendship and good luck on your research.

I feel kind of sorry that I cannot say more than 'thank you' to my parents. They supported me in every way and gave me a chance to study at Georgia Tech.

I give my special thank to my wife, Ji-Hyun. She is not only my lovely wife but also my friend, a best mother to Catherine, and everything. I would say that the PhD degree is earned by her, not me.

I wish I could say everyone's name here who helped me while I was staying at Atlanta. The reason why I cannot do that is that I needed help from so many people due to my lack of ability.

TABLE OF CONTENTS

LIST OF TABLES

LIST OF FIGURES

LIST OF SYMBOLS OR ABBREVIATIONS

CSSM Coherent Signal Subspace Method.

DFT Discrete Fourier Transform.

DOA Direction-Of-Arrival.

EVD Eigenvalue Decomposition.

FOV Field of View.

IMUSIC Incoherent MUSIC method.

MLE Maximum Likelihood Estimator.

MUSIC Multiple Signal Classification.

PFB Pruned Fast Beamformer.

RMS Root Mean Square.

SNR Signal to Noise Ratio.

SVD Singular Value Decomposition.

TOPS Test of Orthogonality of Projected Subspaces.

ULA Uniform Linear Array.

UWB Ultra Wideband.

WAVES Weighted Average of Signal subspaces.

SUMMARY

Sensor arrays are used in many applications where their ability to localize signal sources is essential. For many applications, it is necessary to estimate the direction-of-arrival (DOA) of target sources. Although there are many DOA estimation methods available, most of them are valid only for narrowband signals where time delay can be approximated as a phase shift. This thesis focuses on DOA estimation algorithms for wideband sources. Specifically, this thesis proposes the pruned fast beamformer which can reduce the number of computations of Delay-and-Sum (DS) beamforming by using a multi-resolution structure. For high resolution methods, signal subspace methods are required. Most of the subspace techniques for wideband signals decompose the received wideband signals into several bands of narrowband signals through bandpass filtering. Then, there are two different ways of processing decomposed signals. The incoherent methods process each band independently by a given narrowband method and average the results. The coherent methods attempt to modulate the signals in each band so that they can be combined coherently. In this thesis, a new DOA estimator, which is called TOPS, is developed to avoid disadvantages of both the incoherent and the coherent methods. The new method which can be categorized as a non-coherent method is tested and compared with other methods. It exhibits many desirable features for a number of applications where the sources are wideband such as acoustic direction finding.

CHAPTER 1

INTRODUCTION

1.1 Objective and Contributions of this Work

The ability to transmit and/or receive information without a physical connection between two locations is very attractive in many applications. Information can be delivered via electromagnetic, sonar, acoustic, or seismic waves. The military has a need to detect and recognize enemy objects by receiving signals emitted from those objects. Radar, which is one of those applications, is prevalent for both military and civilian purposes. Wireless communication is another application which is a very active research field. As the applications become more complicated, they require processing of more signals, more data, and/or more robustness which is beyond the capability of single sensor communications.

For many years, systems with multiple sensors have been used to receive or send signals through a wireless channel [24]. Sensor array systems have several advantages over single sensor systems. First, they can increase the signal-to-noise ratio (SNR) up to M times greater than single sensor systems by appropriate processing of the received signals where M is the number of sensors. Second, sensor arrays can steer the transmitting or receiving beams and by doing that, they can separate multiple signals. This is very useful in applications such as multi-user wireless communications which require the processing of as many signals as possible without mutual interference, or passive radar applications which need to localize signal source locations.

Direction of arrival (DOA) is one of the most important parameters that needs to be estimated in most applications. For radar, DOA estimation is the most important factor to localize targets. For communications, DOA estimation can give spatial

diversity to the receiver to enable multi-user scenarios. There are a large number of algorithms for DOA estimation because of its importance in array signal processing. Signal subspace methods are very well known as DOA estimation methods with high performance and relatively low computational cost. MUSIC (MUltiple Signal Classification) [41] and ESPRIT [40] fall into this category. Most of these methods take advantage of the fact that there is only a phase difference between sensor outputs, when the signals are narrowband. Therefore, the subspace methods work exclusively with narrowband signals. Recently, wideband signals have received more attention because they are replacing narrowband signals in many applications. For example, ultra wideband (UWB) radar can provide high resolution images [23] and UWB wireless communication can reduce channel fading from the multipath effect [62]. Wideband signals are also used to track moving objects from acoustic measurements [31] or to find buried objects through seismic sensors [33].

Due to the bandwidth limit of conventional signal subspace methods, some processing should be performed before narrowband techniques are applied or a special method for wideband signals should be applied [2, 8, 37, 49]. We can apply narrowband methods if the wideband signals are decomposed into multiple narrowband signals [61]. When narrowband methods are applied independently to the multiple signals, these types of approaches are called *incoherent methods*. Other than incoherent methods, many approaches have been published regarding wideband DOA estimation [2, 12, 32, 51, 53, 54, 58]. These methods are called *coherent methods* since they use all the frequency components of a wideband signal coherently. Most of these methods involve converting wideband data or statistics into narrowband forms, either directly or indirectly, so that the narrowband subspace methods can be applied. One of the most well-known coherent methods is the coherent signal subspace method (CSSM) [58] from which many methods derive their roots [12, 32]. CSSM requires a preprocessing step called *focusing*. The focusing step requires an initial estimates of

the DOAs which should be as close as possible to the true DOAs. If the initial values are different from the true DOAs, the estimation could be biased even if the number of data samples approaches infinity [51].

In this thesis, two methods for wideband sources are proposed. First, a new fast delay-and-sum (DS) beamforming method is proposed which reduces the computational cost of a DS beamformer by introducing a signal detector. A DS beamformer can also be used for DOA estimation since the power of a beam toward the DOAs would be higher than from other directions. Furthermore, it can deal with wideband signals as well as narrowband signals. The fast beamforming method is an approximation of a DS beamformer with fewer computations [34], which was originally proposed for Synthetic Aperture Radar (SAR) imaging [35]. The fast pruned beamformer is a method that can reduce the number of computations even more by pruning the directions where there are no target-like signals [68] similar to [26].

Second, a new wideband DOA estimator, called TOPS (Test of Orthogonality of Multiple Projected Signal subspace Over Noise subspace), is proposed. TOPS is different from the wideband incoherent methods because it uses multiple frequency bins all at the same time while the incoherent methods use those frequency bins independently. This can avoid inconsistencies in the independent results from multiple frequency bins, which is usually seen in incoherent methods. TOPS also differs from the coherent methods since there is no coherent combination of the data. This means that it does not require focusing angles that might introduce error in the process of data conversion. It is shown that the performance of the new method is best in the mid-SNR range while coherent methods work best in the low-SNR range and incoherent methods work best in the high-SNR range.

The two methods in this thesis are believed to bridge the gap between incoherent and coherent methods. They provide new approaches to solve problems that deal with wideband signals, and they avoid many of the disadvantages of the traditional

incoherent and coherent methods

1.2 Organization of the Thesis

The organization of the thesis is as follows. In Chapter 2, the basics of array signal processing are introduced. Propagating wave fields and sensor arrays are discussed as well as narrowband signal models and wideband signal models which distinguish the wideband methods from narrowband methods.

In Chapter 3, some array signal processing methods for both narrowband and wideband signals are explained. Although the methods explained in this chapter are just a small part of array signal processing, the difference between dealing with narrowband and wideband signals is elucidated.

In Chapter 4, fast pruned beamforming, a new beamforming method which adds a signal detector to the fast beamforming method in [34], is introduced as a low-resolution DOA estimator. First, the structure of the fast DS beamforming method is derived. Then, the new pruned fast beamforming method is introduced followed by simulation results and an error analysis.

The new wideband DOA estimator, TOPS, is introduced in Chapter 5. The basic theory and the extension of the new method are discussed. The differences between TOPS and previous incoherent and coherent methods are described in this chapter followed by an analysis of the new method in Chapter 6.

Chapter 7 presents the results of computer simulations and experiments. For a complete comparison of the new methods with others, many different scenarios are considered. The performance of the estimators is summarized and discussed.

Chapter 8 shows the applicability of TOPS to an application involving seismic waves. Detection of landmines is processed using TOPS.

Finally, Chapter 9 concludes this thesis with contributions and future work.

CHAPTER 2

BASIC BACKGROUND

The basic background of array signal processing is briefly discussed in this chapter. First, the propagating scalar field is explained, then, sensor arrays are discussed. In the third section, the array signal models for narrowband signals and wideband signals are compared. These models suggest why two different DOA estimation methods are required depending on the signal's bandwidth.

2.1 Propagating Waves

2.1.1 Space-Time Representation

Propagating waves are a function of both time and space. According to physics, they can be described as solutions to the wave equation [24]. The wave equation for an electromagnetic field is derived from Maxwell's equation.

$$\nabla^2 \vec{E} = \frac{1}{c^2} \frac{\partial^2 \vec{E}}{\partial t^2},$$

where $\vec{E}$ is the electric field intensity, c is the speed of propagation, and ∇^2 is the Laplacian operator

$$\nabla^2 = \frac{\partial^2}{\partial x^2} + \frac{\partial^2}{\partial y^2} + \frac{\partial^2}{\partial z^2}.$$

Let $\vec{r} = (x, y, z)$ be a position vector where each of three elements represents position along one of the three spatial axis. After plugging in $s(\vec{x}, t)$ representing a general scalar field, the wave equation becomes

$$\frac{\partial^2 s}{\partial x^2} + \frac{\partial^2 s}{\partial y^2} + \frac{\partial^2 s}{\partial z^2} = \frac{1}{c^2} \frac{\partial^2 s}{\partial t^2}. \tag{1}$$

The solution to the partial differential equation (1) is usually assumed to be a complex exponential such as

$$s(\vec{x},t) = s(x,y,z,t) = A\exp\left\{j(\omega t - k_x x - k_y y - k_z z)\right\}. \tag{2}$$

If we plug in (2) to (1), we obtain the following relationship between constants.

$$k_x^2 + k_y^2 + k_z^2 = \frac{\omega^2}{c^2}. \tag{3}$$

If Equation (3) is satisfied, the complex exponential of (2) is a solution of the wave equation. The solution can be rewritten using vector notation and inner product.

$$s(\vec{x},t) = A\exp\left\{j(\omega t - \vec{k}\cdot\vec{r})\right\}, \tag{4}$$

where $\vec{k} = (k_x, k_y, k_z)$ is called a *wavenumber* vector and the exponential is called a monochromatic plane wave. A scalar field can be expressed in terms of plane waves of multiple frequencies by [24]

$$s(\vec{x},t) = \frac{1}{2\pi}\int_{-\infty}^{\infty} S(\omega)\exp\left\{j(\omega t - \vec{k}\cdot\vec{r})\right\} d\omega.$$

This is the space-time representation of the propagating waves. The distance propagated during one temporal period T is denoted by the *wavelength* λ. That is,

$$\lambda = cT = c\frac{2\pi}{\omega}.$$

Since $\left|\vec{k}\right| = \omega/c$ in (3), the wavelength λ is also represented as

$$\lambda = \frac{2\pi}{\left|\vec{k}\right|}.$$

The phase term in the solution (4) can be rewritten as

$$j(\omega t - \vec{k}\cdot\vec{r}) = j\omega(t - \vec{\alpha}\cdot\vec{r}). \tag{5}$$

Usually, the direction and the speed of the propagation are defined by a vector $\vec{\alpha}$ in (5) which is called the *slowness* vector $\vec{\alpha}$. It can be easily shown from (3) and

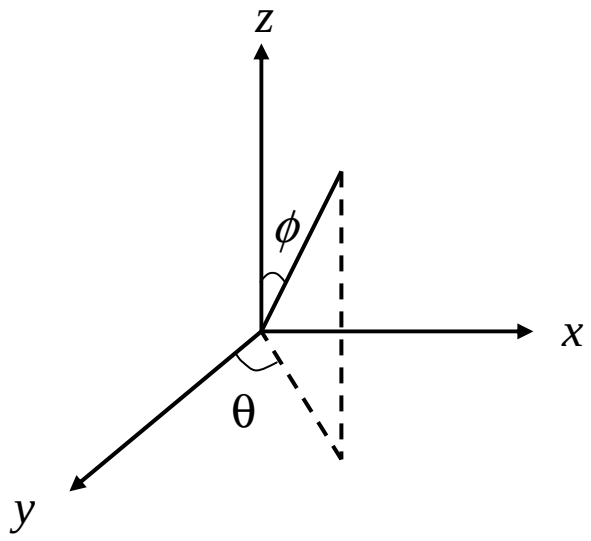

Figure 1: Coordinate of array and signal direction

(5) that the magnitude of $\vec{\alpha}$ is the inverse of the speed of the propagation. If we use spatial coordinate as in Fig. 1, the slowness vector is

$$\vec{\alpha} = \frac{1}{c}(\sin\theta\sin\phi, \cos\theta\sin\phi, \cos\phi), \tag{6}$$

where c is the speed of the propagation, θ is the azimuth angle, and ϕ is the elevation angle. Once we can estimate the slowness vector, we can also estimate the direction of propagation or the speed of propagation, not both. The space-time representation of a propagating signal using the slowness vector is

$$s(\vec{x}, t) = s(t - \vec{\alpha}\cdot\vec{r}) = \frac{1}{2\pi}\int_{-\infty}^{\infty} S(\omega)\exp\left\{j\omega(t - \vec{\alpha}\cdot\vec{r})\right\} d\omega, \tag{7}$$

where $S(\omega)$ is the Fourier transform of $s(\cdot)$.

2.1.2 $\omega - k$ Representation

Propagating signals can be represented also in the wavenumber-frequency $(\omega - k)$ space after taking the Fourier transform of the space-time representation. Since the array signal is function of not only time but also space, a multidimensional Fourier

transform is required. The four-dimensional (x, y, z, t) Fourier transform of space-time signal is,

$$S(\vec{k}, \omega) = \iint s(\vec{r}, t) e^{-j\omega t} e^{j\vec{r}\cdot\vec{k}} dt d\vec{r}. \tag{8}$$

The wave field on the x-axis, $\vec{r} = (x, 0, 0)$, is

$$S(k_x, \omega) = \iint s(x, t) e^{-j\omega t} e^{jxk_x} dt dx.$$

2.2 Sensor Arrays

Sensor arrays consist of multiple sensors which are located at different points in space. The propagating signals are simultaneously sampled and recorded for all sensors. In other words, the array signal is a propagating signal sampled both spatially and temporally by the sensor array. The signal received at the m-th sensor can be represented as (7) where $\vec{r}$ is replaced with $\vec{r}_m$ which denotes the sensor location. When there are P sources travelling from P different directions and the sensor response is assumed to be one, the output of the m-th sensor is

$$x_m(t) = \sum_{i=0}^{P-1} s_i(t - \vec{r}_m \cdot \vec{\alpha}_i) + \eta_m(t) \tag{9}$$

where $\eta_m(t)$ is additive noise at the m-th sensor. The additive noise $\eta_m(t)$ is usually assumed to be uncorrelated with the sources and both temporally and spatially white. If the noise is not white, but the covariance is known, we can deal with noise by whitening. The speed of propagation c is typically 3×10^8 m/s for electromagnetic waves or 344 m/s for outdoor acoustics. The received signal at each sensor is nothing but the sum of P sources which are delayed differently. From receiver point of view, the parameters to be estimated are usually the number of sources P, the source signals $s_i(t)$, the azimuth angle θ, and the elevation angle ϕ. Estimation of P is quite different from estimation of the DOAs (θ or ϕ). The main objective of this thesis is to estimate θ and ϕ. This implies that the number of sources P is assumed to be known or correctly estimated except in Chapter 6 where the effect of an incorrectly

estimated number of signals is discussed. It is also assumed that the sensor locations are calibrated without any error. However, it is not always possible to estimate the two parameters θ and ϕ uniquely. Depending on the array geometry, signals with the same propagation speed but different directions might appear to be the same. The set of directions that the array is unable to distinguish is called the ambiguity set [24].

If the sensors are linearly placed (see Fig. 2(a)), only the x component of the slowness vector will influence the sensor output. In this case, given the azimuth angle θ, there is an ambiguity set around the arrays like a cone whose center is along the array. Due to this ambiguity surface, the elevation angle cannot be uniquely determined with linear arrays and the range of azimuth angles is limited to the half space $(-\pi/2, \pi/2]$. For planar arrays, it is possible to find both the x and y components of the slowness vector. Since the magnitude of the slowness vector is fixed, we can find the third component. However, since we still do not know the sign of the z component, there is ambiguity with respect to the z axis. For 3D arrays, however, both the azimuth and the elevation angle can be determined uniquely. In this thesis, linear arrays will be considered in most cases and they will be assumed to be located on the x-axis. Therefore, the range of DOA is limited within a half-plane to ($-\pi/2$ to $\pi/2$]. Extension to multidimensional arrays will be straightforward.

2.3 Signal Models

The bandwidth of signal is defined as the range of temporal frequency where the signal's power is nonzero. Signals which have only one passband are called bandpass signal (See Fig. 3). According to the fractional bandwidth, which is the ratio of the bandwidth to the central frequency, the signal is either a narrowband signal or a wideband signal. The fractional bandwidth of the received signal is very important because the received signal must be modelled differently depending on this quantity.

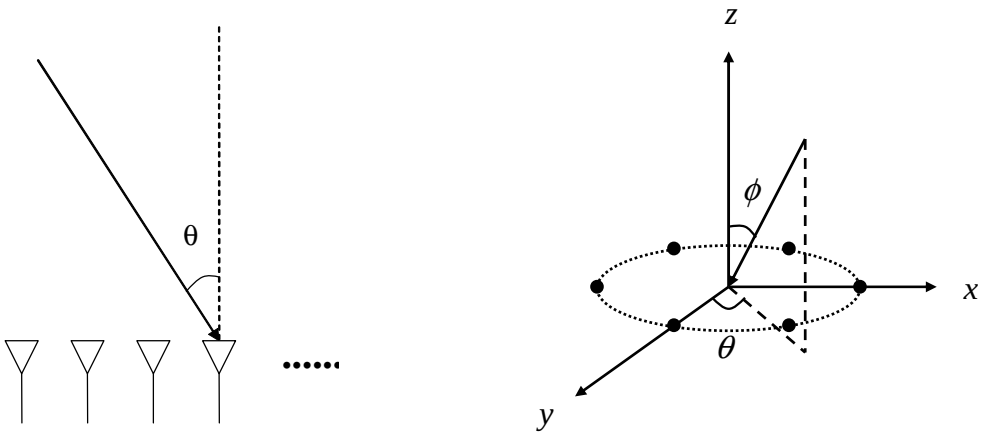

(a) Linear array (b) Circular array

Figure 2: Sensor array examples

In this chapter, the role of bandwidth in array signal processing is explained. A large portion of this chapter is adapted from the book by Stoica and Moses [45]. Let's redefine the m-th sensor output x_m here for the single source case.

$$x_m(t) = h_m(t) * s(t - \tau_m) + \eta_m(t) \tag{10}$$

where $h_m(t)$ is the impulse response of the m-th sensor and $(*)$ denotes convolution. The model (9) in the previous section is the special case where $h_m(t) = 1$. The source signal $s(t)$ is usually a modulated signal formed from the function $b(t)$ which is a baseband signal. If $s(t)$ is a real function, the power spectral density of $s(t)$ is symmetric about $\omega = 0$ as in Fig. 3. The frequency domain representation of (10) is

$$X_m(\omega) = H_m(\omega)[B(\omega - \omega_c) + B^*(-\omega - \omega_c)]e^{-j\omega\tau_m} + N_m(\omega) \tag{11}$$

where $N_m(\omega)$ is the Fourier transform of $\eta_m(t)$. Let $\tilde{x}_m(t)$ be the demodulated signal obtained from $x_m(t)$ as in

$$\tilde{x}_m(t) = x_m(t)e^{-j\omega_c t}.$$

The Fourier transform of the demodulated signal is

$$\tilde{X}_m(\omega) = H_m(\omega + \omega_c)[B(\omega) + B^*(\omega - 2\omega_c)]e^{-j(\omega+\omega_c)\tau_m} + N_m(\omega + \omega_c). \tag{12}$$

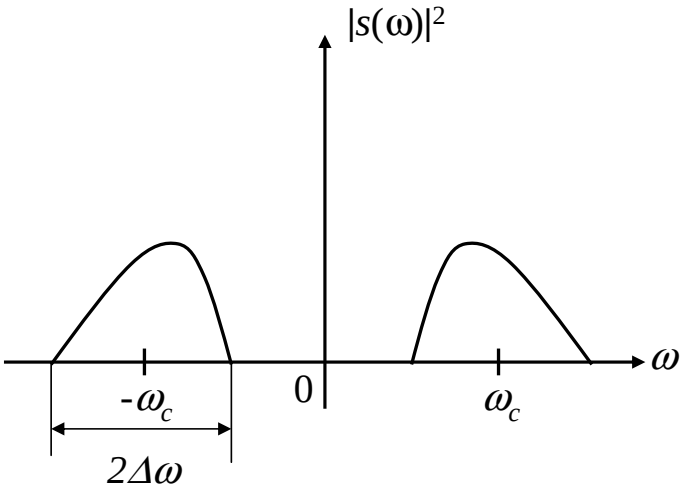

Figure 3: The energy spectrum of a real bandpass signal

After eliminating $B^*(\omega - 2\omega_c)$ by bandpass filtering, it becomes

$$\bar{X}_m(\omega) = H_m(\omega + \omega_c)B(\omega)e^{-j(\omega+\omega_c)\tau_m} + N_m(\omega + \omega_c). \tag{13}$$

If we assume that the sensor frequency response $H_m(\omega + \omega_c)$ is constant over signal's bandwidth, $H_m(\omega + \omega_c) \simeq H_m(\omega_c)$ and

$$\begin{aligned} \bar{X}_m(\omega) &\simeq H_m(\omega_c)B(\omega)e^{-j(\omega+\omega_c)\tau_m} + N_m(\omega + \omega_c) \\ &= H_m(\omega_c)B(\omega)e^{-j\omega_c(1+\omega/\omega_c)\tau_m} + N_m(\omega + \omega_c) \end{aligned} \tag{14}$$

This is common received signal model for both narrowband and wideband sources. Even if $H_m(\omega)$ is not flat, once we know the sensor frequency response, we can make it flat by proper compensation.

2.3.1 Narrowband Signals

If the bandwidth of $B(\omega)$ is $2\Delta\omega$ and $\Delta\omega/\omega_c \ll 1$, we can approximate (14) as

$$\bar{X}_m(\omega) = H_m(\omega_c)B(\omega)e^{-j\omega_c\tau_m} + N_m(\omega + \omega_c) \tag{15}$$

and this is a narrowband signal model. After the inverse Fourier transform,

$$\bar{x}_m(t) = H_m(\omega_c)b(t)e^{-j\omega_c\tau_m} + \bar{\eta}_m(t). \tag{16}$$

The sensor output of this simple model can be easily represented as a vector form.

$$\mathbf{x}(t) = s(t)\mathbf{a} + \mathbf{n}(t) \tag{17}$$

where

$$\mathbf{x}(t) = \begin{bmatrix} \bar{x}_0(t) & \cdots & \bar{x}_{M-1}(t) \end{bmatrix}^T,$$
$$\mathbf{n}(t) = \begin{bmatrix} \bar{\eta}_0(t) & \cdots & \bar{\eta}_{M-1}(t) \end{bmatrix}^T$$

and $\mathbf{a}$ is the array manifold vector such as

$$\mathbf{a} = \begin{bmatrix} e^{-j\omega_c\tau_0} & e^{-j\omega_c\tau_1} & \cdots & e^{-j\omega_c\tau_{M-1}} \end{bmatrix}^T$$

When there are P sources, $\mathbf{x}(t)$ is

$$\begin{aligned} \mathbf{x}(t) &= \begin{bmatrix} \mathbf{a}_0 & \cdots & \mathbf{a}_{P-1} \end{bmatrix} \begin{bmatrix} s_0(t) \\ \vdots \\ s_{P-1}(t) \end{bmatrix} + \mathbf{n}(t) \\ &= \mathbf{A}\mathbf{s}(t) + \mathbf{n}(t), \end{aligned} \tag{18}$$

where the $M \times P$ matrix $\mathbf{A}$ is called the *array response matrix*. Usually, $\mathbf{A}$ is a full rank matrix assuming that the array manifolds with different DOAs are independent. Note that the array manifold vector $\mathbf{a}_i$ depends on the DOA of the signal through the amount of delay τ_i. This vectorized signal model is used in most narrowband array signal processing techniques [24, 52]. Since each DOA can be represented by one array manifold vector the rank-one property holds for narrowband signals in (18). The rank-one property states that the rank of the correlation matrix of the vector of sensor outputs is same as the number of uncorrelated signals. If we assume that there is no noise, then, the correlation matrix of $\mathbf{x}(t)$ is

$$\begin{aligned} \mathbf{R}_x &= E[\mathbf{x}(t)\mathbf{x}^H(t)] \\ &= \mathbf{A}E[\mathbf{s}(t)\mathbf{s}^H(t)]\mathbf{A}^H. \end{aligned}$$

Since $\mathbf{A}$ is $M \times P$ full rank matrix, if we assume that the correlation matrix of $\mathbf{s}(t)$ is full rank, then, $\mathbf{R}_x$ is an $M \times M$ matrix whose rank is P, which is the number of

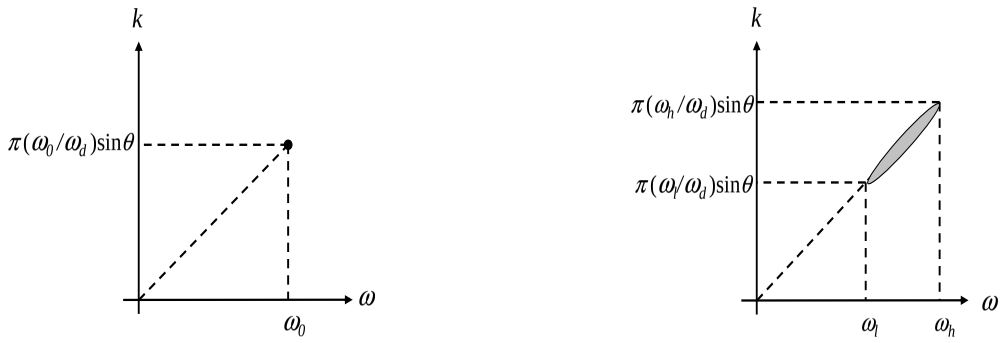

(a) Narrowband signal (b) Wideband signal

Figure 4: Narrowband and wideband signals in $\omega - k$ domain

signals. It is possible to split the M-dimensional space of received signals into the P-dimensional signal subspace and the $(M - P)$-dimensional noise subspaces, which is the basis of the signal subspace methods. The relationship between the rank-one property and the signal's bandwidth is discussed in [69] by exploiting the eigenvalues.

2.3.2 Wideband Signals

If the bandwidth $\Delta\omega$ is comparable to the center frequency ω_c, $s(t)$ is called a *wideband* signal and (14) cannot be approximated by (15) any more. In other words, the exponential term in (14) is not a constant and the sensor output cannot be vectorized as the narrowband signal model. Figure 4 compares narrowband and wideband signals in $\omega - k$ domain for linear arrays. While narrowband signals appears as a Dirac-delta function at one temporal frequency and one wavenumber, wideband signal occupies a relatively wide range of frequencies. One simple way to deal with wideband signals is to decompose the wideband signal into many narrowband signals using filter banks or the discrete Fourier transform along the temporal domain, picking the frequencies with the highest power. Then, narrowband methods can be applied to each narrowband component of the decomposed signal. However, this kind of approach does not take full advantage of the signal's frequency band because it discards some frequency bins which might have information about the DOA. Another

class of possible wideband methods are time-domain methods such as delay-and-sum (DS) beamforming. There have been many efforts to deal with wideband signals and this thesis will present two new methods.

CHAPTER 3

DIRECTION-OF-ARRIVAL (DOA) ESTIMATIONS

In the previous chapter, the basic background of array signal processing was reviewed. In this chapter, various DOA estimation methods are introduced. Since there are two types of signal models according to the bandwidth of the source, two different types of methods are discussed here. The chapter begins with narrowband DOA estimation methods in Section 3.1, followed by wideband DOA estimation methods in Section 3.2.

3.1 Narrowband DOA Estimation

The array signal model for narrowband sources, defined in Section 2.3, is

$$\mathbf{x}(t) = \mathbf{A}(\boldsymbol{\theta})\mathbf{s}(t) + \mathbf{n}(t) \tag{19}$$

where $\mathbf{A}$ is written as $\mathbf{A}(\boldsymbol{\theta})$ to emphasize its dependence on DOA where the vector $\boldsymbol{\theta}$ contains the angles to the P sources:

$$\boldsymbol{\theta} = [\theta_0, \theta_1, \ldots, \theta_{P-1}].$$

If we assume that the sensor position and the speed of propagation are known, then the array manifold vector is known in terms of the intersensor time delays and the DOAs:

$$\mathbf{a}(\theta) = \begin{bmatrix} 1 & e^{-j\omega_0\tau_1} & \cdots & e^{-j\omega_0\tau_{M-1}} \end{bmatrix}^T \tag{20}$$

where τ_m is the amount of delay at the m-th sensor. When the array is linear and the distance between sensors is $d = \lambda/2$ (ULA), where λ is the wavelength of frequency

ω_0, the array manifold vector can be simplified as

$$\mathbf{a}(\theta) = \begin{bmatrix} 1 & e^{-j\pi d \sin\theta} & \dots & e^{-j\pi(M-1)d\sin\theta} \end{bmatrix}^T.$$

When we know the structure of the array response matrix, DOA estimation becomes a parameter estimation method that tries to find the parameter θ in the array manifold response $\mathbf{A}(\boldsymbol{\theta})$ given the sensor output vector $\mathbf{x}(t)$.

3.1.1 Maximum Likelihood Methods

If the probability density of the noise and the signal waveform are known, it is possible to use the maximum likelihood estimator (MLE) for DOA estimation. There are two kinds of MLEs depending on the nature of the source signal. Unconditional MLE is used for random signals, while conditional MLE is for deterministic signals [52].

3.1.1.1 Unconditional MLE

Let the source signals be random variables with a known mean that does not depend on the DOA. Assume that the noise is zero-mean and Gaussian. Then, from (19), the probability density of $\mathbf{x}$ for a single snapshot is

$$p(\mathbf{x};\boldsymbol{\theta}) = \frac{1}{|\pi \mathbf{R}_x(\boldsymbol{\theta})|} \exp\left\{-(\mathbf{x}-\mathbf{m}_x)^H \mathbf{R}_x^{-1}(\boldsymbol{\theta})(\mathbf{x}-\mathbf{m}_x)\right\},$$

where $\mathbf{m}_x$ is the sum of the mean of the signal sources and

$$\mathbf{R}_x = \mathbf{A}(\boldsymbol{\theta})\mathbf{R}_s\mathbf{A}^H(\boldsymbol{\theta}) + \boldsymbol{\Sigma}, \tag{21}$$

where $\mathbf{R}_s$ is the correlation matrix of the source signal $\mathbf{s}(t)$ and $\boldsymbol{\Sigma}$ is the correlation matrix of the noise.

Without loss of generality, assume that $\mathbf{m}_x = \mathbf{0}$ and let $\mathbf{x}_j = \mathbf{x}(j)$ for $j = 0, \dots, J-1$ be independent snapshots. Then the joint probability density function is

$$p(\mathbf{x}_0, \mathbf{x}_1, \dots, \mathbf{x}_{J-1}; \boldsymbol{\theta}) = \prod_{j=0}^{J-1} \frac{1}{|\pi \mathbf{R}_x(\boldsymbol{\theta})|} \exp\left\{-\mathbf{x}_j^H \mathbf{R}_x^{-1}(\boldsymbol{\theta})\mathbf{x}_j\right\}$$

After dropping all the constants that are independent of $\boldsymbol{\theta}$,

$$\begin{aligned} L_x(\boldsymbol{\theta}) &= \ln p(\mathbf{x}_0, \mathbf{x}_1, \ldots, \mathbf{x}_{J-1}; \boldsymbol{\theta}) \\ &= -\left[\ln |\mathbf{R}_x(\boldsymbol{\theta})| + \frac{1}{J} \sum_{j=0}^{J-1} \mathbf{x}_j^H \mathbf{R}_x^{-1}(\boldsymbol{\theta}) \mathbf{x}_j \right] \end{aligned} \tag{22}$$

The objective of MLE is to find the vector $\boldsymbol{\theta}$ that maximizes (22), i.e.,

$$\hat{\boldsymbol{\theta}} = \arg\min_{\boldsymbol{\theta}} |L_x(\boldsymbol{\theta})|.$$

Equation (22) is a nonlinear function and MLE has to find minimum point in a P-dimensional space. Although MLE is in some sese the optimal estimator, due to its high computational cost and sensitivity to errors in the pdf, it is seldom used to find DOAs.

3.1.1.2 Conditional MLE

Conditional MLE is used when the source signal is modelled as an unknown but deterministic signal. In this case, the joint probability density function is

$$p(\mathbf{x}_0, \mathbf{x}_1, \ldots, \mathbf{x}_{J-1}; \boldsymbol{\theta}) = \prod_{j=0}^{J-1} \frac{1}{|\pi \sigma^2 \mathbf{I}|} \exp\left\{ -\frac{1}{\sigma^2} |\mathbf{x}_j - \mathbf{A}(\boldsymbol{\theta}) \mathbf{s}_j|^2 \right\}$$

where we assume that the noise covariance is $\sigma^2 \mathbf{I}$. The log likelihood function is

$$L(\boldsymbol{\theta}, \mathbf{s}) = -JM \ln \sigma^2 - \frac{1}{\sigma^2} \sum_{j=0}^{J-1} |\mathbf{x}_j - \mathbf{A}(\boldsymbol{\theta}) \mathbf{s}_j|^2 \tag{23}$$

The conditional MLE maximizes (23) and it is equivalent to minimizing

$$L'(\boldsymbol{\theta}, \mathbf{s}) = \frac{1}{\sigma^2} \sum_{j=0}^{J-1} |\mathbf{x}_j - \mathbf{A}(\boldsymbol{\theta}) \mathbf{s}_j|^2$$

3.1.2 Signal Subspace Methods

Signal subspace methods exploit the correlation matrix of the sensor output instead of processing received data directly. These methods take advantages of the rank-one

property of narrowband signals to find the signal subspace and the noise subspace. The correlation matrix of the sensor output is given by (21):

$$\mathbf{R}_x = E[\mathbf{x}(t)\mathbf{x}^H(t)] = \mathbf{A}(\boldsymbol{\theta})\mathbf{R}_s\mathbf{A}^H(\boldsymbol{\theta}) + \boldsymbol{\Sigma}$$

When the noise is white, $\boldsymbol{\Sigma} = \sigma^2\mathbf{I}$. If the covariance matrix of the noise is known up to scale, we can make it white noise by whitening . Note that the rank of $\mathbf{R}_x$ is M (full rank) when the noise correlation matrix is full rank.

3.1.2.1 Signal Subspace

Assume that the signal sources $s_i(t)$ are not fully correlated with each other. Then, the correlation matrix $\mathbf{R}_s$ is a full rank matrix. The range of $\mathbf{R}_x$, which is an M-dimensional space, can be divided into two orthogonal subspaces: 1) a P-dimensional signal subspace which is the range of $\mathbf{A}(\boldsymbol{\theta})$ and 2) an $(M-P)$-dimensional noise subspace. The signal subspace and the noise subspace can be found by eigenvalue decomposition (EVD) of the correlation matrix $\mathbf{R}_x$. Assume that the P sources are uncorrelated with each other. Then, $\mathbf{R}_s$ is a diagonal matrix and $\mathbf{R}_x$ is

$$\begin{aligned}
\mathbf{R}_x &= \begin{bmatrix} \mathbf{a}(\theta_0) & \cdots & \mathbf{a}(\theta_{P-1}) \end{bmatrix} \begin{bmatrix} P_0 & 0 & \cdots & 0 \\ 0 & P_1 & & \vdots \\ \vdots & & \ddots & 0 \\ 0 & \cdots & 0 & P_{P-1} \end{bmatrix} \begin{bmatrix} \mathbf{a}^H(\theta_0) \\ \vdots \\ \mathbf{a}^H(\theta_{P-1}) \end{bmatrix} + \sigma^2\mathbf{I} \qquad (24) \\
&= \sum_{l=0}^{P-1} P_l\mathbf{a}(\theta_l)\mathbf{a}^H(\theta_l) + \sigma^2\mathbf{I}. \qquad (25)
\end{aligned}$$

where P_l is the power of the l-th source. Let $\mathbf{v}_j$ be an orthonormal eigenvector of $\mathbf{R}_x$, then,

$$\begin{aligned}
\mathbf{R}_x\mathbf{v}_j &= \sum_{l=0}^{P-1} P_l\mathbf{a}(\theta_l)\mathbf{a}^H(\theta_l)\mathbf{v}_j + \sigma^2\mathbf{v}_j \\
&= \hat{\mathbf{v}}_j + \sigma^2\mathbf{v}_j \\
&= \lambda_j\mathbf{v}_j \qquad (26)
\end{aligned}$$

where λ_j is the corresponding eigenvalue. In order for (26) to hold, $\hat{\mathbf{v}}_j$ must equal $\alpha\mathbf{v}_j$ where α is a constant scalar ($\alpha \geq 0$). Depending on the value of α, there are two sets of eigenvectors $\mathbf{v}_j$. First when $\alpha > 0$ the eigenvectors are linear combinations of $\mathbf{a}(\theta_l)$. Another set is the set of eigenvectors which are orthogonal to $\mathbf{a}(\theta_l)$ for all $l = 0, \ldots, P-1$ so that $\alpha = 0$. The eigenvectors whose eigenvalues are large ($\alpha > 0$) are in the first set and the range of these eigenvectors are called the *signal subspace* since it is the range space of the array response matrix $\mathbf{A}$. On the other hand, the rest of the eigenvectors whose eigenvalue is σ^2 ($\alpha = 0$) span the *noise subspace*. Since the first set of eigenvectors are linear combinations of P independent vectors $\mathbf{a}(\theta_l)$, the number of eigenvectors that span the signal subspace is always P, so that the signal subspace has a rank P. The rank of the noise subspace which is orthogonal to the signal subspace is always $M - P$.

3.1.2.2 MUSIC

MUSIC (MUltiple SIgnal Classification) is a signal subspace method [41] that tries to find the array manifold orthogonal to the noise subspace since the noise subspace is orthogonal to the signal subspace. The MUSIC estimate is

$$\hat{\theta} = \arg\max_{\theta} \frac{\mathbf{a}^H(\theta)\mathbf{a}(\theta)}{\mathbf{a}^H(\theta)\mathbf{W}\mathbf{W}^H\mathbf{a}(\theta)} \tag{27}$$

where $\mathbf{W}$ is a matrix whose columns span the noise subspace such as

$$\mathbf{W} = \begin{bmatrix} \mathbf{v}_P & \cdots & \mathbf{v}_{M-1} \end{bmatrix}$$

where $\mathbf{v}_0, \ldots, \mathbf{v}_{M-1}$ are eigenvectors ordered in decreasing size of their corresponding eigenvalues. If θ is the same as one of the DOAs, $\mathbf{a}(\theta)$ should be orthogonal to the noise subspace $\mathbf{W}$ so that the denominator in (27) becomes zero making (27) maximum. In most cases, the correlation matrix and σ are unknown to the processor. Furthermore, an estimated correlation matrix $\hat{\mathbf{R}}_x$ would be used in place of the true correlation matrix, so that one obtains an estimate of the noise subspace $\hat{\mathbf{W}}$. The correlation

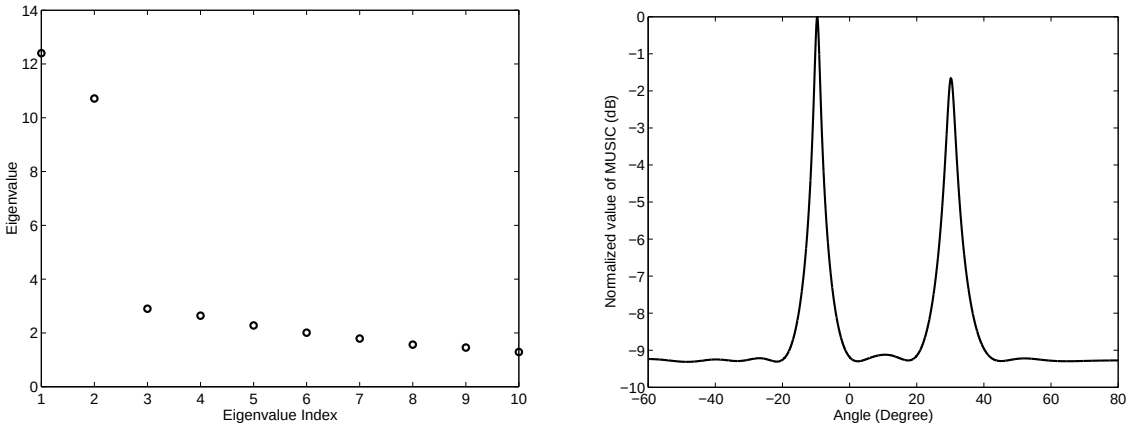

(a) (b)

Figure 5: Example of MUSIC: (a) eigenvalues (b) plot of the normalized righthand side of (27) in dB scale.

matrix $\hat{\mathbf{R}}_x$ is usually defined as

$$\hat{\mathbf{R}}_x = \frac{1}{J}\sum_{t=0}^{J-1}\mathbf{x}(t)\mathbf{x}^H(t)$$

Due to errors in the estimated correlation matrix, the eigenvalues of the noise subspace are no longer equal to σ^2. In this case, we need to decide the dimension of the signal subspace (or the noise subspace) by looking at the eigenvalues. Examples of methods to estimate P appear in [3] (AIC) or [43] (MDL). Once the number of signals is estimated as P, the eigenvectors whose eigenvalues are the P largest eigenvalues define the signal subspace and the remaining $M - P$ eigenvectors define the noise subspace $\hat{\mathbf{W}}$. Figure 5 shows one example result of a MUSIC estimator for a ten-sensor ULA with -3 dB SNR. Figure 5 (a) is a plot of the ordered eigenvalues of the correlation matrix. Two large eigenvalues are easily distinguishable from the rest indicating that two source signals are likely to be present. Figure 5 (b) illustrates the MUSIC estimates, i.e, the righthand side of (27), indicating that two peaks are present at -10° and 30° where the targets are actually located.

3.1.2.3 Other Methods

There are many signal subspace methods other than MUSIC. Some variants of the MUSIC estimator include Root-MUSIC [5] and beamspace MUSIC [71]. ESPRIT is another signal subspace method that does not require an array manifold vector [40]. All the signal subspace methods involve a common process of finding the signal subspace and the noise subspace.

3.2 Wideband DOA Estimation

3.2.1 Delay and Sum Beamforming

Since signals are received by multiple sensors, we have multiple sensor outputs which represent mixtures of the same sources with different delays that depend on the sensor locations relative to the source positions. Beamforming is the processing that *forms* the signal due to a source coming from a specific direction (called the steering direction) by combining the raw sensor outputs [24, 52]. This could be considered as spatial bandpass filtering on the propagating signal field since it passes signals that come only from the steering direction and suppress as all other signals including noise. In order to coherently sum the signal coming from a beamforming direction, it is necessary to algin the phase center of the signal by delaying each sensor output. The name delay-and-sum (DS) beamforming comes from this time-delay-and-sum processing. DS beamforming in the $\vec{\alpha}_o$ direction computes the beamformed output via

$$z(t;\vec{\alpha}_0) = \frac{1}{M}\sum_{m=0}^{M-1} w_m x_m\{t + (\vec{r}_m \cdot \vec{\alpha}_0)\}, \tag{28}$$

where w_m is a weighting applied to the M sensors of the array. When there is a single source from direction $\vec{\alpha}$,

$$x_m(t) = s\{t - (\vec{r}_m \cdot \vec{\alpha})\},$$

the beamformed output, (28) becomes

$$z(t;\vec{\alpha}_0) = \frac{1}{M}\sum_{m=0}^{M-1} w_m s\{t - \vec{r}_m \cdot (\vec{\alpha} - \vec{\alpha}_0)\}. \tag{29}$$

The summation is coherent only if the beamforming direction $\vec{\alpha}_o$ and the signal's slowness vector $\vec{\alpha}$ match. In that case, the energy corresponding to the beamformed signal for the correct DOA will be the largest. However, DS beamforming exhibits some disadvantages. First, the width of passband along the wavenumber domain is relatively wide. The resolution of DS beamforming is the same as Fourier analysis along the spatial domain. Like all Fourier methods, the width of mainlobe is inversely proportional to the length of the sensor array. Unless the array baseline is large enough, its Rayleigh resolution is very low and it is not suitable for high resolution beamforming. Second, it requires a large number of computations. The computational complexity of DS beamforming is $O(n^3)$ for n sensors, n beamforming directions, and n time snapshots. However, since it can be used regardless of the bandwidth of the sources, DS beamforming can be used as a row-resolution DOA estimator for wideband signals. In Chapter 4, a new fast DS beamforming method is proposed.

3.2.2 Signal subspace

In Section 2.3, the difference between narrowband and wideband was mentioned. If the signal source is wideband, the time-delay cannot be approximated by a phase-shift and this makes the rank-one property fail. However, in the temporal frequency domain, the sensor output can be represented in a matrix-vector format as frequency dependent narrowband signals.

$$\mathbf{X}(\omega) = \mathbf{A}(\omega, \boldsymbol{\theta})\mathbf{S}(\omega) + \mathbf{N}(\omega) \tag{30}$$

where the frequency-dependent steering matrix is

$$\mathbf{A}(\omega, \boldsymbol{\theta}) = \begin{bmatrix} \mathbf{a}(\omega, \theta_0) & \cdots & \mathbf{a}(\omega, \theta_{P-1}) \end{bmatrix}$$

and the frequency-dependent array manifold vector is

$$\mathbf{a}(\omega, \theta_l) = \left[\begin{array}{ccc} e^{-j\omega\tau_0(\theta_l)} & \ldots & e^{-j\omega\tau_{M-1}(\theta_l)} \end{array} \right]^T$$

If the frequency in (30) is fixed, it is possible to use narrowband signal subspace methods such as MUSIC. By bandpass filtering or DFT, we can perform a narrowband decomposition to obtain sensor outputs with a fixed temporal frequency. However, since the signal is wideband, we will have to repeat MUSIC for each of the multiple discrete frequency components.

Wideband DOA estimation methods can be divided into two groups depending on whether or not a narrowband decomposition is done, e.g., the methods in [2, 8, 49] do not use the decomposition. The other group which does employ the narrowband decomposition takes advantage of well-developed narrowband signal subspace methods, e.g., the methods in [58, 12, 32, 54, 53]. Since the new method proposed in this thesis falls in the second group, only those methods will be reviewed in this section.

The decomposed signal can be represented as

$$\mathbf{X}(\omega_i) = \mathbf{A}(\omega_i)\mathbf{S}(\omega_i) + \mathbf{N}(\omega_i) \tag{31}$$

for $i = 1, \ldots, K$ and the corresponding correlation matrix is

$$\mathbf{R}_x(\omega_i) = \mathbf{A}(\omega_i)\mathbf{R}_s(\omega_i)\mathbf{A}^H(\omega_i) + \mathbf{\Sigma}(\omega_i)$$

where

$$\mathbf{R}_s(\omega_i) = E\left[\mathbf{S}(\omega_i)\mathbf{S}^H(\omega_i)\right].$$

Frequency ω_i are within the frequency bands where all the wideband signals' passbands are overlapped. Note that we have K correlation matrices corresponding to K narrowband signals. The methods in the second group can be further divided into two groups depending on whether the decomposed signals of multiple frequencies are used independently or new statistics are generated coherently from several frequency bins.

3.2.3 Incoherent Methods

Incoherent methods use the K decomposed signals independently. Since the decomposed signals are assumed to be narrowband signals, narrowband methods can be applied independently and the final estimates can be the average of those independent results [61, 37]. For example, the incoherent MUSIC (IMUSIC) estimator is

$$\hat{\theta} = \arg\max_{\theta} \sum_{i=1}^{K} \frac{\mathbf{a}^H(\omega_i, \theta)\mathbf{a}(\omega_i, \theta)}{\mathbf{a}^H(\omega_i, \theta)\mathbf{W}_i\mathbf{W}_i^H\mathbf{a}(\omega_i, \theta)} \tag{32}$$

where $\mathbf{W}_i$ is the noise subspace at frequency ω_i. Instead of MUSIC, any narrowband technique can be used to estimate DOAs at each frequency. Incoherent methods work well in favorable situations, i.e., well-separated signals and high SNR. However, since the final estimate is the average of results from all frequency bins, one outlier can degrade the estimator's performance [58] and processing more frequency bins might not provide significantly better results when there is incoherence between frequencies. In the low SNR case, having more frequency bins could even degrade the estimator's performance. In order to overcome these problems, *coherent* methods were proposed.

3.2.4 Coherent Methods

The first coherent method was proposed in 1985 by Wang and Kaveh [58]. In their paper, they introduced the coherent signal subspace method (CSSM). Since then, several variations of CSSM have been proposed. Some examples are found in [32, 54]. Recently, a slightly different coherent method known as WAVES was proposed [12].

3.2.4.1 CSSM

The CSSM was the first approach to average the correlation matrices of various frequency bins in a coherent way [58]. Since the signal subspace and the noise subspace depend on frequency, a preprocessing step called *focusing* is required to add the correlation matrices *coherently*. Focusing is the process of transforming the correlation matrices of different frequency bins before averaging by a transformation matrix called

the *focusing matrix*. Let $\mathbf{R}_i$ be the correlation matrix of $\mathbf{X}(\omega_i)$. Then, the general correlation matrix is

$$\mathbf{R}_{gen} = \sum_{i=1}^{K} \alpha_i \mathbf{T}_i \mathbf{R}_i \mathbf{T}_i^H \tag{33}$$

where α_i is a weight and $\mathbf{T}_i$ is the focusing matrix for ω_i obtained via

$$\min_{\mathbf{T}_i} \|\mathbf{A}(\omega_0, \boldsymbol{\theta}_f) - \mathbf{T}_i \mathbf{A}(\omega_i, \boldsymbol{\theta}_f)\|_F \tag{34}$$

where $\boldsymbol{\theta}_f$ is the set of angles called the focusing angles. In other words, the focusing matrix is a transformation matrix that transforms the array response matrix with DOA $\boldsymbol{\theta}_f$ at frequency ω_i to that of frequency ω_0. Assume that the noise covariance at frequency ω_i is

$$\boldsymbol{\Sigma}(\omega_i) = \sigma^2(\omega_i)\mathbf{I}.$$

Since the correlation matrix at frequency ω_i is

$$\mathbf{R}_i = \mathbf{A}(\omega_i, \boldsymbol{\theta})\mathbf{R}_s(\omega_j)\mathbf{A}^H(\omega_i, \boldsymbol{\theta}) + \sigma^2(\omega_i)\mathbf{I},$$

if $\boldsymbol{\theta}_f = \boldsymbol{\theta}$ and

$$\|\mathbf{A}(\omega_0, \boldsymbol{\theta}_f) - \mathbf{T}_i \mathbf{A}(\omega_i, \boldsymbol{\theta}_f)\|_F \simeq 0,$$

the general correlation matrix is

$$\begin{aligned}
\mathbf{R}_{gen} &= \sum_{i=1}^{K} \mathbf{T}_i \mathbf{R}_i \mathbf{T}_i^H \\
&= \sum_{i=1}^{K} \mathbf{T}_i \left\{ \mathbf{A}(\omega_i, \theta_f)\mathbf{R}_s(\omega_i)\mathbf{A}^H(\omega_i, \theta_f) + \sigma^2(\omega_i)\mathbf{I} \right\} \mathbf{T}_i^H \\
&\simeq \mathbf{A}(\omega_0, \theta_f) \sum_{i=1}^{K} \mathbf{R}_s(\omega_i)\mathbf{A}^H(\omega_0, \theta_f) + \sum_{i=1}^{K} \sigma^2(\omega_i)\mathbf{T}_i\mathbf{T}_i^H
\end{aligned} \tag{35}$$

The general correlation matrix (35) has exactly the same structure as the correlation matrix of narrowband signals at frequency ω_0 except that the noise covariance matrix is no longer an identity matrix. Therefore, a narrowband signal subspace method can be applied to $\mathbf{R}_{gen}$. The performance of the CSSM depends on how close the

general correlation matrix (33) is to the form of (35). Focusing matrices $\mathbf{T}_i$ and the focusing angles $\boldsymbol{\theta}_f$ play a very important role in minimizing focusing error, i.e. the difference between $\mathbf{R}_{gen}$ and $\mathbf{R}_0$. One well known focusing matrix is the signal subspace transformation (SST) matrix [13]. SST matrix is optimal in the sense that it minimizes focusing loss which is defined as the ratio of SNR before and after focusing operations. The focusing loss g is [21]

$$g = \frac{tr\left\{\mathbf{R}_n^{-1}\sum_{i=1}^{K}\mathbf{T}_i\mathbf{A}(\omega_i,\theta)\mathbf{R}_s(\omega_i)\mathbf{A}^H(\omega_i,\theta)\mathbf{T}_i^H\right\}}{tr\left\{\sum_{i=1}^{K}\mathbf{A}(\omega_i,\theta)\mathbf{R}_s(\omega_i)\mathbf{A}^H(\omega_i,\theta)\right\}}$$

where

$$\mathbf{R}_n = \frac{\sum_{i=1}^{K}\sigma^2(\omega_i)\mathbf{T}_i\mathbf{T}_i^H}{\sum_{i=1}^{K}\sigma^2(\omega_i)}.$$

It is easy to show that $g = 1$ when $\mathbf{T}_i\mathbf{T}_i^H$ is independent of ω_i [13]. The rotational signal subspace (RSS) focusing matrix, proposed in [21], provides one type of SST matrices since $\mathbf{T}_i\mathbf{T}_i^H = \mathbf{I}$ [13]. Once the focusing angle $\boldsymbol{\theta}_F$ is determined, the RSS focusing matrix $\mathbf{T}_i$ can be found as

$$\min_{\mathbf{T}_i}\|\mathbf{A}(\omega_0,\boldsymbol{\theta}_f) - \mathbf{T}_i\mathbf{A}(\omega_i,\boldsymbol{\theta}_f)\|_F \tag{36}$$

for $i = 1,\ldots,K$ subject to

$$\mathbf{T}_i\mathbf{T}_i^H = \mathbf{I}.$$

The solution to the above optimization problem is

$$\mathbf{T}_i = \mathbf{V}_i\mathbf{U}_i^H \tag{37}$$

where the columns of $\mathbf{U}_i$ and $\mathbf{V}_i$ are left and right singular vectors of $\mathbf{A}(\omega_o,\boldsymbol{\theta}_f)\mathbf{A}^H(\omega_i,\boldsymbol{\theta}_f)$ [21].

The problem becomes, therefore, how to find focusing angles θ_f that should be the same as the signal's DOA which is unavailable. Usually, low-resolution DOA

estimation techniques are used to find focusing angles that should be close enough to the true DOAs. However, some closely spaced DOAs cannot be resolved using this process. Furthermore, unlike initial values in some iterative methods, focusing angles do not necessarily produce a solution with the correct value. Focusing angles should be close to the true DOA in order to have good estimates, but, if it is not same as true DOA and the focusing frequency is not the centroid of the signal's band, the bias will never go to zero. The bias could be very critical to high resolution methods and is the main disadvantage of CSSM.

3.2.4.2 BICSSM

BICSSM stands for beamforming-invariant CSSM [32]. This method is similar to CSSM in the sense that it uses a transformation matrix. The difference with respect to CSSM is that the transformation matrix minimizes error not between signal subspaces but between beams of multiple frequency bins. In order to find those transformation matrices, BICSSM needs to find beamforming weight vectors $\mathbf{t}_i$ and $\mathbf{t}_j$ satisfying

$$\min_{\mathbf{t}_i,\mathbf{t}_j} \int_{\Omega} \rho(\vec{\alpha}) \left| \mathbf{t}_i^H \mathbf{a}_i(\vec{\alpha}) - \mathbf{t}_j^H \mathbf{a}_j(\vec{\alpha}) \right|^2 d\vec{\alpha}$$

where Ω is the field of view (FOV) and $\rho(\vec{\alpha})$ is a weighting function. If the reference frequency ω_0 is fixed as the focusing frequency in CSSM, then the corresponding beamforming weight is

$$\min_{\mathbf{t}_j} \int_{\Omega} \rho(\vec{\alpha}) \left| \mathbf{t}_0^H \mathbf{a}_0(\vec{\alpha}) - \mathbf{t}_j^H \mathbf{a}_j(\vec{\alpha}) \right|^2 d\vec{\alpha}$$

In order to form an $\hat{M}$-dimensional beamspace, it uses $\hat{M}$ ($P < \hat{M} < M$) beamforming weights as a reference beamforming weights. The $\hat{M} \times M$ transformation matrix is found for each frequency i by

$$\mathbf{T}_i = \begin{bmatrix} \mathbf{t}_{i,1}^H \\ \vdots \\ \mathbf{t}_{i,\hat{M}}^H \end{bmatrix}$$

where

$$\min_{\mathbf{t}_{i,\hat{m}}} \int_{\Omega} \rho(\vec{\alpha}) \left| \mathbf{t}_{0,\hat{m}}^H \mathbf{a}_0(\vec{\alpha}) - \mathbf{t}_{i,\hat{m}}^H \mathbf{a}_i(\vec{\alpha}) \right|^2 d\vec{\alpha} \tag{38}$$

for $\hat{m} = 0, \ldots, \hat{M} - 1$. If we rewrite (38) similar to CSSM,

$$\min_{T_i} \int_{\Omega} \left| \mathbf{T}_0 \mathbf{a}_0(\vec{\alpha}) - \mathbf{T}_i \mathbf{a}_i(\vec{\alpha}) \right|^2 d\vec{\alpha}.$$

BICSSM tries to minimize the difference between beams of different frequencies within FOV to get rid of the focusing angle requirement. Once all the $\mathbf{T}_i$'s are found, it generates the general correlation matrix as

$$\mathbf{R}_{gen} = \sum_{i=1}^{K} w_i \mathbf{T}_i \mathbf{R}_i \mathbf{T}_i^H.$$

Since $\mathbf{T}_0 \mathbf{a}_0(\vec{\alpha}) \simeq \mathbf{T}_i \mathbf{a}_i(\vec{\alpha})$ in the FOV, the general correlation matrix is

$$\mathbf{R}_{gen} \simeq \mathbf{B}_0 \left(\sum_{i=1}^{K-1} w_i \mathbf{R}_s(\omega_i) \right) \mathbf{B}_0^H$$

where $\mathbf{B}_0 = \mathbf{T}_0 \mathbf{A}_0$. The narrowband MUSIC now can be applied to the general correlation matrix with the array manifold equal to $\mathbf{T}_0 \mathbf{a}_0(\vec{\alpha})$.

The reference beamforming weight $\mathbf{T}_0$ plays the same important role as the focusing angles in CSSM. Usually, beamforming weights toward $\hat{M}$ directions which are uniformly distributed in the FOV are used for $\mathbf{T}_0$. Since the errors between beams are minimized only within the FOV, the reference beamformer should have low sidelobes outside of the FOV. Furthermore, the beam pattern should be invariant between the frequency components. Although BICSSM is able to avoid the focusing angle requirement, depending on the array geometry, there may not exist a reference beamformer that satisfies both conditions and the FOV may be unavailable to the processor.

3.2.4.3 WAVES

Weighted average of signal subspaces (WAVES) method is a recently developed signal subspace method [12]. It uses a pseudodata matrix that comes from the weighted subspace fitting (WSF) method [57]. Specifically, WAVES estimates the noise subspaces

at a normalized frequency by taking the SVD of the pseudodata matrix $\mathbf{Z}$

$$\mathbf{Z} = \begin{bmatrix} \mathbf{T}_1\mathbf{F}_1\mathbf{P}_1 & \mathbf{T}_2\mathbf{F}_2\mathbf{P}_2 & \cdots & \mathbf{T}_K\mathbf{F}_K\mathbf{P}_K \end{bmatrix}$$

The focusing matrix $\mathbf{T}_i$ can be that of either CSSM or BICSSM [32]. When the signal and noise are Gaussian distributed, the k-th diagonal element of the weighting matrix $\mathbf{P}_i$ is [57]

$$[\mathbf{P}_i]_{(k,k)} = \frac{\lambda_{i,k} - \sigma_n^2}{\sqrt{\lambda_{i,k}\sigma_n^2}}.$$

where $\lambda_{i,k}$ is the k-th largest eigenvalue of $\mathbf{R}_i$ and σ_n^2 is the noise power which is assumed to be constant over frequency bins. From the pseudodata matrix $\mathbf{Z}$ which is an $M \times KP$ matrix, WAVES finds the noise subspace $\mathbf{U}_N$ by doing an SVD.

$$\mathbf{Z} = \begin{bmatrix} \mathbf{U}_S & \mathbf{U}_N \end{bmatrix} \begin{bmatrix} \mathbf{\Sigma}_S & \mathbf{0} \\ \mathbf{0} & \mathbf{\Sigma}_N \end{bmatrix} \begin{bmatrix} \mathbf{V}_S & \mathbf{V}_N \end{bmatrix}^H$$

The subspace $\mathbf{U}_N$ can be used in place of noise subspace in any narrowband signal subspace methods. For example, if MUSIC estimator is used [41], $\mathbf{U}_N$ can replace $\mathbf{W}$ in (27).

WAVES is similar to CSSM since it exploits the noise subspace of the general correlation matrix such as

$$\mathbf{R}_{gen} = \sum_{i=1}^{K} \mathbf{T}_i\{\mathbf{F}_i\mathbf{P}_i\mathbf{P}_i^H\mathbf{F}_i^H\}\mathbf{T}_i^H.$$

However, this method works better than CSSM since it uses weighted signal subspaces instead of using sensor outputs directly to generate a general correlation matrix . If $\mathbf{T}_i$ is borrowed from BICSSM, WAVES does not require focusing angles. However, the estimator performance is better when $\mathbf{T}_i$ is from CSSM and also has good focusing angles [12].

CHAPTER 4

PRUNED FAST BEAMFORMING

In this chapter, a new fast beamforming based on pruning the delay-and-sum beamformer is presented. Although it is not a high-resolution method, it can quickly identify DOAs of interest where signals will be found.

4.1 Fast Multi-stage DS Beamforming

The high computational cost of DS beamforming induced many efforts to reduce the number of computations. The fast multi-stage beamformer is one of those efforts [34]. The fast DS beamformer is a divide-and-conquer method that divides the angular space into small angular sectors and forms multiple beams per sector by partially integrating the steered signals. Initially, the entire plane covering sources from $-90°$ to $90°$ (linear array case) forms one sector where the sensor outputs for each array element form M partial beams where M is the number of elements. The first stage of the fast beamformer divides one sector into N sectors. For each sector, the M signals

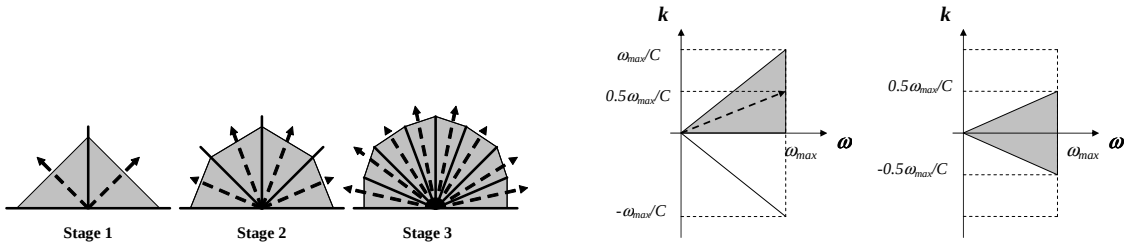

(a) (b)

Figure 6: Steering directions and $\omega - k$ representation of wavefield. (a) Angular sectors and steering angles at each stage. The dashed lines show boundaries of sectors and the dotted lines show steering angles. (b) Spectral support of a wavefield. Dark triangle is the sector to be processed.

are steered toward the phase center of the sector, and adjacent beams are integrated to form M/N signals representing N steered beams by filtering and downsampling by a factor of N along the spatial (or angular) dimension. The process of subdividing sectors by N, steering beams, filtering and downsampling continues in an iterative fashion until each sector (or steered beams) contains a single signal, i.e., full decomposition of the sensor outputs. Figure 6(a) shows the angular sectors and the steering directions at each stage for $N = 2$. Dashed lines represent sector boundaries while the dotted lines represent steering directions, which are phase centers of the sectors. More steering directions mean smaller angular sectors and higher angular sampling. Figure 6(b) illustrates the spectral support of a sector before and after steering to its phase center when $N = 2$. The arrow represents the phase center. After steering, the information of the sector can be preserved by lowpass filtering and downsampling by a factor of N. Unlike the conventional DS beamformer, the delayed sensor outputs are not summed altogether. Instead, the sensor outputs are filtered in the spatial domain and downsampled. Until the final stage, a sector consists of several beams steered toward the same direction (Fig. 7). The details of the general fast DS beamformer is described in [34].

In this thesis, a radix-2 fast beamformer is introduced. The number of sensors is $M = 2^S$ so that at each stage, the number of steering directions, i.e., angular sectors, is doubled and the number of beams per sector is halved. For implementation of the lowpass filter, the fast beamformer uses a simple uniform two tap filter. Longer filters can provide a better approximation to the DS beamformer at the expense of a higher computational cost. At stage s, the number of steered beams is $N_d = 2^s$, and the number of signals per beam is $N_b = M/2^s = 2^{S-s}$. To achieve the radix-2 fast beamformer, the sector centers at Stage s are $\theta_i = \pm \arcsin \frac{2i-1}{2^s}$ for $i = 1, 2, \ldots, 2^{s-1}$. In other words, the phase centers of sectors are uniformly spaced in the $\sin\theta$ domain.

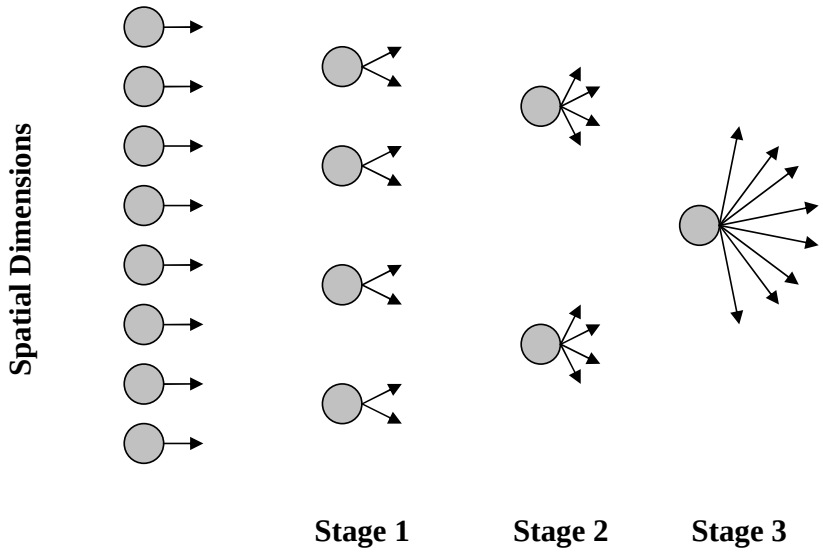

Figure 7: Radix-2 fast beamforming with 8 sensors.

4.2 Sector Pruning

Between each stage of the beamformer, it is possible to determine whether or not a sector might contain a source and to eliminate the sector from further processing if a source is not present. To detect sources, a detector is used that determines whether or not coherent summation has occurred during earlier stages. A similar detector was used in [26] for quadtree SAR processing. Clearly, removing sectors from further stages of the DS fast beamformer will save computations, speed up processing time and lower power usage.

The sensor output model for the m-th sensor due to single source can be rewritten as

$$x_m(t) = s(t - l_{m,\theta}) + n_m(t), \tag{39}$$

where $s(\cdot)$ is the target source, $n_m(t)$ is white Gaussian noise with zero mean and N_o variance, and $l_{m,\theta}$ is the time-shift depending on the source's DOA θ. At the first stage, the filter effectively combines two signals into one by summing them together. The m-th signal after the first stage for the d-th sector is

$$v_{1,m,d}(t) = x_{2m}(t + \vec{r}_{2m} \cdot \vec{\alpha}_d) + x_{2m+1}(t + \vec{r}_{2m+1} \cdot \vec{\alpha}_d), \tag{40}$$

where $\vec{\alpha}_d$ is the steering vector for the center of d-th sector. Given that the sector center is close to the source direction, the source terms in (39) are essentially summed coherently so

$$v_{1,m,d}(t) = 2s(t) + \hat{n}_1(t), \tag{41}$$

where $\hat{n}_1(t)$ is a white Gaussian noise with zero mean. The variance of $\hat{n}_1(t)$ is $2N_o$ since it is the sum of two independent Gaussian noise processes of variance N_o. Therefore, the average energy of all beams in the d-th sector is

$$\varepsilon_1 = 4S_0 + 2N_0, \tag{42}$$

where S_0 is the signal energy,

$$S_0 = \int |s(t)|^2 \, dt.$$

As the stages of the fast beamformer progress, the source signals in the steered signals continue to sum coherently when the sector contains the target sources, while the noise sums incoherently, so that the energy in the sector after the sth stage is

$$\begin{aligned} \varepsilon_s &= 4S_{s-1} + 2N_{s-1} \\ &= 4^s S_o + 2^s N_o. \end{aligned} \tag{43}$$

As one can see from (43), when a source signal is present in a sector, the energy in the sector increases by a factor of four during each stage of the fast beamformer. Conversely, if only noise is present, the sector energy only increases by a factor of two. As a result, as the stage of the fast beamformer progresses, the SNR improves. We use an estimate of the signal processing gain (SPG) as the detection statistic. The statistic is computed for each sector. If the statistic passes the threshold test, the beams corresponding to the sector are passed to the next stage for refined beamforming. The sectors not passing the threshold test are removed from further processing. The SPG estimate is based upon the fact that the computed d-th sector energy follows

$$\hat{\varepsilon}_{d,s} = \frac{1}{N_b} \sum_{m=1}^{N_b} \sum_{n=1}^{N_p} |v_{s,m,d}[n]|^2, \tag{44}$$

for $d = 1, 2, \ldots, N_d$, where $v_{s,m,d}[\cdot]$ is the intermediate fast beamformed signal. The mean value of $\hat{\varepsilon}_{d,s}$ is

$$E[\hat{\varepsilon}_{d,s}] = 4^s S_o + 2^s N_o. \tag{45}$$

The detection statistic $t_{d,s}$ for the d-th sector at stage s is

$$t_{d,s} = \frac{\hat{\varepsilon}_{d,s} - 2\hat{\varepsilon}_{c,s-1}}{4\hat{\varepsilon}_{k,1} - \hat{\varepsilon}_{l,2}}, \tag{46}$$

where the k-th sector for Stage 1, the l-th sector for Stage 2, and the c-th sector for Stage $(s-1)$ contains the d-th sector at Stage s. The numerator is the estimated signal energy at the s-th stage and the denominator is estimated noise at the first stage. The detection statistic is nothing but coherent signal processing gain. Then, the detector is

$$t_{d,s} \lessgtr 4^s \zeta, \tag{47}$$

where ζ is a control factor, which is adjusted to balance the tradeoff between passing lower SNR sources and the computational complexity, i.e., number of sectors not pruned.

4.3 Computational Complexity

In this section, the computational complexity of the fast beamformer with and without pruning is calculated in terms of floating point operations, e.g., additions and multiplications.

4.3.1 Fast beamformer

Fast beamforming consists of time-shift, interpolation, and addition. It requires three multiplications to compute the time delay to steer each beam. To shift the beams by non-integer delays, the fast beamformer uses interpolation. The number of flops for generating one beam by interpolation and filtering is $I \cdot N_p + F \cdot N_p$ where I and F are the number of computations for interpolating and filtering (or summing) adjacent

beams, respectively. In addition, N_p is number of snapshots per beam. The value for F depends on the exact interpolation method. The number of computations of fast beamformer is

$$D_{fast} = \{N_p(I+F)+3\}\sum_{i=1}^{S} L_i, \tag{48}$$

where L_i is the number of processed beams at stage i. Since L_i is the number of spatial dimensions times the number of steering directions, it is always M. Therefore, the total number of computations for the fast beamformer is

$$\begin{aligned} D_{fast} &= \{N_p(I+F)+3\}\sum_{i=1}^{\log_2 M} L_i & (49)\\ &= \{N_p(I+F)+3\}\sum_{i=1}^{\log_2 M} M & (50)\\ &= \{N_p(I+F)+3\}M\log_2 M. & (51)\\ & & (52) \end{aligned}$$

If $N_p = M$,

$$D_{fast} \cong M^2(F+I)\log_2 M. \tag{53}$$

4.3.2 Pruned fast beamformer

There are two differences between the number of computations for pruned and non-pruned fast beamforming. First, the number of sectors for pruned fast beamforming is always less than or equal to the number of sectors for full fast beamforming. Note that once a sector is pruned, its children sectors are automatically pruned during the later stages. Second, the pruned fast beamformer requires computations to calculate the test statistic. Signal detection requires beam energy computation which consists of N_p multiplications and $N_p - 1$ additions. Let L be the total number of processed beams over all stages. Then, the number of computations for calculating the energy is

$$D_{energy} = L(2N_p - 1). \tag{54}$$

To obtain the detection statistic t_s, two subtractions, two multiplications, and one division are required. The total number of computations for the detector at stage n is

$$D_{detect} = L(2N_p - 1) + 5(L - 2M). \tag{55}$$

Note that the detector begins at Stage 3, and the $2M$ beams corresponding to the first two stages are not used to compute a detection statistic. The total number of computations for the pruned fast beamforming is the sum of D_{fast} and D_{detect}. Therefore, the total number of computations for the pruned fast beamformer is

$$D = LN_p(F + I) + L(2N_p - 1) + 5(L - 2M). \tag{56}$$

If $N_p = M$,

$$D = LM(F + I) + L(2M - 1) + 5(L - 2M). \tag{57}$$

4.4 Simulation and Results

4.4.1 Wideband signal and array model

In the following simulation, we generate three wideband signals: a sinc function, a bandpass white Gaussian noise signal, and an ultra-wideband (UWB) source signal using the model in [62]. The sinc function is sampled at the rate of 300 Hz, which is three times the highest frequency of 100 Hz. The passband for the Gaussian noise is from 0.01 to 0.6 in normalized frequency. To generate the UWB signals, we use length-four PN codes, pulses of 0.2ns width and a duty cycle of 20%. The sampling rate of the UWB signals is 100GHz. We test the beamformer using a uniform linear array of 32 sensors spaced less than one half the shortest wavelength of the signal so that spatial aliasing is avoided.

4.4.2 Simulations

First, the single source case is considered. Figures 8 and 9 show the steered response of one sinc function coming from 20°. Figure 8 shows the steered response of the

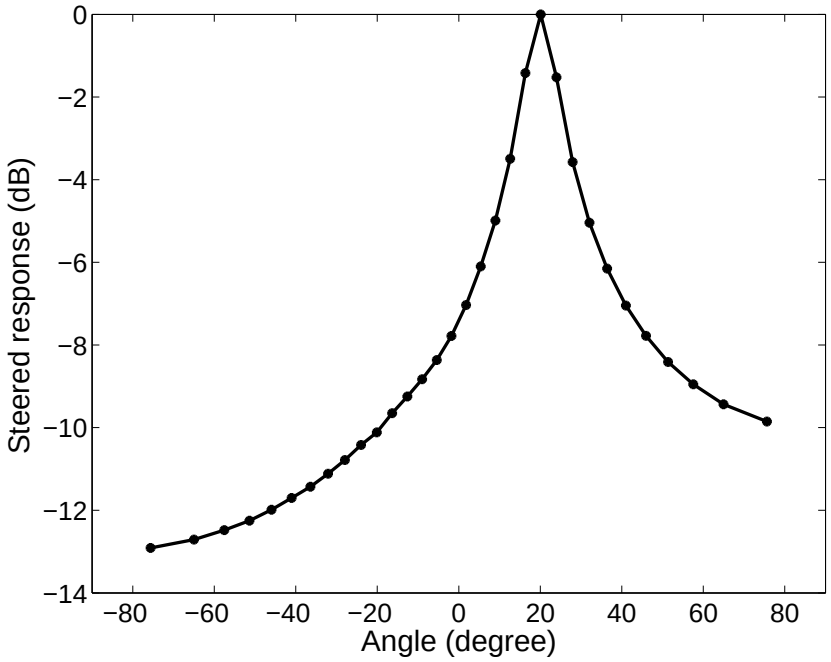

Figure 8: Steered responses of a conventional DS beamformer

conventional beamformer and Fig. 9 provides the response of the fast beamformer. The fast beamformer has a wider mainlobe and higher sidelobes than a conventional beamformer; This is the cost paid for less computations.

Figure 10 illustrates the steered response of fast beamforming at each stage with and without pruning. The upper row provides the fast beamformer output without pruning and the lower row with pruning. The left column shows the earliest stage and the right column shows the last stage of beamforming. Detection begins at Stage 3 because the noise is estimated at Stage 2. Clearly, many beams have been pruned between Stage 3 and Stage 4. The pruning step reduced the number of sectors by 12 and 28 at Stages 4 and 5, respectively.

Figure 11 summarizes the performance of the detector from 200 Monte-Carlo runs for the three signals. Figure 11 (a,c,e) shows plots of probability of detection versus detector parameter, ζ. Figure 11 (b,d,f) shows plots of the normalized number of flops vs probability of detection. The number of flops is normalized to that of a non-pruning fast beamformer. We used linear interpolation so that $F = 3$ and the number

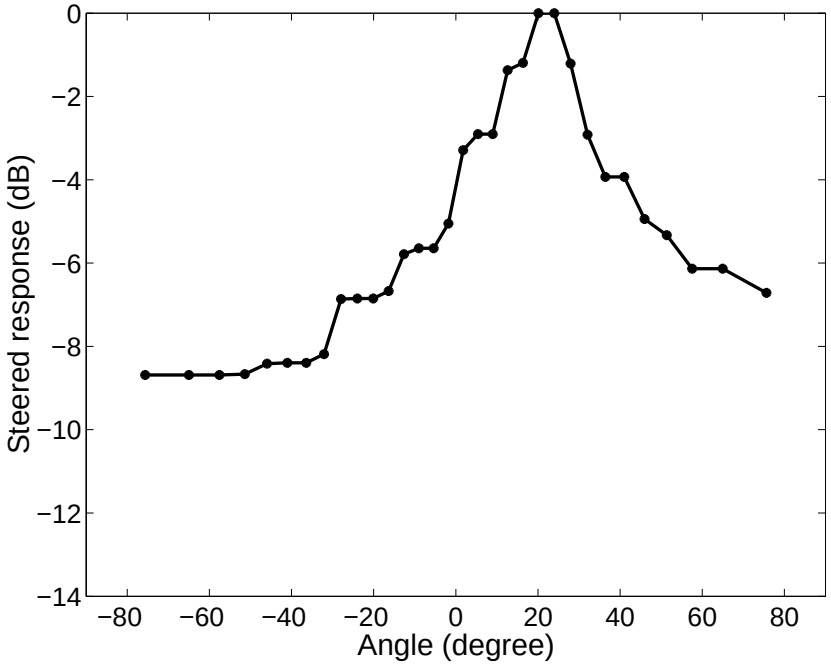

Figure 9: Steered responses of a fast DS beamformer

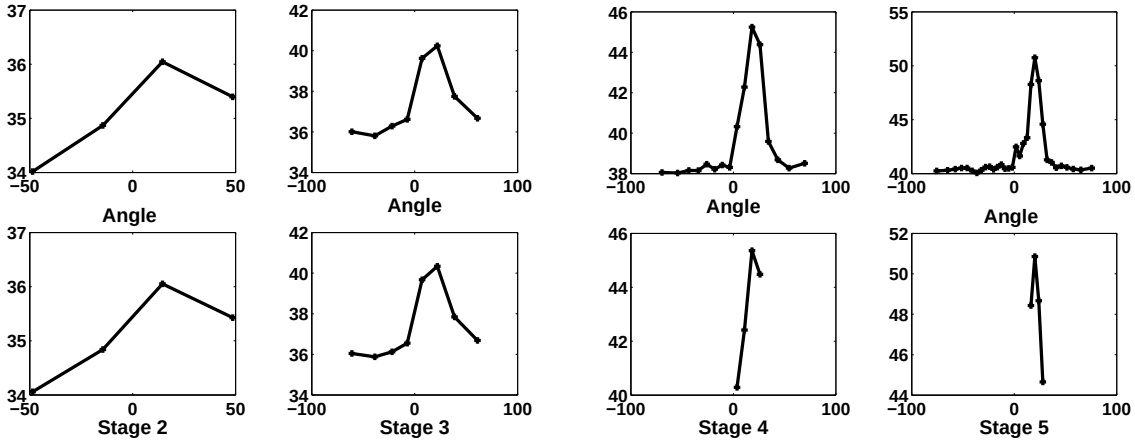

Figure 10: Steered response at each stage. From left to right, columns represent stages 2 through 5. Upper panels show regular fast beamforming and lower panels show prescreened (pruned) fast beamforming.

of snapshots was 400. We also used a two-tap lowpass filter which requires just one addition (I=1). Each signal and ζ setting was tested with five different SNRs. The detector works well even for the low SNR case, although the detector performance is different for each signal. In the bandpass Gaussian case, the probability of detection never reaches 100% even when ζ goes to zero. In general, the detector worked better with the UWB signal than others. However, the detection rate is very sensitive to changes in ζ. The fast beamformer saves nearly 23% of computations. The number of flops can be reduced further if less snapshots are used. However, a small number of snapshots may result in bad detection performance since more snapshots give better statistics. If there were more stages due to more array elements, the computational savings could be even larger. As expected, a small value of ζ gives better detection performance at the expense of more computations.

Figure 12 shows steered responses when two sinc signal sources are present at 12° and -20°. The steered responses at all stages are plotted together in one figure. However, in Fig. 12(a), the two signals have the same power while in Fig. 12(b), one signal's power is twice as large as the other. Resolving two signals depends on the signals' angular separation, power difference, and SNR.

4.5 Error Analysis

The fast DS beamforming can reduce the number of computations by approximating regular DS beamforming, while the detector (46) is derived by assuming that intermediate stages of the fast beamforming represent perfect partial coherent sums. If there is one source in a sector, if the steering direction matched the signal's DOA, and if the beamforming is perfect, then the source signal is perfectly aligned during each fast beamforming stage. However, the beamforming angles at each stage usually do not match the signal's DOA and even if they match, due to approximation in fast beamforming, the source signal cannot be perfectly aligned. In this section, the effect

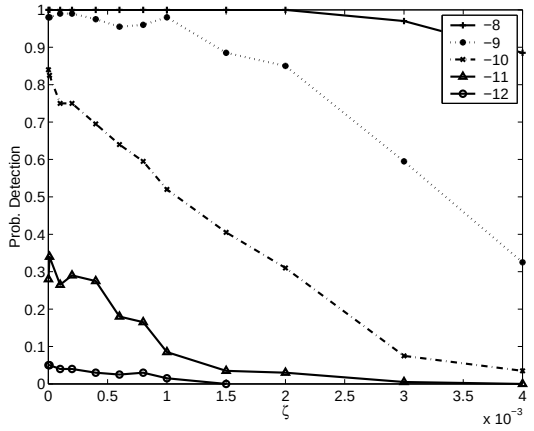

(a) Sinc

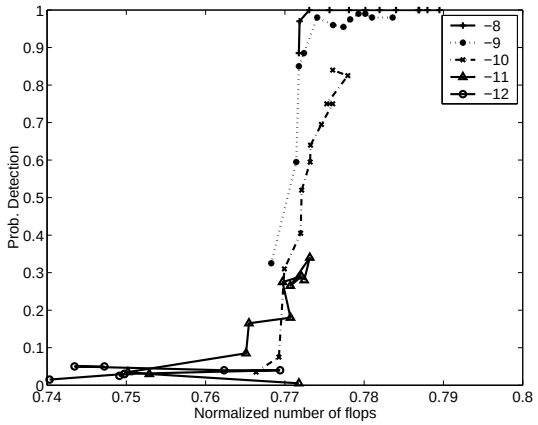

(b) Sinc

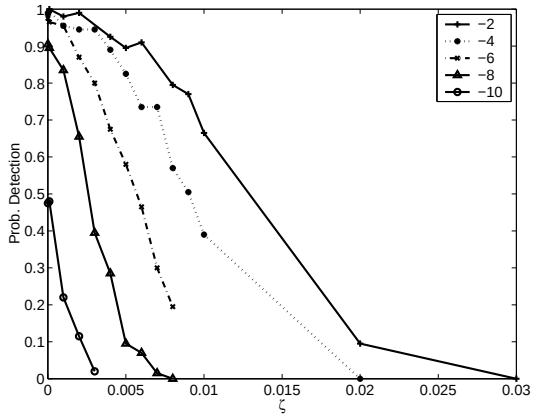

(c) Gaussian

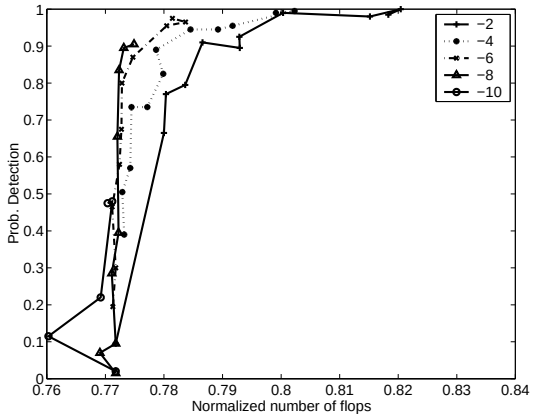

(d) Gaussian

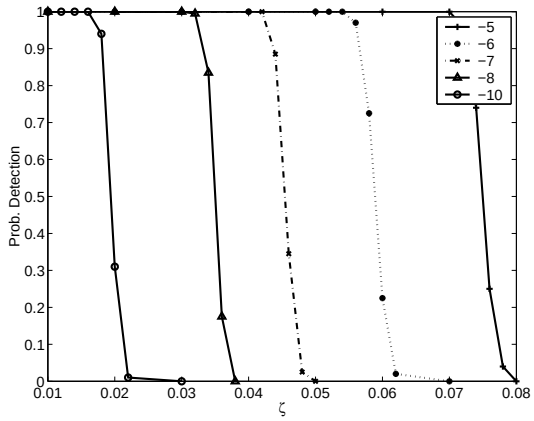

(e) UWB

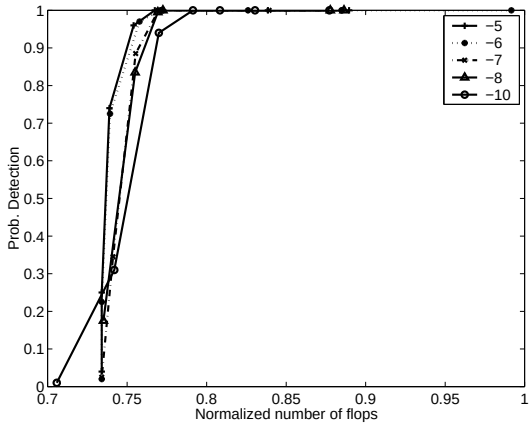

(f) UWB

Figure 11: Simulation results. The left column is plot of detection probability vs detector parameter, ζ,and the right column is plot of detection probability vs normalized number of flops for various SNRs.

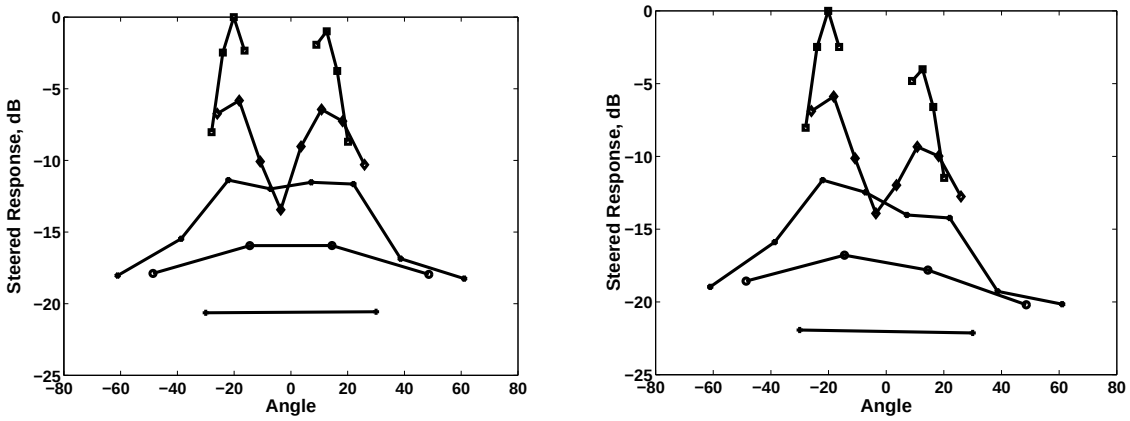

(a) (b)

Figure 12: Two signal cases. Steered response at all stages are plotted simultaneously. (a) Two equi-power signals and (b) different-power signals are located at 12° and −20° with SNR=0 dB.

of the beamforming errors on the detector performance is considered.

4.5.1 Detector Performance

First, it is necessary to find receiver operator characteristic (ROC) curves for the detector using the idealized scenario, e.g., the error-free case. The derivation of the ROC curves is similar to the approach in [26] for a detector in the quadtree image formation technique for SAR. The derivation ignores the fact that interpolation in the fast beamforming will correlate the noise. When the a-th subaperture at stage s is included in the b-th subaperture at stage $s + s'$, then

$$\mathrm{cov}\{v_{s,d,a}[n], v_{s+s',k,b}[m]\} = 2^s \sigma^2 \delta[n - m],$$

and the covariance between energy estimates is

$$\begin{aligned}\mathrm{cov}\{\hat{\varepsilon}_s, \hat{\varepsilon}_{s+s'}\} &= \mathrm{cov}\{\frac{1}{2^{M-s}}\sum_{a=1}^{2^{M-s}}\sum_{n}|V_{s,a}[n]|^2, \\ &\quad \frac{1}{2^{M-s-s'}}\sum_{b=1}^{2^{M-s-s'}}\sum_{m}|V_{s+s',b}[m]|^2\} \\ &= \frac{1}{2^{M-s}}\frac{1}{2^{M-s-s'}}2^{M-s-s'}2^{s'} \\ &\quad \cdot\mathrm{cov}\{\sum_{n}|v_{s,a}[n]|^2, \sum_{m}|v_{s+s',a}[m]|^2\} \end{aligned} \tag{58}$$

Note that the sector label d is omitted for notational convenience. Since the noise is uncorrelated,

$$\begin{aligned}&\mathrm{cov}\{\sum_{n}|v_{s,a}[n]|^2, \sum_{m}|v_{s+s',a}[m]|^2\} = \\ &\sum_{n}\mathrm{cov}\{|v_{s,a}[n]|^2, |v_{s+s',a}[n]|^2\}\end{aligned} \tag{59}$$

After using the following identity [26],

$$\mathrm{cov}\{x^2, y^2\} = 2\mathrm{cov}^2\{x, y\} + 4\mathrm{cov}\{x, y\}\varepsilon\{x\}\varepsilon\{y\}$$

the covariance between the squares of beams is

$$\mathrm{cov}\{|v_{s,a}[n]|^2, |v_{s+s',a}[n]|^2\} = 2(2^s\sigma^2)^2 + 4(2^s\sigma^2)2^{2s+s'}s^2(nT_s).$$

Therefore, (59) becomes

$$\mathrm{cov}\{\sum_{n}|v_{s,a}[n]|^2, \sum_{m}|v_{s+s',a}[m]|^2\} = 2^{2s+1}N\sigma^4 + 4\cdot 2^{3s+s'}\sigma^2 P \tag{60}$$

where

$$P = \sum_{n=0}^{N-1}|s(nT_s)|^2.$$

After substituting (60) into (58),

$$\mathrm{cov}\{\hat{\varepsilon}_s, \hat{\varepsilon}_{s+s'}\} = \frac{1}{2^{M-(s+s')}}(2^{2s+1}N\sigma^4 + 4\cdot 2^{3s+s'}\sigma^2 P) \tag{61}$$

The coherence detector is equivalent to comparing the statistic

$$\mathcal{T}(s) = \hat{\varepsilon}_{d,s} - \hat{\varepsilon}_{c,s-1} - 4^s\zeta(4\hat{\varepsilon}_{k,1} - \hat{\varepsilon}_{l,s})$$

to a threshold of zero. If $\mathcal{T}(s)$ is larger than zero, the detector assumes a coherent source. The expected value of $\mathcal{T}(s)$ is

$$E[\mathcal{T}(s)] = 4^s(\frac{1}{2}P - 4\zeta N\sigma^2).$$

We derive the variance of $\mathcal{T}(s)$, using the covariance expression from (61), to be

$$\text{var}\{\mathcal{T}(s)\} = \frac{N\sigma^4}{2^M}(2 \cdot 8^s + 128 \cdot 16^s\zeta^2 + 3 \cdot 16^s\rho)$$

where $\rho = P/(N\sigma^2)$ is the SNR. If N is sufficiently large, $\hat{\varepsilon}$ can be considered to have a Gaussian distribution. Then, $\mathcal{T}(s)$ is also Gaussian since it is a linear combination of Gaussian random variables. The probability of detection at Stage s is

$$\begin{aligned} P_d(s) &= \text{Prob}(\mathcal{T}(s) > 0 | P \neq 0) \\ &= Q\left(-E[\mathcal{T}(s)]/\sqrt{\text{var}\{\mathcal{T}(s)\}}\right) \\ &= Q\left(\frac{-\sqrt{N}4^s(\frac{1}{2}\rho - 4\zeta)}{\sqrt{2^{-M}(2 \cdot 8^s + 128 \cdot 16^s\zeta^2 + 3 \cdot 16^s\rho)}}\right), \end{aligned}$$

and the false alarm probability at Stage s is

$$\begin{aligned} P_{fa}(s) &= \text{Prob}(\mathcal{T}(s) > 0 | P = 0) \\ &= Q\left(-E[\mathcal{T}(s)]/\sqrt{\text{var}\{\mathcal{T}(s)\}}\right) \\ &= Q\left(\frac{\sqrt{N}4^{s+1}\zeta}{\sqrt{2^{-M}(2 \cdot 8^s + 128 \cdot 16^s\zeta^2)}}\right), \end{aligned}$$

where the error function $Q(x)$ is defined as

$$Q(x) = \frac{1}{\sqrt{2\pi}}\int_{-\infty}^{x} e^{-\frac{1}{2}x^2}dx.$$

4.5.2 Energy Loss

As mentioned earlier, the detector performance in the previous section is for the ideal case where the steering direction matches the signal's DOA and there is no error

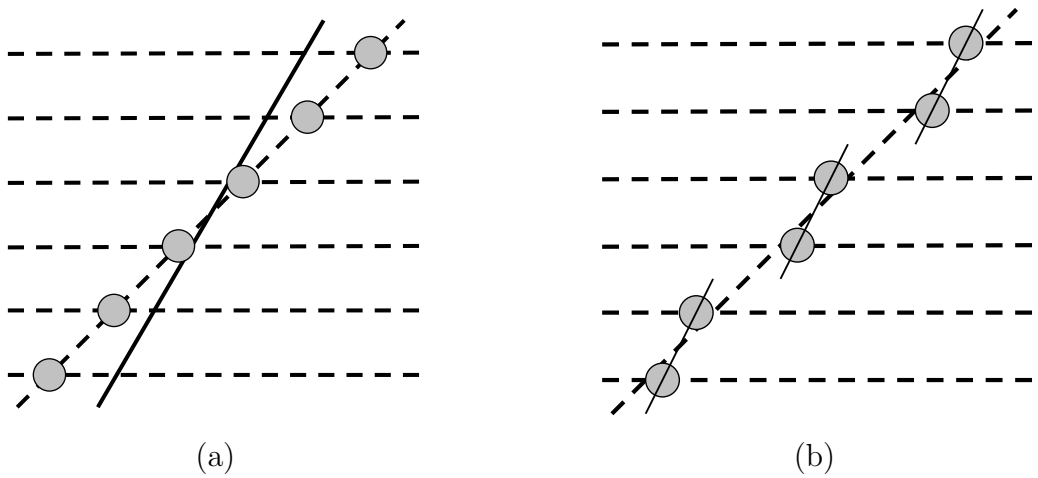

Figure 13: Misalignment. (a) steering direction mismatch, (b) fast beamforming approximation.

in the beamforming process. However, the fast beamformer is not perfect because there are shifting errors, which cause energy loss in a steered beam. There are two causes of shifting error: 1) misalignment between the DOA and the steering angle, and 2) approximation errors during the intermediate stages of fast beamforming. The following sections analyze these two errors and quantify their effect on the detector. This section models the wideband signal as a sinc waveform and considers the array to be a ULA.

4.5.2.1 Steering Loss

Steering angle mismatch is a common error in beamforming when the steering direction needs to be decided in advance. There is always some mismatch error in fast beamforming even if the signal is present in the processing sector. Figure 13(a) illustrates this error. The dashed diagonal line represents the required amount of time-shift for each sensor, and the solid line represents the time-shift for beamforming toward the phase center of the sector. As mentioned in the previous section, the beam energy ε_s is the sum of squared beam in the time domain. Let $x_m[n]$ be the m-th sensor output at the n-th sample. Assume that the sensor is discrete and the

sampling rate is equal to the Nyquist rate. Then, the Fourier transform of $x_m[n]$ over the time domain is

$$X_m(\omega) = S(\omega)\exp(-j\frac{\omega md}{c}\sin\theta),$$

where θ is the signal's DOA. After steering towards $\hat{\theta}$, the Fourier transform of the steered sensor output is

$$X_m(\omega) = S(\omega)\exp(-j\frac{\omega md}{c}\Delta u),$$

where $\Delta u = \sin\theta - \sin\hat{\theta}$. Assuming that the sensor spacing d is equal to $\lambda_{min}/2$, where λ_{min} is the wavelength of the highest frequency component of the signal source, then

$$X_m(\omega) = S(\omega)\exp(-j\omega m\Delta u).$$

The Fourier transform of $X_m(\omega)$ over the spatial domain is

$$X(k,\omega) = S(\omega)\sum_{m=0}^{M-1}\exp(-j\omega m\Delta u)\exp(jkm). \tag{62}$$

The energy of steered beam for uniform weights is simply

$$\varepsilon = \frac{1}{2\pi}\int_{-\pi}^{\pi}|X(0,\omega)|^2\,d\omega$$

In other words, the beam energy is the integral of $X(k,\omega)$ along the ω-axis. Assume that the signal source is a critically sampled sinc function so that $S(\omega) = \gamma$ is a constant. Then, using (62) for $k = 0$, the beam energy can be expressed as

$$\varepsilon = \frac{\gamma^2}{2\pi}\int_{-\pi}^{\pi}\left|\frac{\sin(\frac{M}{2}\omega\Delta u)}{\sin(\frac{1}{2}\omega\Delta u)}\right|^2 d\omega \tag{63}$$

The difference between DOA and steering direction in the sine domain, i.e., Δu, determines the energy loss. Because the sector size is $2/L$ in the $\sin\theta$ domain for fast beamforming, the maximum possible value of Δu is $1/L$. Therefore, the worst case energy ε_{min} is

$$\varepsilon_{min} = \frac{\gamma^2}{2\pi}\int_{-\pi}^{\pi}\left|\frac{\sin\frac{\omega}{2}}{\sin\frac{1}{2M}}\right|^2 d\omega.$$

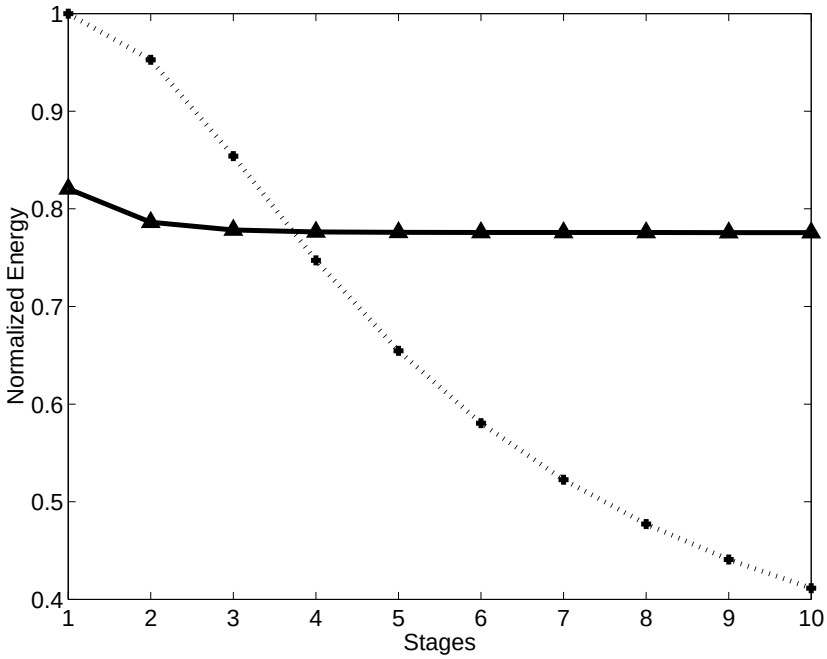

Figure 14: Energy loss. represents loss from steering direction mismatch and the dotted line represents it from fast beamforming approximation with matched steering angle.

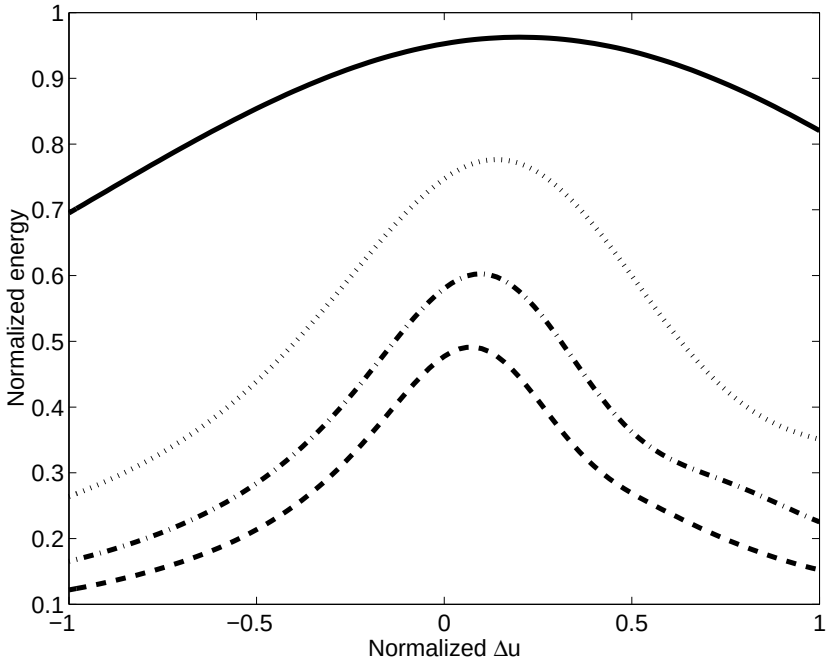

Figure 15: Combined energy loss at various stage. X-axis is the normalized Δu

4.5.2.2 Propagation of Alignment Error

During each stage, fast beamforming assumes that the there is enough alignment to coherently sum adjacent subapertures. Once the subapertures are combined, the error caused by the offset between the signal direction and the sector phase center becomes fixed. (Fig. 13 (b)). The beamforming loss can be calculated by analyzing the difference between the true and virtual sensor positions. The l-th sensor position at Stage s is

$$w_l^{(s)} = 2^s \left(l + \frac{1}{2} \right) - \frac{M}{2}$$

for $l = 0, 1, 2, \ldots, M/2^s - 1$. The steered beam at Stage s is

$$v_{s,d,l}[n] = v_{s-1,a,2l}[n + w_{2l}^{s-1}\mu_s] + v_{s-1,a,2l+1}[n + w_{2l+1}^{s-1}\mu_s],$$

where $\mu_s = \pm 1/2^s$. If d is odd, μ_s is positive; otherwise, it is negative. The steered beam at Stage s is

$$v_{s,d,l}[n] = \sum_{j=0}^{2^s-1} x_j \left[n + \sum_{i=0}^{s-1} w_{\lfloor l/2^i \rfloor}^{(i)} \mu_i \right] \tag{64}$$

where $\lfloor \beta \rfloor$ is the largest integer which does not exceed β. The steering direction is $\hat{\theta} = \sin^{-1}(\sum \mu_i)$.

If we assume that the steering direction matches the source's DOA, and $y[n]$ is the sampled source signal, then (64) becomes

$$v_{s,d,l}[n] = \sum_{i=0}^{2^s-1} y[n + a_i] \tag{65}$$

where

$$a_i = \sum_{l=1}^{s-1} (w_{\lfloor i/2^l \rfloor}^{(l)} - w_i^{(0)}) \mu_l \tag{66}$$

The dotted line in Fig. 14 shows the energy loss at Stages 1 through 10. At Stage 1 there is no loss due to beamforming since the sensor positions have not been changed.

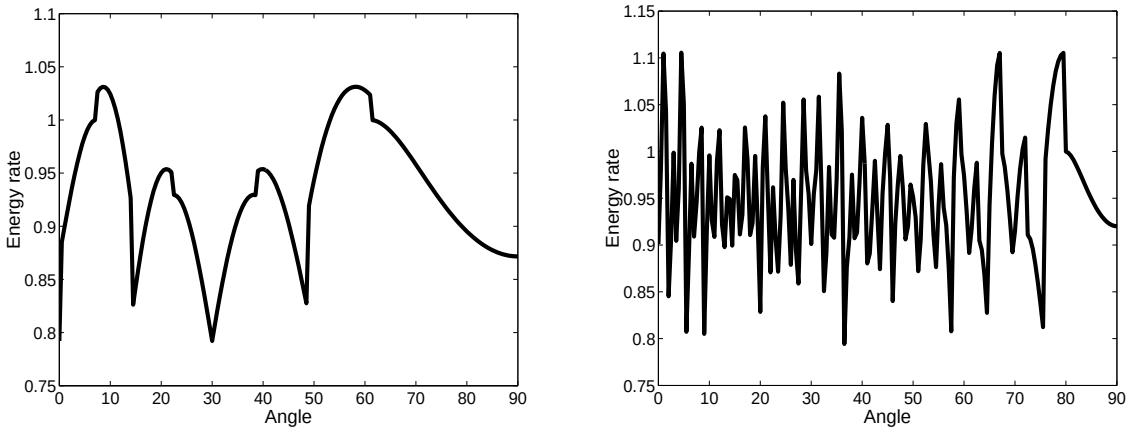

(a) (b)

Figure 16: ELF rate. (a) α_3/α_2 (b) α_6/α_5

4.5.2.3 Combined loss

The effect of the two shifting errors can be calculated by just adding Δu in (65) to form the combined error

$$v_{s,d,l}[n] = \sum_{i=0}^{2^s-1} y[n + w_i^{(0)}\Delta u + a_i].$$

Figure 15 shows the normalized energy at various stages where these two shifting errors are combined. If the normalized energy is one, it means that there is no energy loss. The x-axis is normalized to $1/2^s$ which is the largest Δu at Stage s.

4.5.3 Signal Detector

Due to the energy loss, the beam energy at Stage s can be represented as

$$E[\hat{\varepsilon_s}] = 4^s\alpha_s(\theta)P + 2^sN\sigma^2$$

where $\alpha_s(\theta)$ is the energy loss factor (ELF), which is the normalized energy shown in Figure 15. The numerator of the detection statistic is

$$\begin{aligned} \varepsilon_{c,s} - 2\varepsilon_{d,s-1} &= 4^s\alpha_s(\theta)P - 2\cdot 4^{s-1}\alpha_{s-1}(\theta)P \\ &= 4^s\left(\frac{\alpha_s(\theta)}{\alpha_{s-1}(\theta)} - \frac{1}{2}\right)P \end{aligned} \tag{67}$$

If α_s/α_{s-1} is less than 1/2, the detector statistic is negative and the detector will fail to detect the target. Figure 16 provides plots of α_3/α_2 and α_6/α_5 versus θ. In general, the ELF rate varies greatly as a function of DOA. Therefore, the probability of detection depends on the signal's DOA. In general, the ELF rate never dips below the critical value of 1/2, so the detector works through all the stages. Using the ELF, one can calculate probability of detection and false alarms for the nonideal beamforming case.

4.5.4 New Detector Statistics

In this section, we recalculate the statistics of the detector by considering energy loss and by slightly modifying the analysis in Section 4.5.1. The second term in (60) is derived from

$$4 \cdot 2^{3s+s'}\sigma^2 P = 4 \cdot 2^s \sigma^2 \sum_{n=1}^{N} \varepsilon\{V_s[n]\}\varepsilon\{V_{s+s'}[n]\} \tag{68}$$

Since there are misalignments in $V_s[n]$, the summation is no longer $2^{2s+s'}P$, which is $\sum 2^{2s+s'}y^2[n]$. It is not easy to get the value exactly. We introduce a new factor $\beta_{s,s+s'}$ such that $0 < \beta_{s,s+s'} < 1$ that includes all the energy loss of the beamformer. Then,

$$\sum_{n=0}^{N-1} E[V_s[n]]E[V_{s+s'}[n]] = 2^{2s+s'}\beta_{s,s+s'}P$$

The new factor $\beta_{s,s+s'}$ depends on the stage number s, the stage displacement s', the DOA θ, and the steering direction $\hat{\theta}$. The covariance (61) is

$$\mathrm{cov}\{\hat{\varepsilon}_s, \hat{\varepsilon}_{s+s'}\} = \frac{1}{2^{S-(s+s')}}(2^{2s+1}N\sigma^4 + 4 \cdot 2^{3s+s'}\sigma^2\beta_{s,s+s'}P)$$

Now, the expected value of $\mathcal{T}(s)$ is

$$\begin{aligned} E[\mathcal{T}(s)] &= 4^s(\alpha_s - 0.5\alpha_{s-1} - 16\tau(\alpha_2 - \alpha_1))P - 4^{s+1}\tau N\sigma^2 \\ &= 4^s N\sigma^2((\alpha_s - 0.5\alpha_{s-1} - 16\tau(\alpha_2 - \alpha_1))\rho - 4\tau), \end{aligned} \tag{69}$$

and the variance is

$$\begin{aligned}
\mathrm{var}\{\mathcal{T}(s)\} &= 2^{3s}P\sigma^2\left\{4\alpha_s + 2\alpha_{s-1} - 2^{s-S+1}\beta_{s,s-1}\right. \\
&\quad \left. +128\cdot 2^s\tau^2(4\alpha_1 + 2\alpha_2 - 2^{-S}\beta_{1,2})\right\} \\
&\quad +2^{2s}N\sigma^4\{4 - 2^{s-S} + 2^{2s}\tau^2 16(10 - 2^{-S})\} \\
&= 2^{2s}N\sigma^4\left\{2^s\left(4\alpha_s + 2\alpha_{s-1} - 2^{s-S+1}\beta_{s,s-1}\right.\right. \\
&\quad \left.\left. +128\cdot 2^{2s}\tau^2(4\alpha_1 + 2\alpha_2 - 2^{-S}\beta_{1,2})\right)\rho\right. \\
&\quad \left. +4 - 2^{s-S} + 2^{2s}\tau^2 16(10 - 2^{-S})\right\} \qquad (70)
\end{aligned}$$

In (70), the covariance between $\mathcal{S}(s)$ and $\mathcal{N}(s)$ is set to zero since it is close to zero.

$$\begin{aligned}
\mathrm{cov}\{\mathcal{S}(s)\mathcal{N}(s)\} &= 2^{s+6}\sigma^2 P(\beta_{s,1} + \beta_{s-1,2} - \beta_{s,2} - \beta_{s-1,1}) \\
&\cong 0.
\end{aligned}$$

Figure 17 shows how the energy loss deteriorates the detector performance by comparing performance curves with the loss-free detector. The parameters are $\beta_{s,s-1} = 0.9$, $\beta_{1,2} = 0.8$, $s = 3$, and $S = 5$. The signal's DOA is 20°. In all three plots, the dashed line is for the ideal case and the dotted line is the practical case where energy losses exist. As N increases, the probability of false alarm decreases and as expected, low SNR has small probability of detection. Apparently, these probabilities also depend on DOA. However, since we know the ELF for all DOA's, we can get the performance plot for every direction. Figure 17 (c) is the ROC curve of the detector when the SNR is -12dB. Note that the energy loss degraded the performance significantly. For low SNR case, this performance difference would be even larger. However, the detector never fails to work despite the energy losses.

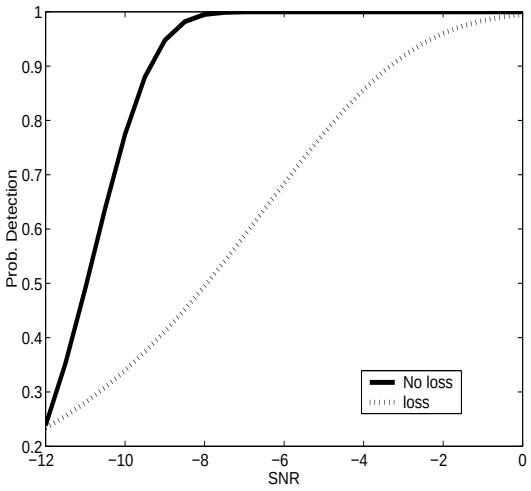

(a) P_d vs SNR

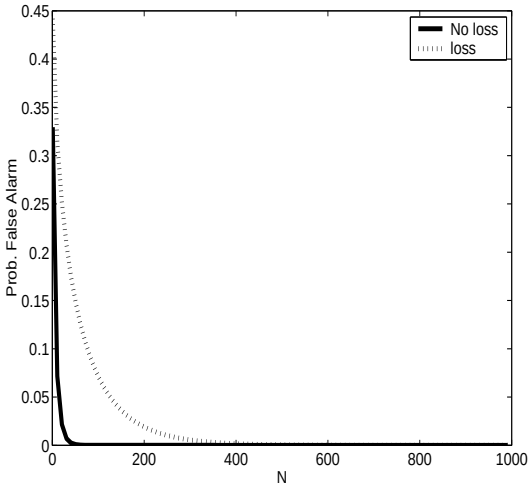

(b) P_{fa} vs. N

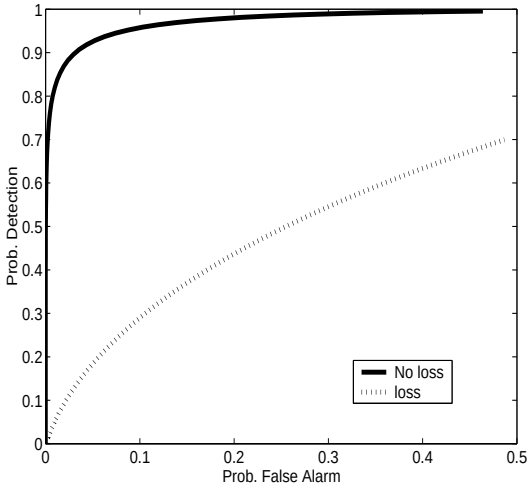

(c) P_d vs. P_{fa}

Figure 17: Detector performance. (a) probability of detection vs. SNR. (b) probability of false alarm vs the number of snapshots. (c) ROC curve. The dashed line is the ideal case and the dotted line is with energy loss. In (a) and (b), ζ is fixed while in (c) the SNR and N is fixed

CHAPTER 5

TOPS: NEW WIDEBAND DOA ESTIMATOR

In this chapter, a new wideband DOA estimation technique is introduced. The new method, which is called TOPS (Test of Orthogonality of Projected Subspaces), can circumvent the disadvantages of both the incoherent and the coherent wideband methods.

5.1 Theory

Like previous wideband methods, the new estimator uses frequency-dependent sensor outputs whose structure is the same as (31).

$$\mathbf{X}(\omega_i) = \mathbf{A}(\omega_i, \boldsymbol{\theta})\mathbf{S}(\omega_i) + \mathbf{N}(\omega_i),\ i = 1, 2, \ldots, K.$$

Initially, only 1-D linear arrays will be considered, but the sensor locations do not need to be uniform. However, the array manifolds corresponding to different DOAs should be independent. Later, multidimensional arrays will be considered. Like CSSM and WAVES, TOPS also uses a transformation matrix to exploit multiple frequency components. However, there are two notable differences with respect to other methods. First, in TOPS, only the noise subspaces of multiple frequencies are used while the two previous methods use multiple signal subspaces or both subspaces. Second, the transformation matrix depends on the array manifold vector, not on the signal subspaces. The previous methods try to transform the whole signal subspace for one frequency into that of another frequency, which requires complete knowledge of the original subspace. TOPS tries to transform a single array manifold vector in the signal subspace instead of the whole signal subspace. This can reduce errors during the transformation step since we might not know much about the signal subspace.

If the m-th element of an array manifold at an arbitrary frequency ω_i with an arbitrary DOA θ_i is multiplied by the m-th element of that with a different DOA θ_j and the frequency is ω_j, then

$$\begin{aligned}[\mathbf{a}(\omega_i,\theta_i)]_m[\mathbf{a}(\omega_j,\theta_j)]_m &= e^{-j\omega_i v_{m-1}\sin\theta_i}\cdot e^{-j\omega_j v_{m-1}\sin\theta_j} \\ &= e^{-jv_{m-1}(\omega_i+\omega_j)(\frac{\omega_i\sin\theta_i}{\omega_i+\omega_j}+\frac{\omega_j\sin\theta_j}{\omega_i+\omega_j})},\end{aligned} \tag{71}$$

where $[\cdot]_m$ denotes the m-th element of the vector. We can rewrite (71) as

$$[\mathbf{a}(\omega_i,\theta_i)]_p[\mathbf{a}(\omega_j,\theta_j)]_p = e^{-j\omega_k v_{p-1}\sin\theta_k},$$

where

$$\begin{aligned}\omega_k &= \omega_i+\omega_j, \\ \sin\theta_k &= \frac{\omega_i}{\omega_k}\sin\theta_i+\frac{\omega_j}{\omega_k}\sin\theta_j.\end{aligned}$$

Now the following Lemma is stated:

Lemma 1 *For a linear array manifold* $\mathbf{a}(\omega_i,\theta_i)$*, there exists a matrix* $\mathbf{\Phi}(\omega_j,\theta_j)$ *such that*

$$\mathbf{a}(\omega_k,\theta_k) = \mathbf{\Phi}(\omega_j,\theta_j)\mathbf{a}(\omega_i,\theta_i) \tag{72}$$

where

$$\mathbf{\Phi}(\omega_j,\theta_j) = diag\{\mathbf{a}(\omega_j,\theta_j)\}$$

Then, the relationships between frequencies and DOAs are

$$\omega_k = \omega_i+\omega_j, \tag{73}$$

$$\sin\theta_k = \frac{\omega_i}{\omega_k}\sin\theta_i+\frac{\omega_j}{\omega_k}\sin\theta_j. \tag{74}$$

This Lemma means that by multiplying $\mathbf{\Phi}(\omega, \theta)$ by the proper values of ω and θ, we can transform an array manifold of any frequency and any DOA into that of the desired frequency and DOA. Note that if $\theta_i = \theta_j$, then $\theta_k = \theta_i$. In other words, if θ_j in $\mathbf{\Phi}$ is same as the original DOA θ_i, we can transform the array manifold of frequency i into that of frequency k without changing the DOA θ_i. This fact is the key idea of TOPS. For notational convenience, from now on, $\mathbf{A}(\omega_i, \boldsymbol{\theta})$ and $\mathbf{a}(\omega_i, \theta_j)$ will be represented as $\mathbf{A}_i(\boldsymbol{\theta})$ and $\mathbf{a}_i(\theta_j)$, respectively.

Lemma 2 *Let $\Delta\omega = \omega_j - \omega_i$. Then,*

$$\mathcal{R}\{\mathbf{\Phi}(\Delta\omega, \phi)\mathbf{F}_i\} = \mathcal{R}\{\mathbf{A}(\omega_j, \hat{\boldsymbol{\theta}})\}$$

where $\mathcal{R}\{\cdot\}$ denotes the range of the matrix and

$$\left[\hat{\boldsymbol{\theta}}\right]_i = \arcsin\left\{\frac{\omega_i}{\omega_j}\sin\theta_i + \frac{\Delta\omega}{\omega_j}\sin\phi\right\}$$

proof: By Lemma 1 and the fact that the range space of $\mathbf{F}_i$ and $\mathbf{A}_i$ is the same, we can easily show that

$$\begin{aligned}\mathbf{\Phi}(\Delta\omega, \phi)\mathbf{F}_i &= \mathbf{\Phi}(\Delta\omega, \phi)\mathbf{A}_i(\boldsymbol{\theta})\mathbf{G}_i \\ &= \mathbf{A}_j(\hat{\boldsymbol{\theta}})\mathbf{G}_i, \end{aligned} \tag{75}$$

where $\mathbf{G}_i$ is a full rank square matrix. Therefore, the lemma holds. ■

This observation is the main idea of the following theorem.

Theorem 1 *Assume that $2P \leq M$ and $K \geq P+1$. Let $\mathbf{U}_i(\phi)$ be $M \times P$ matrix for $i = 2, \ldots, K$ such that*

$$\mathbf{U}_i(\phi) = \mathbf{\Phi}(\Delta\omega_i, \phi)\mathbf{F}_1 \tag{76}$$

where $\Delta\omega_i = \omega_i - \omega_1$. Note that ϕ here is the hypothesized azimuth angle, not the elevation angle. Define a $P \times (K-1)(M-P)$ matrix $\mathbf{D}(\phi)$ such that

$$\mathbf{D}(\phi) = [\ \mathbf{U}_2^H\mathbf{W}_2\ \mathbf{U}_3^H\mathbf{W}_3\ \ldots\ \mathbf{U}_K^H\mathbf{W}_K\ ] \tag{77}$$

Then,

a) if $\phi = \theta_l$ for some l, $\mathbf{D}(\phi)$ loses its rank (singular).

b) if $\mathbf{D}(\phi)$ is singular, $\phi = \theta_l$ for some l.

Proof: The theorem says that $\phi = \theta_l$ for some l is the only case where the $\mathbf{D}(\phi)$ becomes singular. The statements a) and b) should be proved independently.

Proof of a): Let ϕ be equal to the l-th DOA θ_l. Since $\mathbf{W}_i$ is the noise subspace $\mathbf{A}_i^H \mathbf{W}_i = \mathbf{0}$, it is true that

$$\mathbf{a}_i^H(\theta_l)\mathbf{W}_i = \mathbf{0}^T$$

for all $l = 0, 1, \ldots, P-1$ and $i = 1, 2, \ldots, K-1$. By Lemma 2, we know that

$$\mathbf{U}_i = \Phi(\Delta\omega_i, \phi)\mathbf{A}_1\mathbf{G}_1 = \mathbf{A}_i(\hat{\boldsymbol{\theta}}_{\boldsymbol{i}})\mathbf{G}_1$$

where

$$[\hat{\boldsymbol{\theta}}_i]_p = \arcsin\left\{\frac{\omega_1}{\omega_i}\sin\theta_p + \frac{\Delta\omega_i}{\omega_i}\sin\phi\right\} \tag{78}$$

for $p = 0, 1, \ldots, P-1$. Since $\phi = \theta_l$,

$$[\hat{\boldsymbol{\theta}}_2]_l = \ldots = [\hat{\boldsymbol{\theta}}_K]_l = \theta_l$$

Therefore, for $i = 2, \ldots, K$,

$$\begin{aligned}
\mathbf{U}_i^H\mathbf{W}_i &= \mathbf{G}_1^H \begin{bmatrix} \mathbf{a}_i^H([\hat{\boldsymbol{\theta}}_i]_0)\mathbf{W}_i \\ \vdots \\ \mathbf{a}_i^H(\theta_l)\mathbf{W}_i \\ \vdots \\ \mathbf{a}_i^H([\hat{\boldsymbol{\theta}}_i]_{P-1})\mathbf{W}_i \end{bmatrix} \\
&= \mathbf{G}_1^H \begin{bmatrix} * \\ \mathbf{0}^T \\ * \end{bmatrix} \leftarrow l\text{-th row}
\end{aligned} \tag{79}$$

Then, the $\mathbf{D}$ matrix becomes

$$\mathbf{D} = [\mathbf{U}_2^H \mathbf{W}_2 \ \ldots \ \mathbf{U}_K^H \mathbf{W}_K] = \mathbf{G}_1^H \begin{bmatrix} * & \cdots & * \\ \mathbf{0^T} & \cdots & \mathbf{0^T} \\ * & \cdots & * \end{bmatrix} \leftarrow l\text{-th row.}$$

and it loses rank. This proves that $\phi = \theta_l$ is a sufficient condition for $\mathbf{D}$ to become singular.

Proof of b): Suppose that the $\mathbf{D}(\phi)$ matrix is rank-deficient and ϕ is not the same as any of the DOAs . Since $\mathbf{D}(\phi)$ has more columns than rows, and $\mathbf{G}_0$ is a nonsingular square matrix, the row vectors of the following matrix should be linearly dependent.

$$\mathbf{L} = \begin{bmatrix} \mathbf{L}_2 & \cdots & \mathbf{L}_K \end{bmatrix} \tag{80}$$

where

$$\mathbf{L}_i = \mathbf{A}_i^H(\hat{\boldsymbol{\theta}}_i)\mathbf{W}_i.$$

There are two cases that we need to consider. The first case is when none of the $\hat{\theta}$'s match the DOAs. The other is the case where some of $\hat{\theta}$'s are the same as one of the DOAs (ambiguity). Since the individual block matrices $\mathbf{L}_i$ can be either full rank or rank-deficient, we need to consider both cases independently.

CASE I

Assume that all $\hat{\theta}$'s are different from the DOAs, Then, there is no zero row vector in $\mathbf{L}_i$. With slight abuse of the notation, let $\hat{\mathbf{A}}_i = \mathbf{A}_i(\hat{\boldsymbol{\theta}}_i)$ and $\mathbf{A}_i = \mathbf{A}_i(\boldsymbol{\theta}_i)$. Define $\mathbf{B}$ and $\mathbf{C}$ as

$$\mathbf{B} = \begin{bmatrix} \mathbf{A}_i & \hat{\mathbf{A}}_i \end{bmatrix}$$

and

$$\mathbf{C} = \begin{bmatrix} \mathbf{A}_i & \mathbf{W}_i \end{bmatrix}$$

Since $P < M/2$, the rank of $\mathbf{B}$ and the rank of $\mathbf{C}$ are $2P$ and M, respectively. If we multiply both matrices

$$\mathbf{B}^H\mathbf{C} = \begin{bmatrix} \mathbf{A}_i^H \\ \hat{\mathbf{A}}_i^H \end{bmatrix} \begin{bmatrix} \mathbf{A}_i & \mathbf{W}_i \end{bmatrix} = \begin{bmatrix} \mathbf{A}_i^H\mathbf{A}_i & \mathbf{0} \\ \hat{\mathbf{A}}_i^H\mathbf{A}_i & \mathbf{L}_i \end{bmatrix},$$

then, Sylvester's inequality states that the rank of $\mathbf{B}^H\mathbf{C}$ should be bounded by [11]

$$\gamma(\mathbf{B}) + \gamma(\mathbf{C}) - M \leq \gamma(\mathbf{B}^H\mathbf{C}) \leq \min(\gamma(\mathbf{B}), \gamma(\mathbf{C}))$$

where $\gamma(\cdot)$ denotes rank of a matrix. Therefore,

$$2P + M - M \leq \gamma(\mathbf{B}^H\mathbf{C}) \leq \min(2P, M)$$

In other words, $\mathbf{B}^H\mathbf{C}$ is always full rank. Since the upper right block is a zero matrix, $\mathbf{L}_i$ is always full rank and the row vectors in $\mathbf{L}_i$ are independent for all i (Note that $\mathbf{L}_i$ has more columns than rows). This proves the non-singularity of $\mathbf{L}$. Therefore, it is proved that if the $\mathbf{D}$ matrix is singular, at least one $\hat{\theta}$ is the same as the DOA. Note that for the case where $2P > M$, we cannot guarantee that $\mathbf{L}$ still has independent rows.

CASE II

This is the case where some of the angles $\hat{\theta}$ are the same as DOAs but ϕ is not same as any of DOAs. Of course, this happens when the hypothesized ϕ is the same as one of DOAs. However, in the multiple-source case, there is an ambiguity when $\hat{\theta}$ happens to be the same as one of the DOAs even if the hypothesized ϕ does not match any of DOAs. For example, let $[\hat{\boldsymbol{\theta}}_i]_l$ be the l-th DOA of $\hat{\mathbf{A}}_i$. If ϕ is not same as any of θ's, it is still possible that, for $l \neq n$, $[\hat{\boldsymbol{\theta}}_i]_l = \theta_n$ since

$$[\hat{\boldsymbol{\theta}}_i]_l = \arcsin\left\{\frac{\omega_1}{\omega_i}\sin\theta_l + \frac{\omega_i - \omega_1}{\omega_i}\sin\phi\right\}. \tag{81}$$

In this case, $\mathbf{L}_i$ loses its rank since its l-th row will be zero. Note that this is the only case where $\mathbf{L}_i$ becomes singular. Otherwise, $\mathbf{L}_i$ is proved to be a full rank matrix in the proof of case I. Without loss of generality, let's assume that $[\hat{\boldsymbol{\theta}}_2]_l = \theta_n$. Then,

$$\mathbf{e}_l^H \mathbf{L}_1 = \mathbf{0}^T,$$

where $\mathbf{e}_l$ is a vector whose elements are zero except for the l-th element which is one. Any null space of $\mathbf{L}_i$ can be spanned by $\mathbf{e}_l$. If $\mathbf{L}$ is singular,

$$\bigcap_{i=2}^{K} \mathcal{LN}\left\{\mathbf{L}_i\right\} \neq \emptyset. \tag{82}$$

where $\mathcal{LN}\{\cdot\}$ denotes the left null space. Since the $\mathbf{e}_l$'s form an orthogonal set, (82) is equivalent to saying that there exists a vector $\mathbf{e}_l$ such that $\mathbf{e}_l^H \mathbf{L}_i = \mathbf{0}^T$ for all $i = 2, \ldots, K$ implying that $[\hat{\boldsymbol{\theta}}_i]_l$ equals to one of the DOAs for all i. Since the right hand side of (81) is monotonically increasing or decreasing, $[\hat{\boldsymbol{\theta}}_i]_l \neq [\hat{\boldsymbol{\theta}}_j]_l$ as long as $i \neq j$. Since it is assumed that $\phi \neq \theta_l$, $[\hat{\boldsymbol{\theta}}_i]_l \neq \theta_l$, and $[\hat{\boldsymbol{\theta}}_i]_l$ can be the same as one of the DOAs at most $P-1$ times. Therefore, if $K - 1 > P$, there does not exist a vector $\mathbf{e}_l$ such that $\mathbf{e}_l^H \mathbf{L}_i = \mathbf{0}^T$ for all $i = 2, \ldots, K$ and $\mathbf{L}$ is nonsingular as long as $\phi \neq \theta_l$ for all l. We can conclude that $\mathbf{D}(\phi)$ is singular if and only if $\phi = \theta_l$ for some l. ■

The foregoing theorem ensures that the DOA of the signals can be found by looking for the element ϕ that makes $\mathbf{D}(\phi)$ singular.

5.2 Extension to Multidimensional Arrays

In the previous section, TOPS was applied to 1-D linear arrays only. In this section, it is generalized to arbitrary multidimensional arrays. Even though we say *arbitrary* arrays, it is assumed that the array manifold vectors of different DOAs should be mutually independent and the distance between sensors should be close enough to avoid spatial aliasing like the linear array case. In order to work with arbitrary arrays, the following two conditions should hold:

1. There always exists a transformation matrix such that

$$\mathbf{a}(\omega_k, \theta) = \mathbf{\Phi}(\omega_i, \theta)\mathbf{a}(\omega_j, \theta)$$

2. The $\mathbf{D}(\phi)$ matrix should be nonsingular if ϕ is not the same as any DOA.

Condition 1) ensures that $\mathbf{D}(\phi)$ will become singular when $\phi = \theta_i$ and condition 2) ensures that there will be no false alarm. If there is a transformation matrix $\mathbf{\Phi}$ as in Lemma 1, both conditions will be satisfied since we assume that the array manifolds of different DOAs are independent. Although the relation (74) will be slightly different for different shaped arrays, if the matrix $\mathbf{\Phi}(\phi)$ exists for the array, then the estimator is guaranteed to work. For arbitrary arrays, we need to redefine the array manifold vector. The m-th element of the array manifold vector of an arbitrary sensor array is

$$\exp\{j\omega(\vec{\alpha} \cdot \vec{r}_m)\}$$

where $\vec{x}_m$ is a position vector of the mth sensor and $\vec{\alpha}$ is the slowness vector such as

$$\vec{\alpha} = \frac{1}{c}(\sin\theta\sin\phi, \cos\theta\sin\phi, \cos\phi)$$

where θ and ϕ are the azimuth and the elevation, respectively [24]. The array manifold of the ULA in (20) is a special case of this general array manifold. Note that the magnitude of $\vec{\alpha}$ is the inverse of the propagation speed.

Let's define the transformation matrix $\mathbf{\Phi}$ as

$$\mathbf{\Phi}(\omega, \vec{\alpha}) = \text{diag}\{\mathbf{a}(\omega, \vec{\alpha})\}.$$

Let the $\mathbf{b}$ vector be the transformed array manifold:

$$\mathbf{b} = \mathbf{\Phi}(\omega_1, \vec{\alpha}_1)\mathbf{a}(\omega_2, \vec{\alpha}_2).$$

The phase of the m-th element of the vector $\mathbf{b}$ is

$$\omega_1(\vec{\alpha}_1 \cdot \vec{r}_m) + \omega_2(\vec{\alpha}_2 \cdot \vec{r}_m) = \omega_3(\vec{\beta} \cdot \vec{r}_m), \tag{83}$$

where $\omega_3 = \omega_1 + \omega_2$, and

$$\begin{aligned} \vec{\beta} &= \frac{\omega_1\vec{\alpha}_1 + \omega_2\vec{\alpha}_2}{\omega_3} \\ &= \zeta\vec{\alpha}_1 + (1-\zeta)\vec{\alpha}_2 \end{aligned} \tag{84}$$

where $\zeta = \omega_1/\omega_3$. If the magnitude of $\vec{\beta}$ is $1/c$, $\mathbf{b}$ is nothing but the array manifold vector of frequency ω_3 and the estimator will work. By the triangle inequality,

$$\left|\vec{\beta}\right| \leq \zeta|\vec{\alpha}_1| + (1-\zeta)|\vec{\alpha}_2| = \frac{1}{c}.$$

and the equality holds if and only if $\vec{\alpha}_1$ is proportional to $\vec{\alpha}_2$. Since $\vec{\alpha}_1$ and $\vec{\alpha}_2$ have same magnitude, equality happens if and only if $\vec{\alpha}_1 = \vec{\alpha}_2$. Usually, $\vec{\alpha}_1 \neq \vec{\alpha}_2$ and we cannot say that $\mathbf{b}$ is the array manifold in general. However, if there exists a slowness vector $\vec{\alpha}_3$ such that

$$\vec{\beta} \cdot \vec{r}_m = \vec{\alpha}_3 \cdot \vec{r}_m, \tag{85}$$

then $\mathbf{b}$ is a valid array manifold with the direction of $\vec{\alpha}_3$ regardless of the magnitude of $\vec{\beta}$. If the magnitude of $\vec{\beta}$ is less than $1/c$, for 1-D or 2-D arrays, we can still find α_3 satisfying (85). Let

$$\begin{aligned} \vec{\alpha}_l &= (\alpha_{l,x}, \alpha_{l,y}, \alpha_{l,z}), \\ \vec{\beta} &= (\beta_x, \beta_y, \beta_z). \end{aligned}$$

and define sensor position vectors as

$$\begin{aligned} \mathbf{x} &= [\ x_1 \quad \cdots \quad x_M]^T, \\ \mathbf{y} &= [\ y_1 \quad \cdots \quad y_M]^T, \\ \mathbf{z} &= [\ z_1 \quad \cdots \quad z_M]^T. \end{aligned}$$

If we define the vector of phases of the array manifold as

$$phase\{\mathbf{a}\} = \begin{bmatrix} \vec{\alpha} \cdot \vec{r}_1 \\ \vdots \\ \vec{\alpha} \cdot \vec{r}_M \end{bmatrix} = \vec{\alpha} \cdot \tilde{\mathbf{x}},$$

then we can rewrite (85) as

$$\begin{aligned}\vec{\beta}\cdot\tilde{\mathbf{x}} &= \beta_x\mathbf{x}+\beta_y\mathbf{y}+\beta_z\mathbf{z}\\ &= \alpha_{3,x}\mathbf{x}+\alpha_{3,y}\mathbf{y}+\alpha_{3,z}\mathbf{z}\\ &= \vec{\alpha_3}\cdot\tilde{\mathbf{x}}\end{aligned}$$

If the array's geometry cannot be collapsed into a lower dimensional array, the sensor position vectors $\mathbf{x}$, $\mathbf{y}$, and $\mathbf{z}$ are independent. In order to find $\vec{\alpha}_3$ where (85) holds, it is enough to compare $\vec{\beta}$ and $\vec{\alpha}_3$ element by element.

5.2.1 One-dimensional (Linear) Array

The sensor location vector $\vec{x}_m$ has only one dimension for linear arrays. Then, (85) is equivalent to one simple equation

$$\zeta\sin\theta_1+(1-\zeta)\sin\theta_2=\sin\theta_3. \tag{86}$$

There always exists an angle θ_3 that satisfies (86) for any $-1<\zeta<1$, θ_1, and θ_2. Therefore,

$$\begin{aligned}\mathbf{b} &= \mathbf{\Phi}(\omega_1,\theta_1)\mathbf{a}(\omega_2,\theta_2)\\ &= \mathbf{a}(\omega_3,\theta_3)\end{aligned}$$

This is same as Lemma 1.

5.2.2 Two-dimensional Array

For two-dimensional arrays ($\mathbf{z}=\mathbf{0}$), we need to compare two elements.

$$\begin{aligned}&(\zeta\vec{\alpha}_1+(1-\zeta)\vec{\alpha}_2)\cdot\vec{\mathbf{x}}\\ &=(\zeta\alpha_{1,x}+(1-\zeta)\alpha_{2,x})\mathbf{x}+(\zeta\alpha_{1,y}+(1-\zeta)\alpha_{2,y})\mathbf{y}.\end{aligned}$$

If we change the variables

$$\begin{aligned}u_l &= \sin\theta_l,\\ v_l &= \sin\phi_l.\end{aligned}$$

then,

$$\begin{aligned} \alpha_{l,x} &= v_l u_l, \\ \alpha_{l,y} &= v_l \sqrt{1-u_l^2}. \end{aligned}$$

Finally, (85) is equivalent to

$$\begin{aligned} \zeta v_1 u_1 + (1-\zeta) v_2 u_2 &= v_3 u_3, \\ \zeta v_1 \sqrt{1-u_1^2} + (1-\zeta) v_2 \sqrt{1-u_2^2} &= v_3 \sqrt{1-u_3^2}. \end{aligned}$$

It can be shown that there always exist vectors u_3 and v_3 given any numbers that satisfy $0 \leq |u_1|, |v_1|, |u_2|, |v_2| \leq 1$ and $-1 \leq \zeta \leq 1$. Therefore, $\mathbf{b}$ is an array manifold and we can conclude that the TOPS method works with arbitrary 1-D or 2-D arrays unless the array manifolds are dependent which is a case where any signal subspace method also fails.

5.3 Signal Subspace Projection

In practice, the correlation matrices are unavailable, so estimated correlation matrices have to be used in the place of real correlations. In order to estimate the correlation matrix, the sensor outputs should be divided into J identical blocks with the number of samples in one block equal to the number of DFT points. Let $\mathbf{x}_{j,i}$ be the sensor output at $\omega = \omega_i$ for the j-th block. Then, the estimated correlation matrix is

$$\hat{\mathbf{R}}_i = \frac{1}{J} \sum_{j=0}^{J-1} \mathbf{x}_{j,i} \mathbf{x}_{j,i}^H$$

From $\hat{\mathbf{R}}_i$, we can find $\hat{\mathbf{F}}_i$, $\hat{\mathbf{W}}_i$ using an eigenvalue decomposition. The DOA estimation performance depends on how precise the estimated correlation matrix is. The quality of the estimated correlation matrix is fully determined by the number of snapshots and the SNR, which are usually uncontrollable by the processor. By subspace projection,

however, it is possible to reduce some error terms in the matrix $\hat{\mathbf{D}}(\phi)$. Define a projection matrix $\mathbf{P}_i(\phi)$ as

$$\mathbf{P}_i(\phi) = \mathbf{I} - (\mathbf{a}_i^H(\phi)\mathbf{a}_i(\phi))^{-1}\mathbf{a}_i(\phi)\mathbf{a}_i^H(\phi), \tag{87}$$

which is the projection on to the null space of $\mathbf{a}_i(\phi)$. Then, a new $\mathbf{D}(\phi)$ matrix where $\mathbf{U}_i(\phi)$ is replaced by

$$\mathbf{U}_i'(\phi) = \mathbf{P}_i(\phi)\mathbf{U}_i(\phi) \tag{88}$$

provides an estimate with less mean square error. Let $\hat{\mathbf{F}}_i$ and $\hat{\mathbf{W}}_i$ be the estimated signal subspace matrix and noise subspace matrix, respectively. We can represent these estimated matrices and the estimation error matrices as

$$\begin{aligned} \hat{\mathbf{F}}_i &= \bar{\mathbf{F}}_i + \delta\mathbf{F}_i \\ \hat{\mathbf{W}}_i &= \bar{\mathbf{W}}_i + \delta\mathbf{W}_i \end{aligned}$$

where $\bar{\mathbf{F}}_i$ and $\bar{\mathbf{W}}_i$ are in the range of $\mathbf{F}_i$ and the range of $\mathbf{W}_i$, respectively. The terms $\delta\mathbf{F}_i$ and $\delta\mathbf{W}_i$ are error matrices such that

$$\begin{aligned} \delta\mathbf{F}_i &\subset \mathcal{N}\{\mathbf{F}_i\} \\ \delta\mathbf{W}_i &\subset \mathcal{R}\{\mathbf{F}_i\} \end{aligned}$$

and if the number of samples is large, it can be assumed that $\|\delta\mathbf{F}\|_F \ll \|\mathbf{F}\|_F$ and $\|\delta\mathbf{W}\|_F \ll \|\mathbf{W}\|_F$ where $\|\cdot\|_F$ denotes Frobenius norm.

If $\theta = \theta_p$,

$$\begin{aligned} \hat{\mathbf{F}}_i^H\hat{\mathbf{W}}_i &= (\bar{\mathbf{F}}_i^H + \delta\mathbf{F}_i^H)(\bar{\mathbf{W}}_i + \delta\mathbf{W}_i) \\ &= \bar{\mathbf{F}}_i^H\bar{\mathbf{W}}_i + \delta\mathbf{F}_i^H\bar{\mathbf{W}}_i + \bar{\mathbf{F}}_i^H\delta\mathbf{W}_i + \delta\mathbf{F}_i^H\delta\mathbf{W}_i \\ &\simeq \bar{\mathbf{T}}_i^H \begin{bmatrix} * \\ \mathbf{0}^T \\ * \end{bmatrix} + \delta\mathbf{F}_i^H\bar{\mathbf{W}}_i + \bar{\mathbf{F}}_i^H\delta\mathbf{W}_i \end{aligned}$$

In the last equation, the second order term is neglected. It is important to note that the terms other than the first term prevent $\hat{\mathbf{F}}_i^H \hat{\mathbf{W}}_i^H$ from losing rank. If the projection matrix is included

$$\begin{aligned}
\hat{\mathbf{F}}_i^H \mathbf{P}_i^H \hat{\mathbf{W}}_i &= (\bar{\mathbf{F}}_i^H + \delta\mathbf{F}_i^H)\mathbf{P}_i^H(\bar{\mathbf{W}}_i + \delta\mathbf{W}_i) \\
&= (\tilde{\mathbf{F}}_i^H + \delta\mathbf{F}_i^H)(\bar{\mathbf{W}}_i + \delta\mathbf{W}_i) \\
&= \tilde{\mathbf{F}}_i^H \bar{\mathbf{W}}_i + \delta\mathbf{F}_i^H \bar{\mathbf{W}}_i + \tilde{\mathbf{F}}_i^H \delta\mathbf{W}_i + \delta\mathbf{F}_i^H \delta\mathbf{W}_i \\
&\simeq \bar{\mathbf{T}}_i^H \begin{bmatrix} * \\ \mathbf{0}^T \\ * \end{bmatrix} + \delta\mathbf{F}_k^H \bar{\mathbf{W}}_k + \tilde{\mathbf{F}}_k^H \delta\mathbf{W}_i \qquad (89)
\end{aligned}$$

Using the fact that $\mathbf{P}_i \delta\mathbf{F}_i = \delta\mathbf{F}_i$ and

$$\tilde{\mathbf{F}}_i = \begin{bmatrix} * & \mathbf{0} & * \end{bmatrix} \bar{\mathbf{T}}_i.$$

(89) becomes

$$\begin{aligned}
\hat{\mathbf{F}}_i^H \mathbf{P}_i^H \hat{\mathbf{W}}_i &\simeq \bar{\mathbf{T}}_i^H \begin{bmatrix} * \\ \mathbf{0}^T \\ * \end{bmatrix} + \delta\mathbf{F}_i^H \bar{\mathbf{W}}_i + \bar{\mathbf{T}}_i^H \begin{bmatrix} \diamond \\ \mathbf{0}^T \\ \diamond \end{bmatrix} \\
&\simeq \bar{\mathbf{T}}_i^H \begin{bmatrix} * + \diamond \\ \mathbf{0}^T \\ * + \diamond \end{bmatrix} + \delta\mathbf{F}_i^H \bar{\mathbf{W}}_i \qquad (90)
\end{aligned}$$

Thus one error term has been removed and this reduces the perturbation on the smallest singular value.

Note that this projection method can be used only when the distance between sensors is less than half the wavelength of the highest frequency that is used in processing, not the center frequency; otherwise, aliasing happens. If the FOV is known and is less than half the whole angle space [$-\pi \sim \pi$), we can just ignore aliasing that appears in the other half.

5.4 Algorithm

Since all the signal subspace and noise subspace are estimated, $\mathbf{D}$ would never become singular. However, we can determine how close a matrix is to a singular matrix by looking at the condition number, or the minimum singular value, of the matrix [19]. In this case, the smallest singular value is a better indicator since we are looking for the case where $\mathbf{D}$ becomes singular when one of the row vectors of (80) is a zero vector.

The following steps summarize the process of finding the DOAs of wideband sources using the DFT. If a filter bank is used, the correlation matrix will be estimated as shown in Section 3.1.

1. Divide the sensor outputs into J identical sized blocks.

2. Compute the temporal DFT of the J blocks.

3. For the j-th block, select $\mathbf{x}_{j,i}$ of pre-selected frequencies ω_i where $i = 1, \ldots, K$ and $j = 1, \ldots, J$.

4. Compute the signal subspace $\hat{\mathbf{F}}_1$ and the noise subspace $\hat{\mathbf{W}}_i$ for $i = 2, \ldots, K$ by EVD of the estimated covariance matrices $\hat{\mathbf{R}}_i$

5. Generate $\hat{\mathbf{U}}'_{\mathbf{i}}$ using (88) for each hypothesized ϕ .

6. Estimate $\hat{\boldsymbol{\theta}}$ by

$$\hat{\boldsymbol{\theta}} = \arg\max_{\boldsymbol{\phi}} \left\{ \frac{1}{\sigma_{min}(\boldsymbol{\phi})} \right\} = \arg\min_{\boldsymbol{\phi}} \sigma_{min}(\boldsymbol{\phi})$$

   where $\sigma_{min}(\boldsymbol{\phi})$ is the smallest singular value of $\mathbf{D}(\boldsymbol{\phi})$, and $\boldsymbol{\phi} = \phi$ for 1-D arrays or $\boldsymbol{\phi} = [\theta, \phi]$ for 2-D arrays.

The estimation problem now involves finding P local maxima (minima) by doing a one/two dimensional search over the domain of possible angles. This strategy is similar to MUSIC [41].

5.5 Computational Complexity

It is not easy to calculate the exact computational cost of the TOPS estimator. The number of computations for the EVD of an $M \times M$ matrix is $O(M^3)$ [19]. The minimum nonzero singular values of the $\mathbf{D}$ matrix can be found by doing an EVD of a $P \times P$ matrix. Since this requires $O(P^3)$ computations for each hypothesized ϕ, the computational cost is high for TOPS. For CSSM or WAVES, once the general correlation matrix is estimated, only one EVD is required to use those narrowband signal subspace methods. Therefore, they take fewer computations than TOPS. However, to find the RSS focusing matrices, they require an EVD of an $M \times M$ $(M > 2P)$ matrix for each of the frequency bins, and if we consider the computational cost for preprocessing and the performance results that are shown in the following section, TOPS is still a viable alternative choice for wideband DOA estimations despite its high computational cost.

CHAPTER 6

ANALYSIS

In this chapter, the factors that might effect the performance of TOPS are considered. These include the effect of incorrect estimates of the number of signals and a strategy for choosing the frequency bins.

6.1 Effect of The Number of Signals P

The number of signals P is usually estimated from an EVD of the correlation matrix. While MUSIC uses only the noise subspace and finds vectors orthogonal to it, TOPS uses the singularity of the $\mathbf{D}$ matrix which contains both the signal and the noise subspace. Therefore, having the wrong number of signals leads not only to incorrect signal and noise subspaces but also may lead to a disaster in the target estimator. Since the estimated number $\hat{P}$ is not always right, it is necessary to consider the effect of this error.

6.1.1 Over-estimated P

Let's say P is the true number of signals and $\hat{P}$ is the estimated number. If $\hat{P} > P$ (over-estimated), the estimated signal subspace $\hat{\mathbf{F}}_1$ is

$$\hat{\mathbf{F}}_1 = \begin{bmatrix} \mathbf{F}_1 & \tilde{\mathbf{W}}_1 \end{bmatrix}$$

where $\mathbf{F}_0$ is the true signal subspace and

$$\tilde{\mathbf{W}}_1 = \begin{bmatrix} \mathbf{v}_{1,P+1} & \cdots & \mathbf{v}_{1,\hat{P}} \end{bmatrix}$$

is the set of additional eigenvectors from the noise subspace caused by over-estimating $\hat{P}$. Then, the $\mathbf{D}$ matrix becomes

$$\begin{aligned}
\mathbf{D}_{\hat{P}}(\phi) &= \begin{bmatrix} \mathbf{F}_1^H \\ \tilde{\mathbf{W}}_1^H \end{bmatrix} \begin{bmatrix} \mathbf{\Phi}_2^H(\phi)\mathbf{W}'_2 & \cdots & \mathbf{\Phi}_K^H(\phi)\mathbf{W}'_K \end{bmatrix} \\
&= \begin{bmatrix} \mathbf{D}'_P(\phi) \\ \tilde{\mathbf{W}}_2^H \begin{bmatrix} \mathbf{\Phi}_2^H(\phi)\mathbf{W}'_2 & \cdots & \mathbf{\Phi}_K^H(\phi)\mathbf{W'}_K \end{bmatrix} \end{bmatrix} \\
&= \begin{bmatrix} \mathbf{D}'_P(\phi) \\ \mathbf{E}(\phi) \end{bmatrix}
\end{aligned} \tag{91}$$

where

$$\mathbf{W}'_i = \begin{bmatrix} \mathbf{v}_{i,\hat{P}+1} & \cdots & \mathbf{v}_{i,M} \end{bmatrix}.$$

In other words, $\mathbf{W}'_i$ is the set of $M - \hat{P}$ smallest eigenvectors instead of the signal subspace $\mathbf{W}_i$ that is the set of the $M - P$ smallest eigenvectors. In order for the estimator to work, $\mathbf{D}_{\hat{P}}(\phi)$ matrix should lose its rank if and only if $\phi = \theta_l$ for some l.

It is straightforward to show that $\mathbf{D}_{\hat{P}}(\phi)$ becomes singular when $\phi = \theta_l$ for some l since $\mathbf{D'}_P(\phi)$ becomes singular. Therefore, the smallest singular value of (91) will be zero when $\phi = \theta_l$. However, for the estimator to work, $\mathbf{D}_{\hat{P}}(\phi)$ should NOT lose its rank when $\phi \neq \theta_l$ for all $l = 0, \ldots, P-1$. There are two cases where it becomes rank-deficient even if $\phi \neq \theta_l$: 1) $\mathbf{D}'_P(\phi)$ and $\mathbf{E}(\phi)$ are nonsingular but the row vectors of $\mathbf{E}(\phi)$ and $\mathbf{D}'_P(\phi)$ are linearly dependent and 2) $\mathbf{D}'_P(\phi)$ or $\mathbf{E}(\phi)$ is singular.

Theorem 2 $\mathbf{D}_{\hat{P}}(\phi)$ *is full rank when both* $\mathbf{D}'_P(\phi)$ *and* $\mathbf{E}(\phi)$ *are nonsingular.*

Proof: Assume that $\mathbf{D}_{\hat{P}}(\phi)$ is singular ($\gamma\{\mathbf{D}_{\hat{P}}(\phi)\} \leq \hat{P}$). Then there exist vectors $\mathbf{y}_1$ and $\mathbf{y}_2$ such that

$$\begin{bmatrix} \mathbf{y}_1^H & \mathbf{y}_2^H \end{bmatrix} \begin{bmatrix} \mathbf{D}'_P(\phi) \\ \mathbf{E}(\phi) \end{bmatrix} = \mathbf{0}^T,$$

which is equivalent to

$$\mathbf{y}_1^H \mathbf{F}_1^H \mathbf{H} + \mathbf{y}_2^H \tilde{\mathbf{W}}_1^H \mathbf{H} = \mathbf{0}^T$$

and it can be simplified as

$$(\mathbf{y}_1^H \mathbf{F}_1^H + \mathbf{y}_2^H \tilde{\mathbf{W}}_1^H)\mathbf{H} = 0^T \tag{92}$$

where

$$\mathbf{H} = \left[\begin{array}{ccc} \mathbf{\Phi}_2^H(\phi)\mathbf{W}'_2 & \cdots & \mathbf{\Phi}_K^H(\phi)\mathbf{W}'_K \end{array} \right].$$

Since we have assumed that $\mathbf{D}'_P(\phi)$ and $\mathbf{E}(\phi)$ are full rank matrices and that $\mathbf{F}_1$ and $\tilde{\mathbf{W}}_1$ contain a set of orthonormal eigenvectors, the only solution to (92) is

$$\mathbf{y}_1 = \mathbf{0}_P$$
$$\mathbf{y}_2 = \mathbf{0}_{\hat{P}-P}$$

where $\mathbf{0}_P$ is a P-dimensional zero vector. Therefore, if $\mathbf{D}'_P(\phi)$ and $\mathbf{E}(\phi)$ are nonsingular, $\mathbf{D}_{\hat{P}}(\phi)$ is nonsingular. ■

The above Theorem excludes the first case where the estimator fails.

Lemma 3 *The estimator fails if and only if*

$$\bigcap_{i=2}^{K} \left\{ \mathcal{R}\left\{\hat{\mathbf{A}}_i\right\} \cap \mathcal{R}\left\{ \left[\begin{array}{cc} \mathbf{A}_i & \tilde{\mathbf{W}}_i \end{array} \right] \right\} \right\} \neq \emptyset \tag{93}$$

or

$$\bigcap_{i=2}^{K} \left\{ \mathcal{R}\left\{\mathbf{\Phi}_i(\phi)\tilde{\mathbf{W}}_1\right\} \cap \mathcal{R}\left\{ \left[\begin{array}{cc} \mathbf{A}_i & \tilde{\mathbf{W}}_i \end{array} \right] \right\} \right\} \neq \emptyset \tag{94}$$

Proof: By Theorem 2, it is proved that the estimator fails if and only if $\mathbf{D}'_P(\phi)$ or $\mathbf{E}(\phi)$ is singular. It means that there exists a vector $\mathbf{b}$ or $\mathbf{c}$ such that

$$\mathbf{b}^H \mathbf{D}'_P(\phi) = \mathbf{0}^T \tag{95}$$

where $\mathbf{b} \in \mathbb{C}^P$, or

$$\mathbf{c}^H \mathbf{E}(\phi) = \mathbf{0}^T \tag{96}$$

where $\mathbf{c} \in \mathbb{C}^{(\hat{P}-P)}$. Equation (95) is equivalent to

$$\bigcap_{i=2}^{K} \mathcal{LN}\left\{\mathbf{F}_1^H \mathbf{\Phi}_i^H(\phi)\mathbf{W}_i'\right\} \neq \emptyset \tag{97}$$

Note that $\mathbf{\Phi}_i(\phi)\mathbf{F}_0 = \hat{\mathbf{A}}_j$. Since the column vectors of $\mathbf{\Phi}_i(\phi)\mathbf{F}_0$ are linearly independent, the left null space for $\hat{\mathbf{A}}_i^H \mathbf{W}_i'$ is

$$\mathcal{R}\{\hat{\mathbf{A}}_i\} \cap \mathcal{LN}\{\mathbf{W}_i'\} \tag{98}$$

The left null space of $\mathbf{W}_i'$ is

$$\mathcal{LN}\{\mathbf{W}_i'\} = \mathcal{R}\left\{\begin{bmatrix} \mathbf{A}_i & \tilde{\mathbf{W}}_i \end{bmatrix}\right\}$$

Therefore, (97) is equivalent to (93). By the same reasoning, it can be shown that (94) is the case where the $\mathbf{E}(\phi)$ matrix is singular. ■

Equation (93) is identical to the case where the signal subspace methods fail with an over-estimate of the number of signals. It is the case where not only TOPS but also all the signal subspace methods fail to work. Equation (94) is the case where only TOPS fails. The rank of the range space of $\mathbf{\Phi}_i(\phi)\tilde{\mathbf{W}}_1$ is as small as $\hat{P} - P$, and that of $[\mathbf{A}_i \ \tilde{\mathbf{W}}_i]$ is $\hat{P}$. Equation (94) requires that there be a non-zero intersection between all $(K-1)$ rank-$(\hat{P}-P)$ subspaces and the $(K-1)$ rank-$\hat{P}$ subspaces in the M-dimensional vector spaces. Since $M > 2\hat{P}$ (we assumed that the number of signals is less than (M/2), as K or M increases, the probability that (94) is true decreases. This is also true for (93) even when the rank of $\hat{\mathbf{A}}_i$ is larger than that of $\mathbf{\Phi}_i(\phi)\tilde{\mathbf{W}}_1$. In fact, we cannot guarantee that there is no false alarm, because the $\mathbf{D}_{\hat{P}}(\phi)$ matrix can lose its rank even if ϕ does not match any of the DOAs. However, it is still possible to estimate DOAs since $\mathbf{D}_{\hat{P}}(\phi)$ becomes singular when $\phi = \theta$ and the false alarm is unlikely to occur when the number of frequency bins is large or the number of signals is small. The performance of the estimator with an over-estimated value of P will be shown in the Chapter 7.

6.1.2 Under-estimated P

The other case is when the estimated $\hat{P}$ is less than the correct value of P. In this case, the estimated noise subspaces contain part of the signal subspaces. The $\mathbf{D}$ matrix would not lose rank even if the hypothesized ϕ matches one of the DOAs due to those signal subspace components. One way to avoid this case is to set the threshold low when estimating P so that the estimator tends to over-estimate P.

6.2 Choosing Subspaces

TOPS uses a subset of the all frequency bins. Among the chosen K frequencies, one frequency bin is used for the signal subspace $\mathbf{F}_1$ and the rest are used for the noise subspaces ω_i. Depending on which frequency bins are chosen, the estimator performance could be different. There are various possible strategies for choosing frequency bins. First, we may choose the signal subspace of the frequency bin where the separation between the smallest eigenvalue in the signal subspace and the largest eigenvalue in the noise subspace is maximum. The signal subspace $\mathbf{F}_1$ is very important in TOPS since only one signal subspace is used but multiple noise subspaces. The other possible approach is to weight the subspaces. Subspace weighting appears in weighted subspace fitting (WSF) method [57]. In the WSF, the optimal weighting matrix is chosen to minimize error covariances. In TOPS, the same type of weighting is not valid since it is not a least-square type method. However, we can borrow the idea since it weights eigenvectors proportional to the difference between its corresponding eigenvalues and the eigenvalues of the noise subspace.

The number of frequency bins is also an important parameter to choose in TOPS. Since more frequency bins require more computations, the number of frequency bins K should be determined as a trade-off between performance and computational cost. More studies are necessary to find a way to determine the optimal number and the optimal set of frequency bins

6.3 Asymptotic Performance

The estimated correlation matrix is always different from the true correlation matrix because the estimate relies on a finite number of samples. Therefore, eigenvectors derived from the estimated correlation matrix are also different from the true eigenvectors. Even though the asymptotic behavior of the eigenvectors is well known, the statistics of the singular values are not well known, so it is not easy to characterize the statistics of the TOPS estimator. For the single source case, the matrix $\mathbf{D}(\phi)$ is a vector. Therefore, the Euclidian norm is used instead of the smallest singular value. Then,

$$\begin{aligned} \|\mathbf{D}(\phi)\|_2^2 &= \mathbf{D}(\phi)\mathbf{D}^H(\phi) \\ &= \frac{1}{|\mathbf{a}_1(\theta)|^2}\sum_{i=2}^{K}\mathbf{a}_1^H(\theta)\mathbf{\Phi}_i^H(\phi)\mathbf{W}_i\mathbf{W}_i^H\mathbf{\Phi}_i(\phi)\mathbf{a}_1(\theta) \\ &= \frac{1}{|\mathbf{a}_1(\theta)|^2}\sum_{i=2}^{K}\mathbf{a}_i^H(\theta')\mathbf{W}_i\mathbf{W}_i^H\mathbf{a}_i(\theta') \end{aligned} \tag{99}$$

The above equation holds only if the eigenvector of the correlation matrix is the same as the normalized array manifold. This happens only if the bandwidth of the passband in the filter bank is zero. However, if the fractional bandwidth is small, it can be approximated by (99). Since the inverse of (99) indicates the source locations, it is similar to IMUSIC (32). Assume that the observation time is long enough so that $\mathbf{X}(\omega_i)$ and $\mathbf{X}(\omega_j)$ are independent when $\omega_i \neq \omega_j$. Then, the variance of the estimation error is [46]

$$E[(\theta-\theta')^2] = \frac{1}{2J}\frac{\sum_{i=1}^{K}\mathbf{a}_i^H(\theta)\mathbf{C}_i\mathbf{a}_i(\theta)}{\sum_{i=1}^{K}h_i(\theta)} \tag{100}$$

where

$$\mathbf{C}_i = \sum_{\substack{j=1 \\ j\neq i}}^{P}\frac{\sigma^2\lambda_{i,j}}{(\sigma^2-\lambda_{i,j})^2}\mathbf{v}_{i,j}\mathbf{v}_{i,j}^H$$

and

$$h_i(\theta) = \mathbf{d}_i^H(\theta)\mathbf{W}_i\mathbf{W}_i^H\mathbf{d}_i(\theta).$$

where $\mathbf{v}_{i,j}$ and $\lambda_{i,j}$ are the j-th largest eigenvector of the correlation matrix at frequency ω_i and the corresponding eigenvalue and $\mathbf{d}_i(\theta) = d\mathbf{a}_i(\theta)/d\theta$. The error variance of CSSM for the single source case is the same as (100) except that the noise covariance σ^2 is reduced to σ^2/K assuming that the focusing angle exactly matches the DOA. This implies that CSSM can perform better than TOPS when there is single target. However, this is only true for the case when the initial focusing angle for CSSM matches the DOA exactly.

CHAPTER 7

SIMULATIONS

The performance of TOPS is tested by computer simulations and compared with two coherent methods (CSSM and WAVES) and one incoherent method (IMUSIC) using various scenarios. The simulation results in this chapter exhibit the characteristics of each method.

7.1 Specifications

A ten-sensor uniform linear array is the main array structure used in these simulations, except for the case where circular array is used for testing the 2-D case. The distance between sensors is half of the shortest wavelength of the wideband signals. This ensures that there is no spatial aliasing. Note that CSSM and WAVES work without aliasing even for a larger sensor displacement, equal to $\lambda/2$ at the center frequency [12, 58]. Two kinds of wideband signals are used. The first one is the sum of sinusoidal signals such as

$$s_i(t) = b_i(t) \sum_{n=1}^{N_f} e^{j(2\pi f_n t + \sigma_n)} \tag{101}$$

where $b_i(t)$ is a complex circular Gaussian random variable and σ_n is a uniformly distributed random phase in $[0, 2\pi]$. The signal $s_i(t)$ is the sum of exponentials of N_f different frequencies with random phases. The magnitude $b_i(t)$ is assumed to vary slowly in time so that the estimated correlation matrix of the frequency-dependent signal decomposed by DFT is valid. Another signal model is the sinc function with Gaussian random magnitude. For both models, the fractional bandwidth was set equal to 2/3 and the sampling frequency is three times higher than the highest frequency of the signals. The number of signals P is three, two of which are fixed at

Table 1: The specification of simulations

Number of sensors M	10
Number of sources P	3
DOAs	$8°$, $33°$ and $(35, 36, 37,$ or $38°)$
Signal's frequency band	$\pi/3 \sim 2\pi/3$
Number of frequency bins K	3,5,7, and 9 (TOPS, IMUSIC). 21 (CSSM, WAVES)

$8°$ and $33°$. The location of the third signal is changed for each simulation to test the resolution of the estimators. The number of frequency bins used for TOPS is also changed for each simulation to see its effect on the estimation performance. The frequency bin used for the signal subspace is chosen so that the difference between the smallest eigenvalue of the signal subspace and the largest eigenvalue of the noise subspace is maximum for that frequency bin. There are three scenarios: The first scenario is the case when the number of signals is known. The second scenario is the case of over-estimating the number of signals. The third scenario is the case where the number of frequency bins is different. For each scenario, there are four cases depending on the third signal's location. The location is $35°$, $36°$, $37°$, and $38°$ making the smallest angle differences vary from $2°$ to $5°$.

7.2 Focusing

For CSSM and WAVES, the focusing angles are one of the most important factors that determine the estimator's performance. Even though it does not require focusing angles when it is combined with the beamforming invariant (BI) focusing matrices in (38) [32], the performance of WAVES is better when it uses RSS rather than BI focusing matrices [12]. In the simulation discussed here, two different kinds of focusing angles are used. First, we used Gaussian random variables

$$\boldsymbol{\theta}_F \sim \mathcal{N}(\boldsymbol{\theta}, \sigma_F^2 \mathbf{I}) \tag{102}$$

as focusing angles. The mean of the focusing angle is same as true DOA and the focusing errors are independent of each other. It should be mentioned here that the errors in focusing angles are usually coupled, so independent errors between focusing angles might be a little bit unrealistic. However, simulations with those focusing angles can give some idea of how much error in the focusing angles can be tolerated. Various values of σ_F^2 are used in simulations. A second method of generating the focusing angles is the realistic focusing strategy in [21]. That is, 1) find DOAs μ_i using low-resolution algorithms 2) use $\mu_i + 0.25\text{BW}$, and $\mu_i - 0.25\text{BW}$ as well as μ_i as focusing angles where BW denotes the beamwidth to cover signals that might not be detected by low-resolution techniques. Unlike the focusing angles which are fixed in [21], the μ_i's are estimated at each run in this thesis. This should be more realistic since the μ_i's are also random variables. Capon's method is used as preprocessing to find the focusing angles [10]. In order to use Capon's method which is a narrowband technique, the sensor outputs are first decomposed into narrowband signals and the frequency bin with the maximum power is used for beamforming. In high SNR cases, Capon's method successfully detects all three signals. In those cases, the μ_i's are used as the focussing angles. For all other cases, the $\pm 0.25\text{BW}$ strategy mentioned above is used. As a focusing matrix, the RSS focusing matrix (37) is used [21, 13]

7.3 Results

The performance of the estimator is summarized with the sum of the root mean square (RMS) error of all three sources and with the probability of resolution. The probability of resolution denotes the probability that the two closest sources are resolved. The minimum DOA difference between the two closest sources is varied from 2° up to 5°. The performance statistics are calculated from the results of 200 Monte-Carlo runs. However, since the probability of resolution is different for each method, the number of results used for the RMS error computation is different. Figure 18 shows

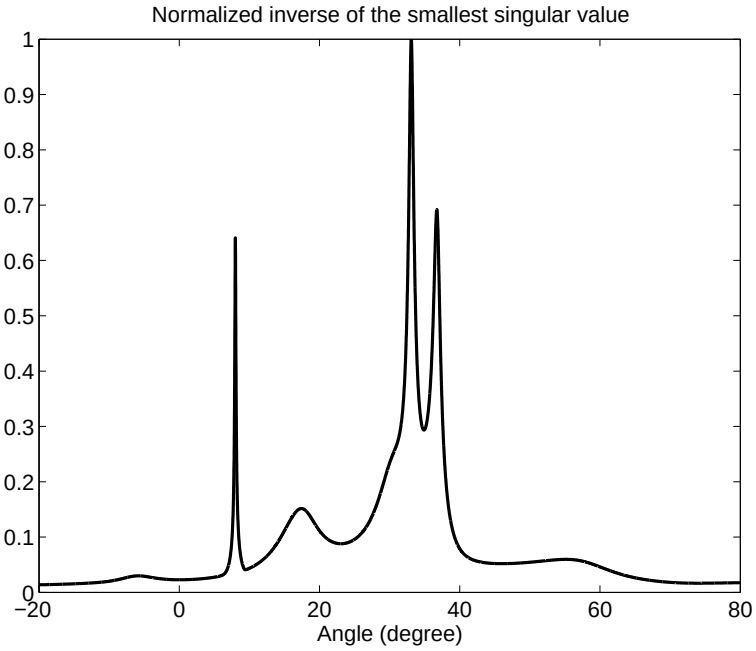

Figure 18: One example run of TOPS (SNR=10dB)

one example result of TOPS where the plot is the normalized inverse of the smallest singular value of the **D** matrix. In this run, the signals are located at $[8°,\ 33°, 37°]$ and the three peaks in the figure indicate those three signals at the correct locations. Since the plot is the inverse of singular values, the magnitude of the peaks does not correspond to the power of the signals. Figure 19 shows results for a seven-sensor 2-D circular array. For comparison, same case done with IMUSIC is also shown in Figure 20. We can easily see that there are two targets at $(10°, 20°)$ and $(20°, 15°)$. This example shows that TOPS works correctly with 2-D arrays. Note that the width of the peaks in TOPS is narrower than those in IMUSIC. Furthermore, TOPS exhibits a lower sidelobe level than IMUSIC. These two factors are very important in resolving two closely spaced targets.

7.3.1 Case 1: Known number of signals

When the number of signals, P, is known or estimated correctly, the signal and the noise subspaces have the proper dimensions. In Figs. 21 to 24, the RMS errors

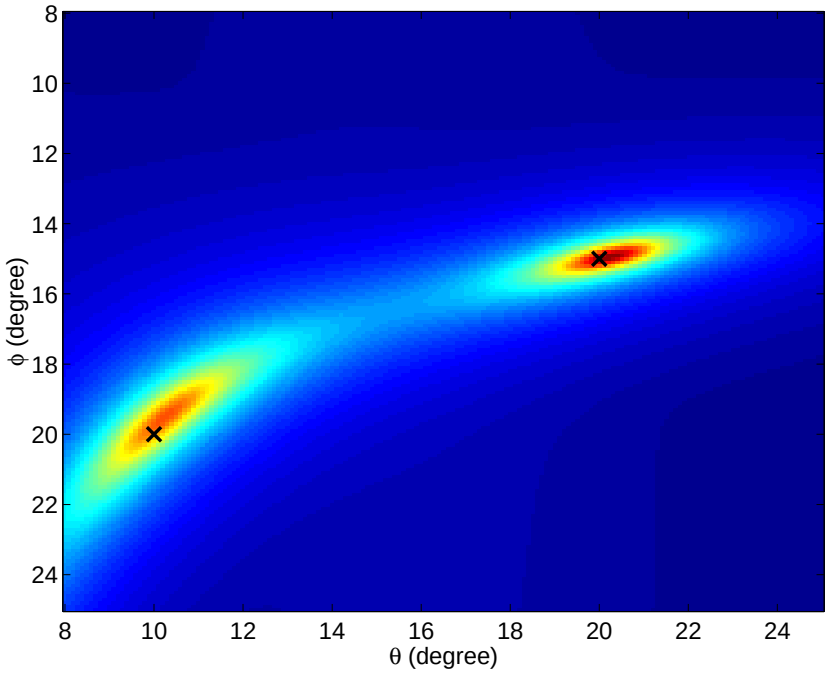

Figure 19: One example run of TOPS with a 2-D seven-sensor circular array.

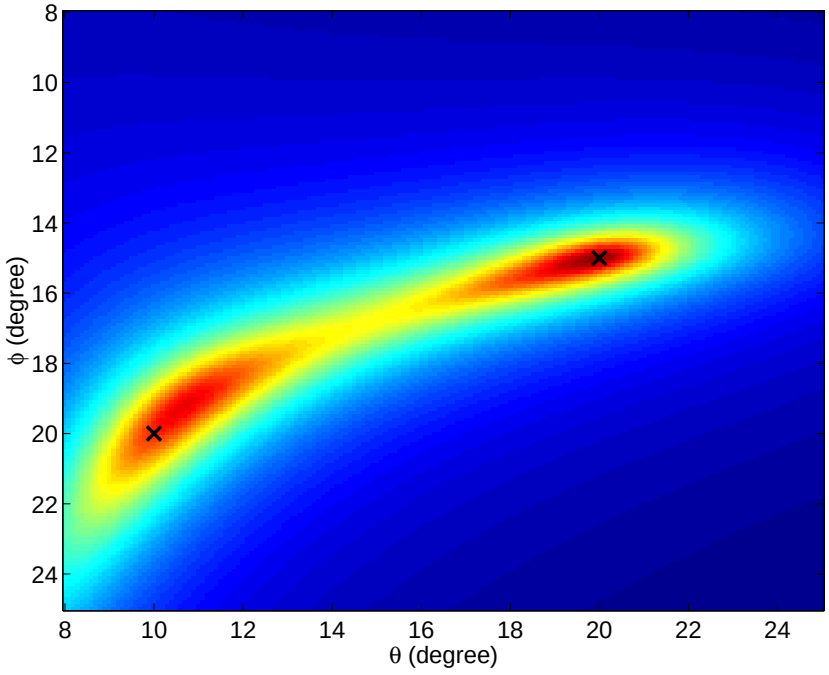

Figure 20: One example run of IMUSIC with a 2-D seven-sensor circular array.

for different locations of the third source when the source signal is (101) are shown followed by Figs. 25 through 28 showing the probability of resolution. Focusing angles for CSSM and WAVES are determined by the strategy in [21]. Simulation results with the same specification except that the source signal is a sinc function can be found in Appendix A. When the minimum DOA difference is less than 3 degrees, it is hard to compare the performance characteristics of the four methods since the probability of resolution of IMUSIC and TOPS is close to zero when the SNR drops below 10 dB. When the minimum DOA difference is larger than 3 degrees, we can compare the overall performance of the estimators (see Figs. 23 and 24.) When the third signal is at 37° (Fig. 23), the two coherent methods (CSSM and WAVES) show similar performance for all SNRs. At high SNR, IMUSIC and TOPS show similar performance both in RMS error and probability of resolution. These two incoherent methods outperform both coherent methods when the SNR is higher than 5 dB. However, when the SNR is less than 5 dB, the RMS error of the incoherent methods suddenly increases and the probability of resolution drops dramatically. Below 0 dB, the coherent methods show better performance than the two incoherent methods. In the mid-SNR range (from 0 dB to 10 dB), TOPS shows a little bit better performance than IMUSIC. In other words, the incoherent methods work better than the coherent methods in high SNR, but, in low SNR, the coherent methods are better. In between, TOPS outperforms all three other methods.

Figures 29 through 32 compare the results of TOPS with CSSM for randomized focusing angles as in equation (102) when the third signal is at 36° (Figs. 29 and 30) and 37° (Figs. 31 and 32). Two other cases where the third signal is at 35° and 38° are omitted since the results are similar to the figures presented here. The source signal is a sinc function for these simulations. The results show that even when the error in each focusing angle is as small as 0.1°, the RMS errors of TOPS is less than that of CSSM. When the SNR is less than 2 dB, the probability of resolution of

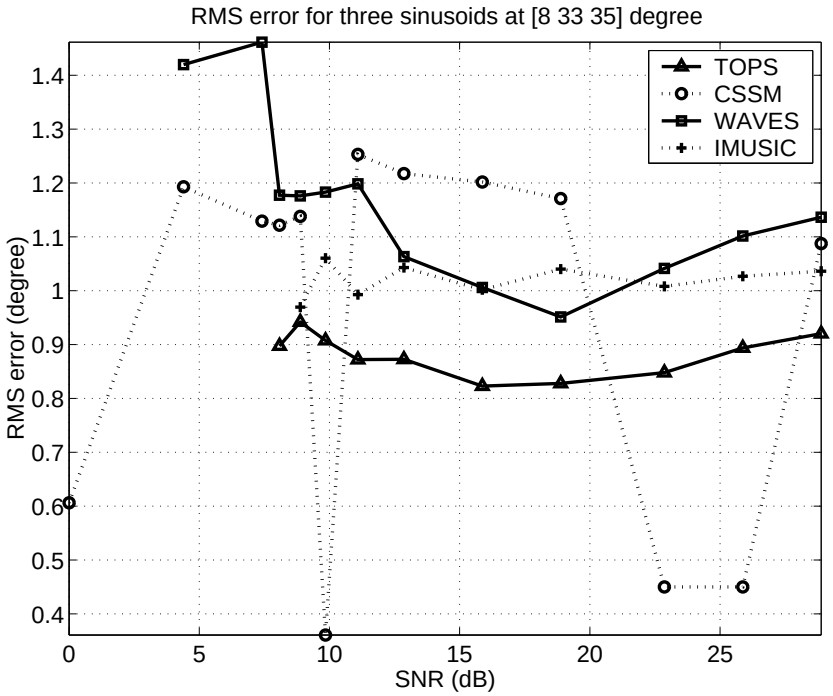

Figure 21: RMS error versus SNR of TOPS, CSSM, WAVES, and IMUSIC for third sinusoid at 35°.

TOPS is lower than CSSM with 2° focusing error. If the SNR is higher than 10 dB, TOPS outperforms CSSM with a focusing error as small as 0.1°. Note that when the focusing error is larger than 0.5°, the RMS error of CSSM does not decrease as SNR increases. It seems that the performance of CSSM is dominated by the errors in focusing angles.

7.3.2 Case 2: Over-estimated number of signals

In Section 6.1, it was shown that the probability that TOPS with an over-estimated value for P will fail is low. This time, the simulations were done with the same specification as the previous ones except that the number of signals is over-estimated by one. In other words, the dimension of the signal subspace is four instead of three while the dimension of the noise subspace is six instead of seven. This time only sinusoids signals are used for simulations. Figures 33 through 35 show the RMS errors and Figs. 36 through 38 show the corresponding probability of resolution.

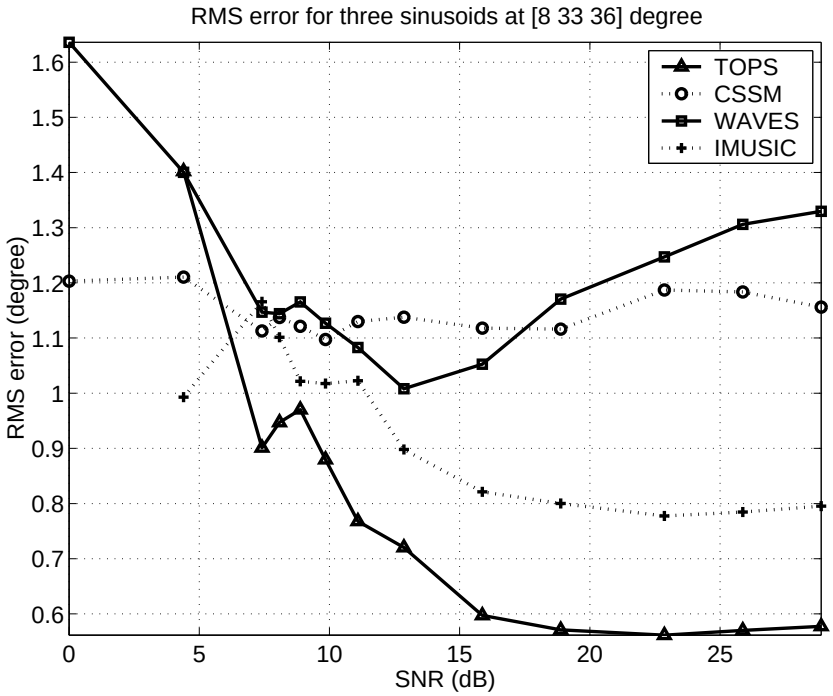

Figure 22: RMS error versus SNR of TOPS, CSSM, WAVES, and IMUSIC for third sinusoid at 36°.

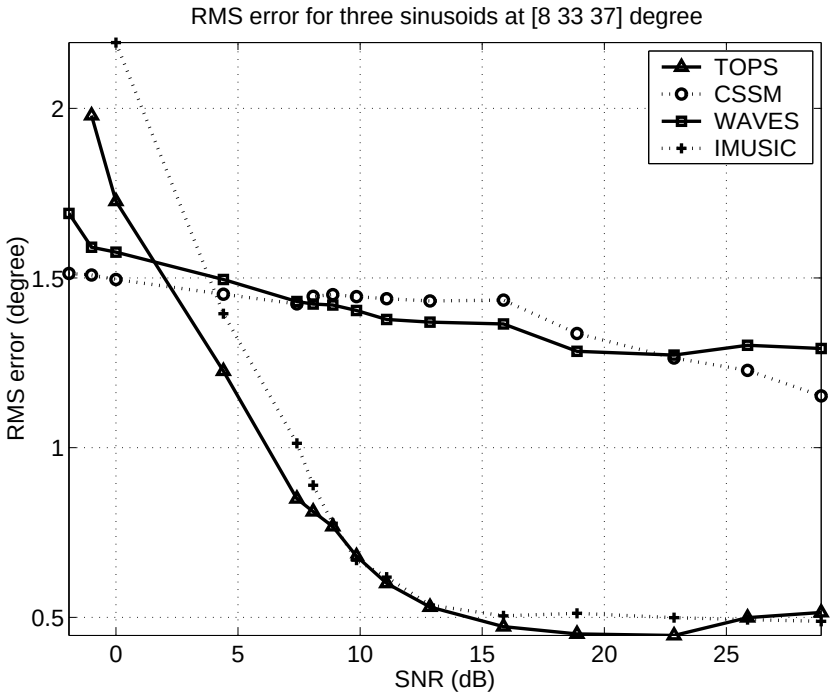

Figure 23: RMS error versus SNR of TOPS, CSSM, WAVES, and IMUSIC for third sinusoid at 37°.

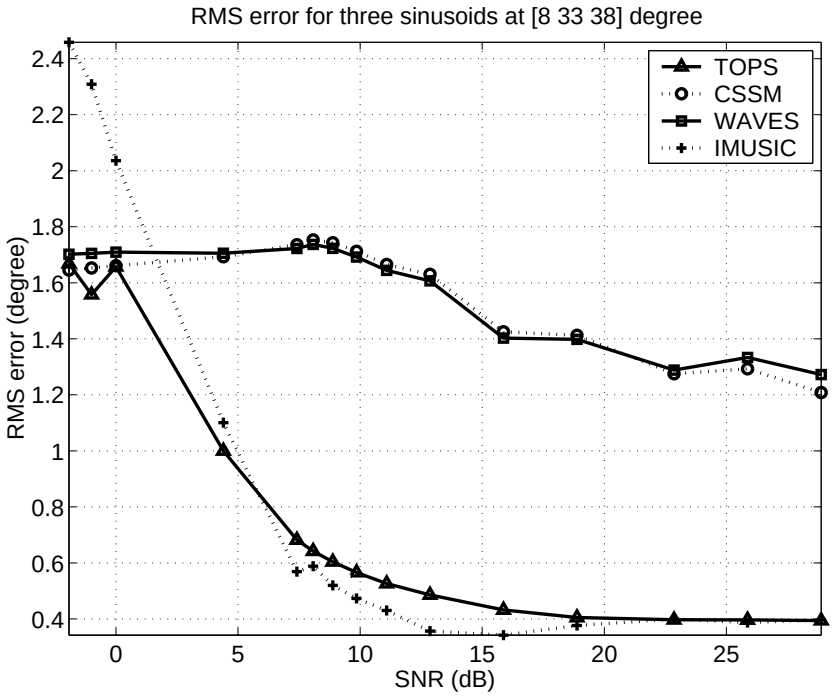

Figure 24: RMS error versus SNR of TOPS, CSSM, WAVES, and IMUSIC for third sinusoid at 38°.

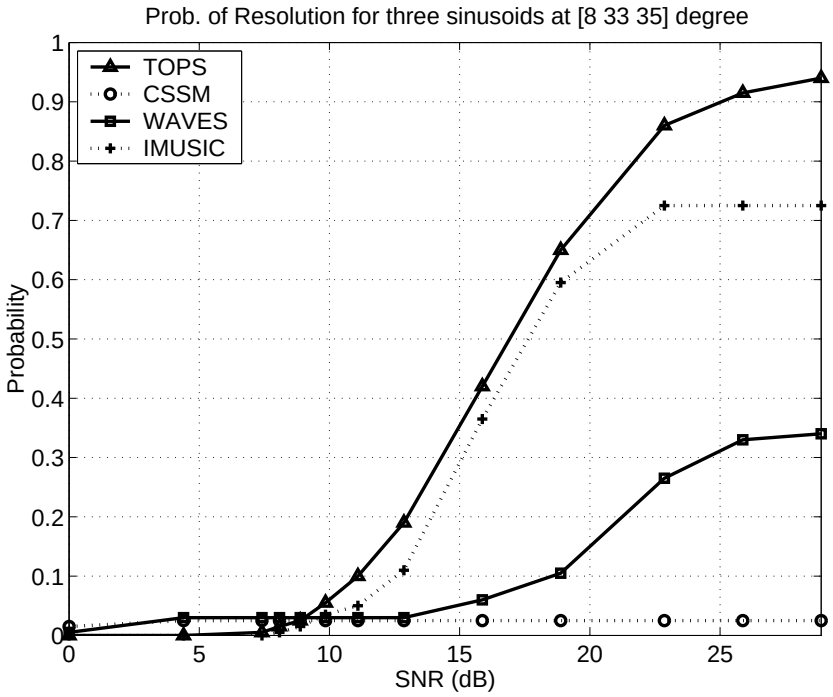

Figure 25: Probability of resolution versus SNR of TOPS, CSSM, WAVES, and IMUSIC for third sinusoid at 35°.

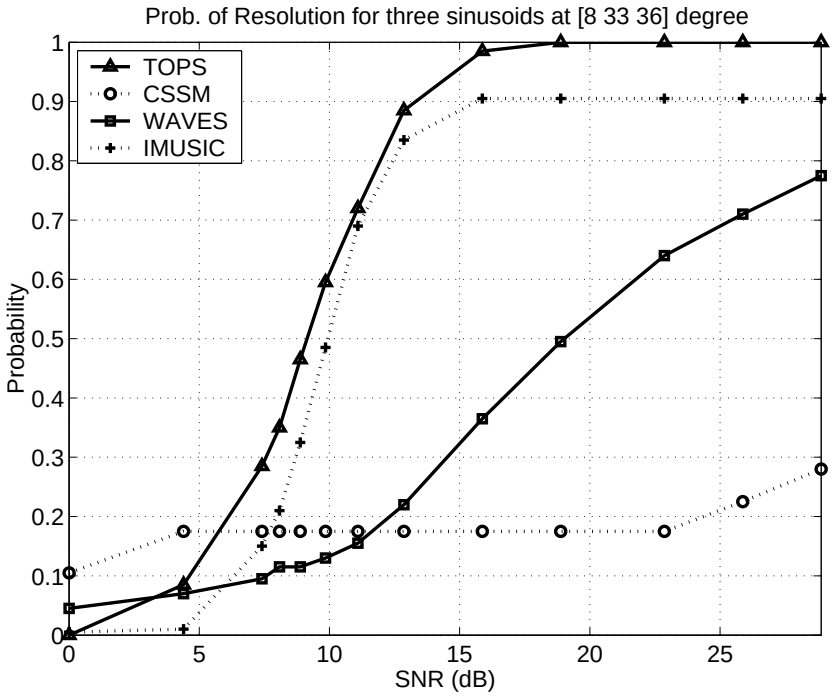

Figure 26: Probability of resolution versus SNR of TOPS, CSSM, WAVES, and IMUSIC for third sinusoid at 36°.

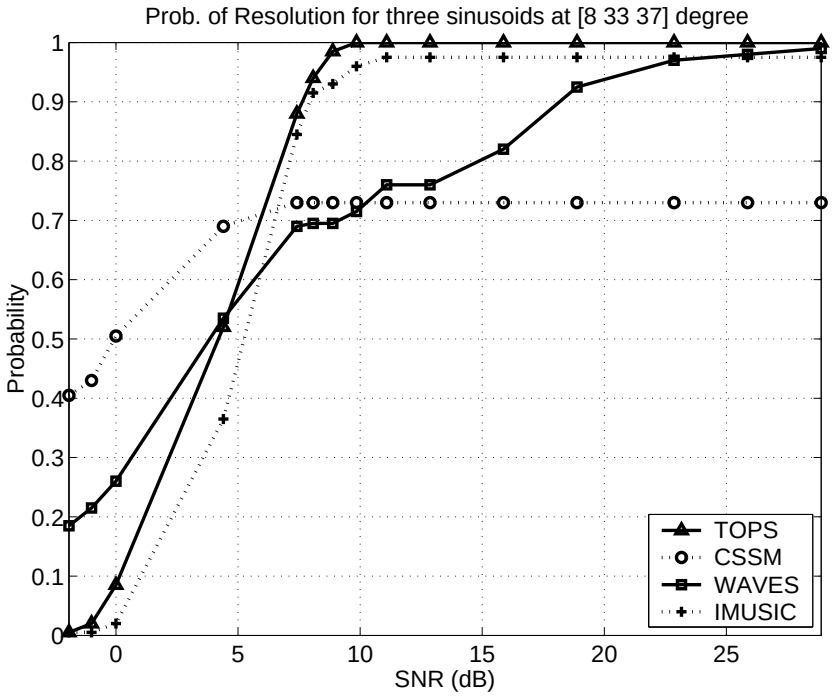

Figure 27: Probability of resolution versus SNR of TOPS, CSSM, WAVES, and IMUSIC for third sinusoid at 37°.

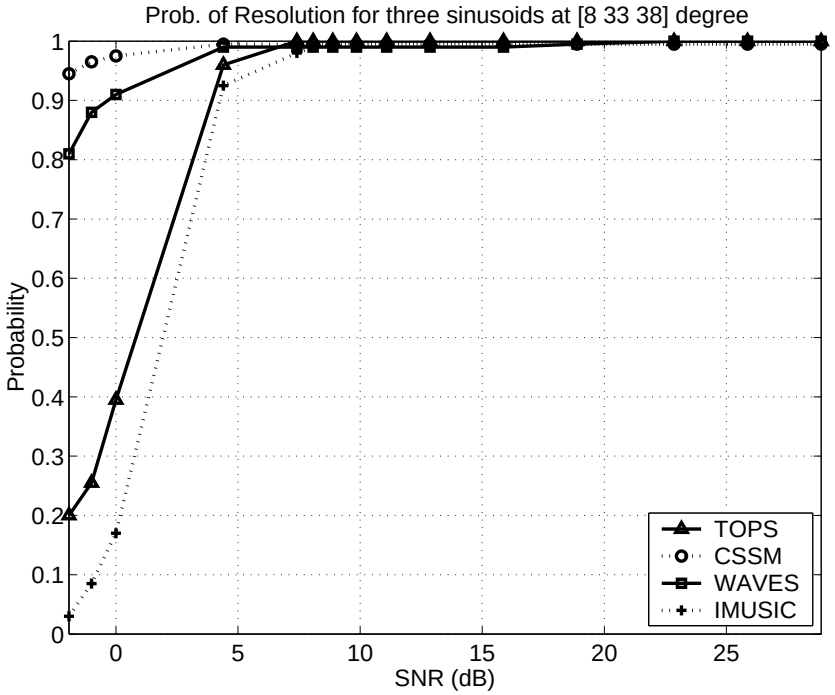

Figure 28: Probability of resolution versus SNR of TOPS, CSSM, WAVES, and IMUSIC for third sinusoid at 38°.

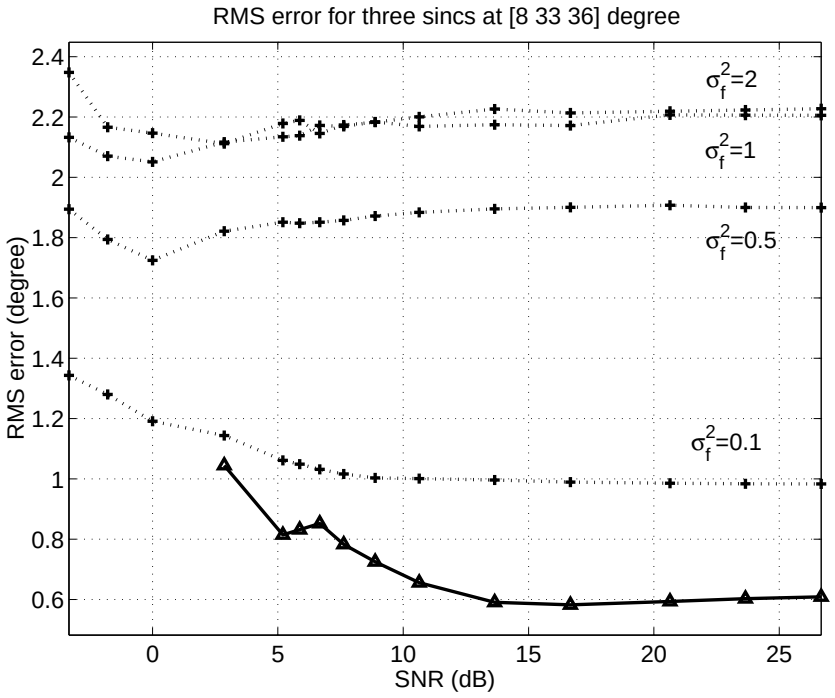

Figure 29: RMS error versus SNR of TOPS and CSSM with random focusing angles for third sinc at 36°. σ_f^2 denotes the variance of focusing angles.

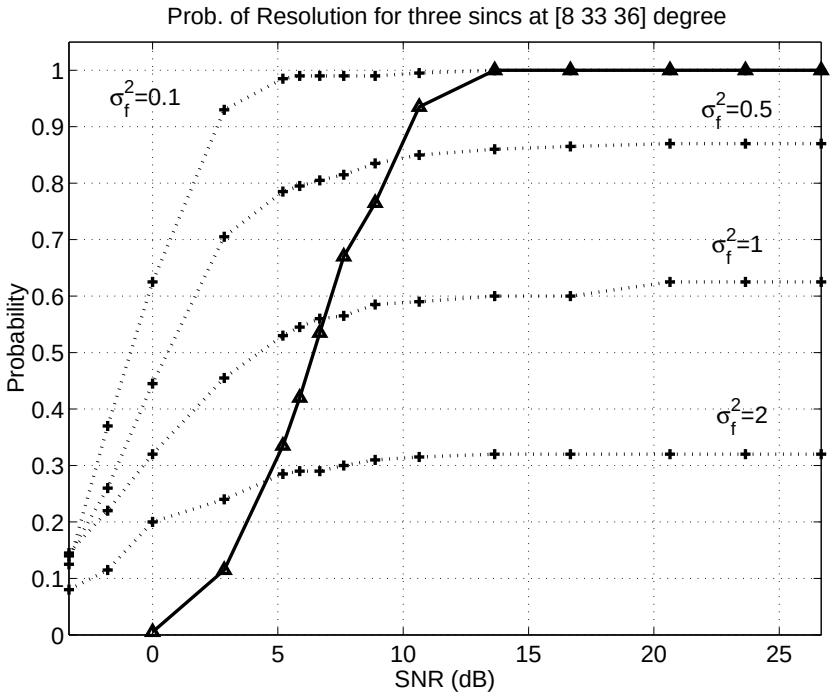

Figure 30: Probability of resolution versus SNR of TOPS and CSSM with random focusing angles for third sinc at 36°. σ_f^2 denotes the variance of focusing angles.

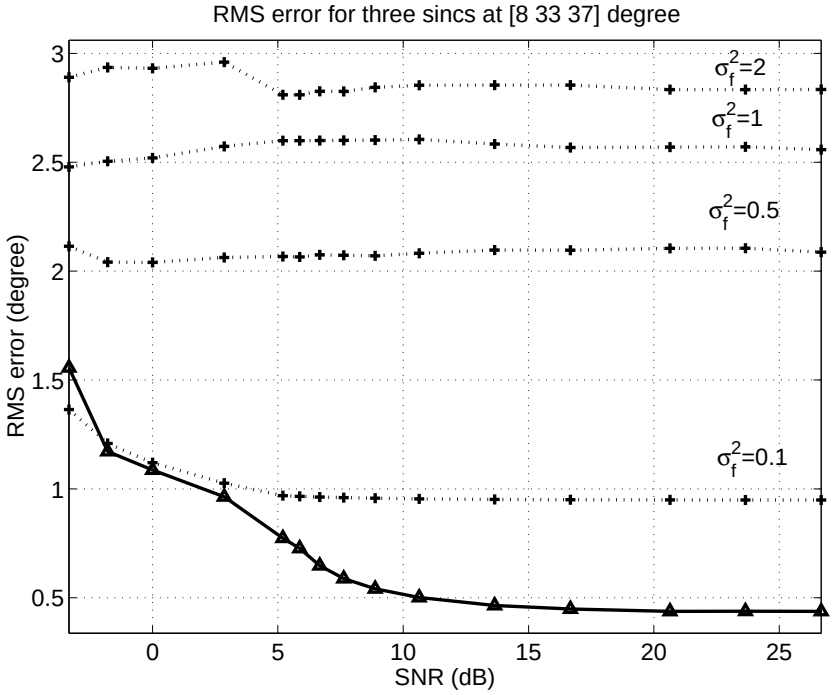

Figure 31: RMS error versus SNR of TOPS and CSSM, with random focusing angles for third sinc at 37°. σ_f^2 denotes the variance of focusing angles.

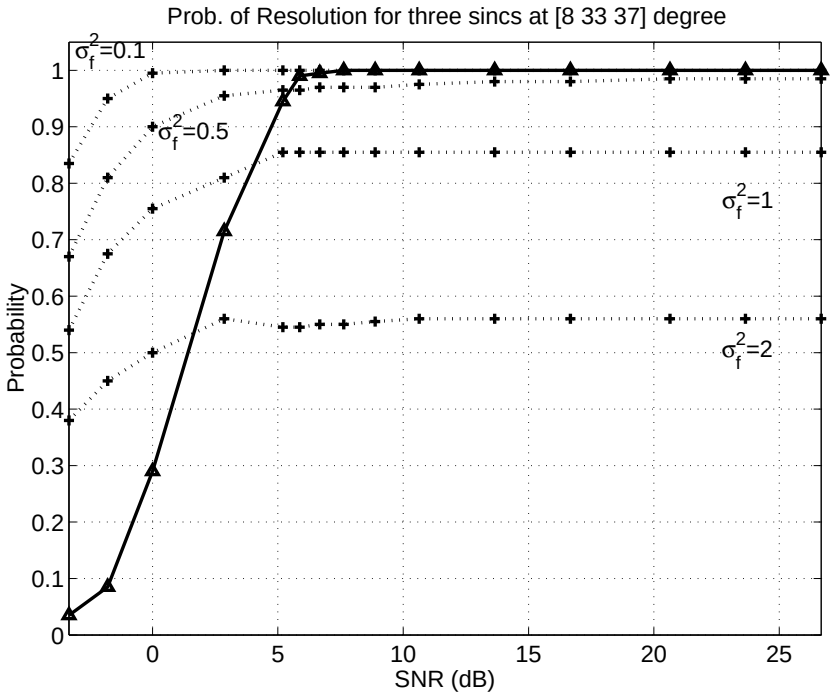

Figure 32: Probability of resolution versus SNR of TOPS and CSSM with random focusing angles for third sinc at 37°. σ_f^2 denotes the variance of focusing angles.

Even though there is little degradation in the performance, TOPS still works well with an over-estimated number of signals. Coherent methods show less robustness than incoherent methods. Like previous simulations, TOPS works better than all three others in the SNR range around $0 \sim 5$dB. IMUSIC seems to be the most robust to errors in the number of signals.

7.3.3 Case 3: Various number of frequency bins

TOPS is tested with various numbers of frequency bins, K. Since TOPS is not a coherent method, more frequency bins do not necessarily mean better estimates. TOPS is tested with three, five, seven, and nine frequency bins and the results are shown in Figs. 39 through 44. The simulation results do not show consistent characteristics regarding the number of frequency bins. It seems that the performance is dominated by the quality of the frequency components not the number of frequency bins.

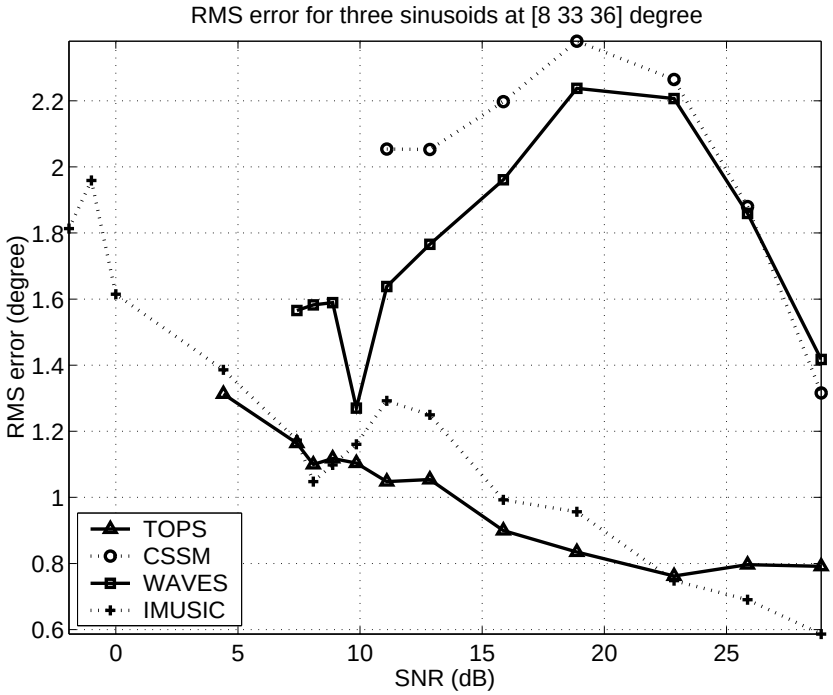

Figure 33: RMS error versus SNR with an over-estimated number of signals of TOPS, CSSM, WAVES, and IMUSIC for third sinusoid at 36°.

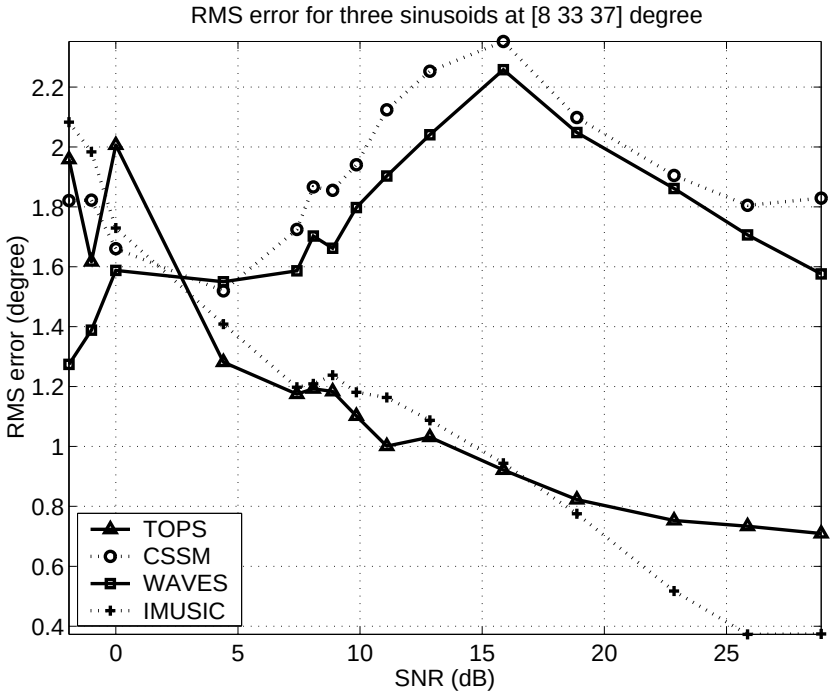

Figure 34: RMS error versus SNR with an over-estimated number of signals of TOPS, CSSM, WAVES, and IMUSIC for third sinusoid at 37°.

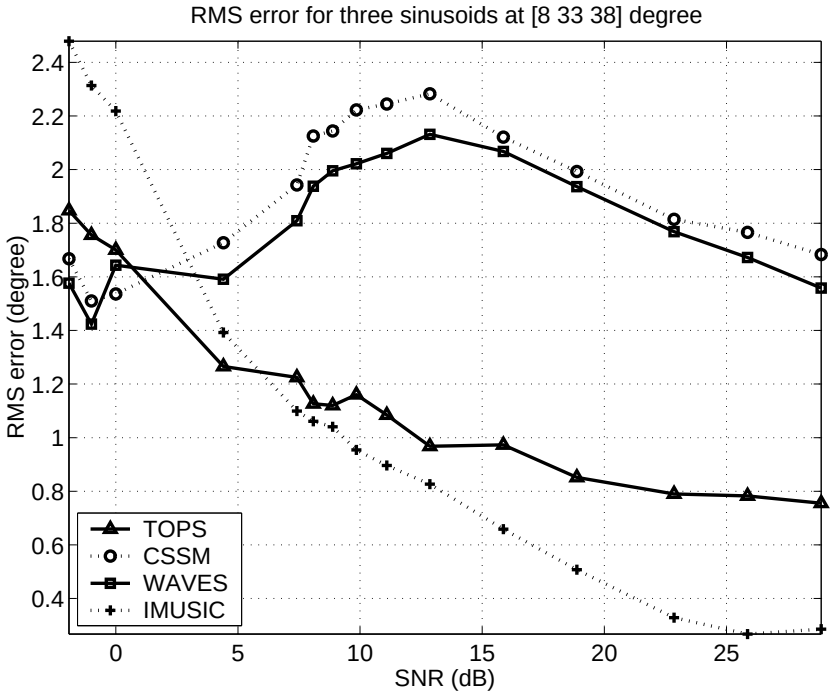

Figure 35: RMS error versus SNR with an over-estimated number of signals of TOPS, CSSM, WAVES, and IMUSIC for third sinusoid at 38°.

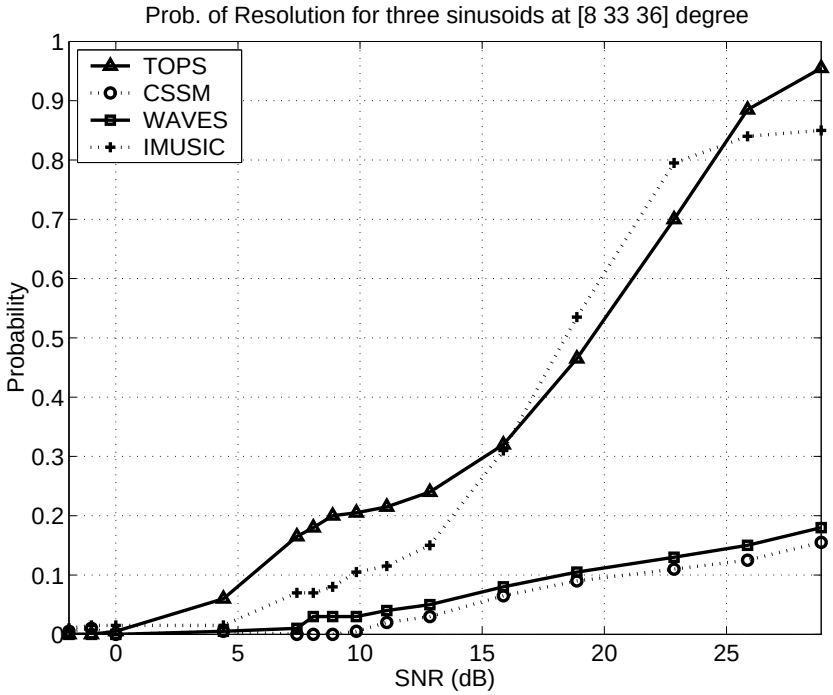

Figure 36: Probability of resolution versus SNR with an over-estimated number of signals of TOPS, CSSM, WAVES, and IMUSIC for third sinusoid at 36°.

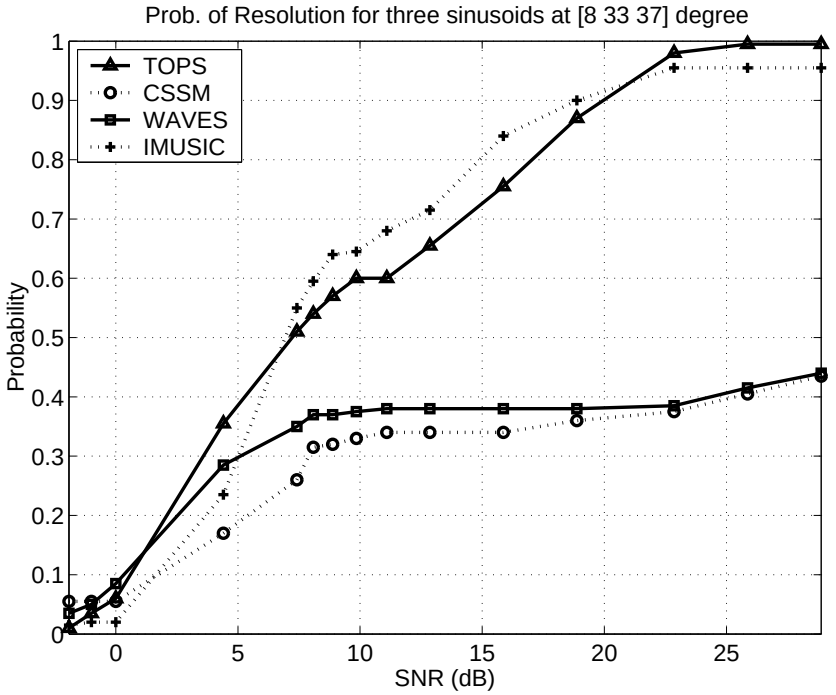

Figure 37: Probability of resolution versus SNR with an over-estimated number of signals of TOPS, CSSM, WAVES, and IMUSIC for third sinusoid at 37°.

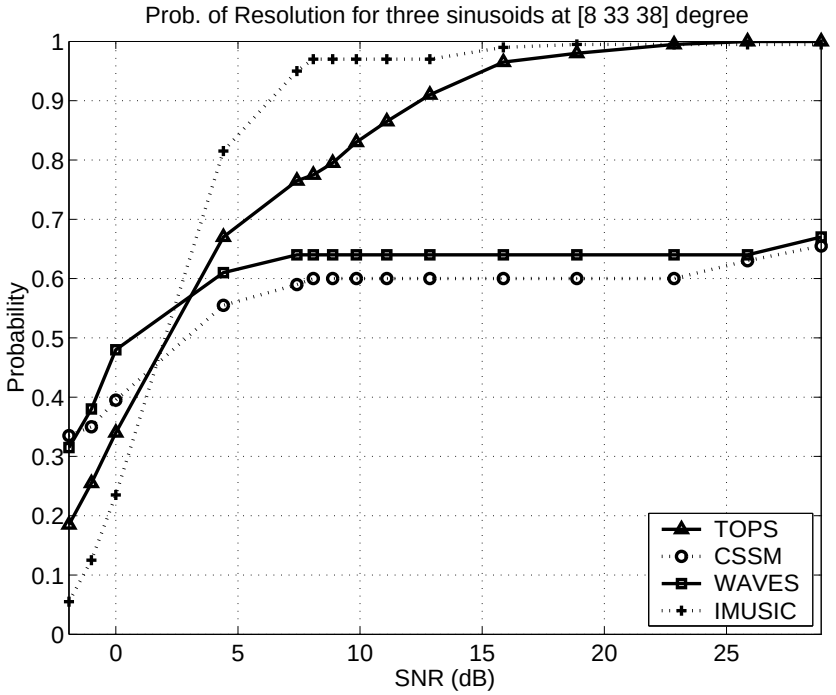

Figure 38: Probability of resolution versus SNR with an over-estimated number of signals of TOPS, CSSM, WAVES, and IMUSIC for third sinusoid at 38°.

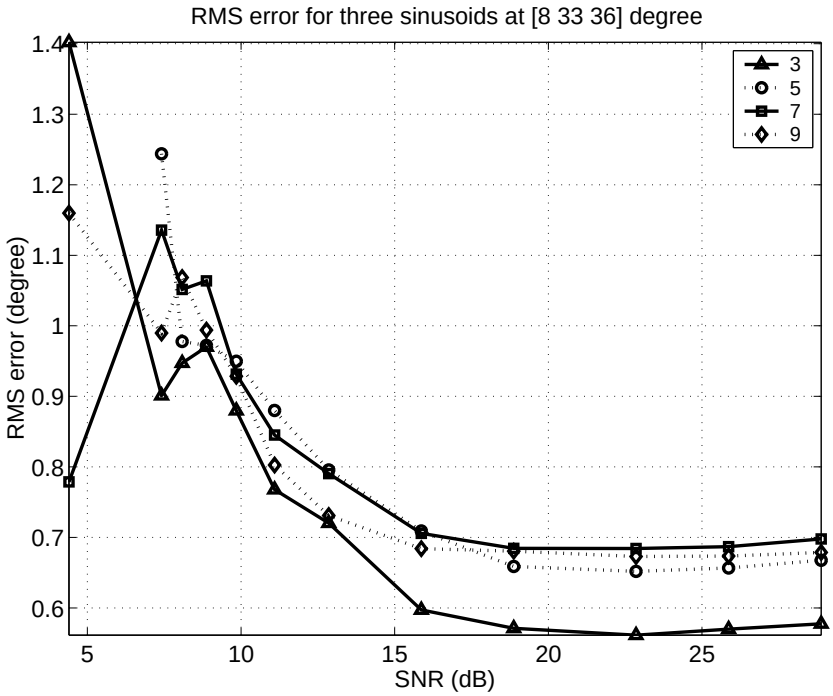

Figure 39: RMS error versus SNR of TOPS with different number of frequency bins for third sinusoid at 36°.

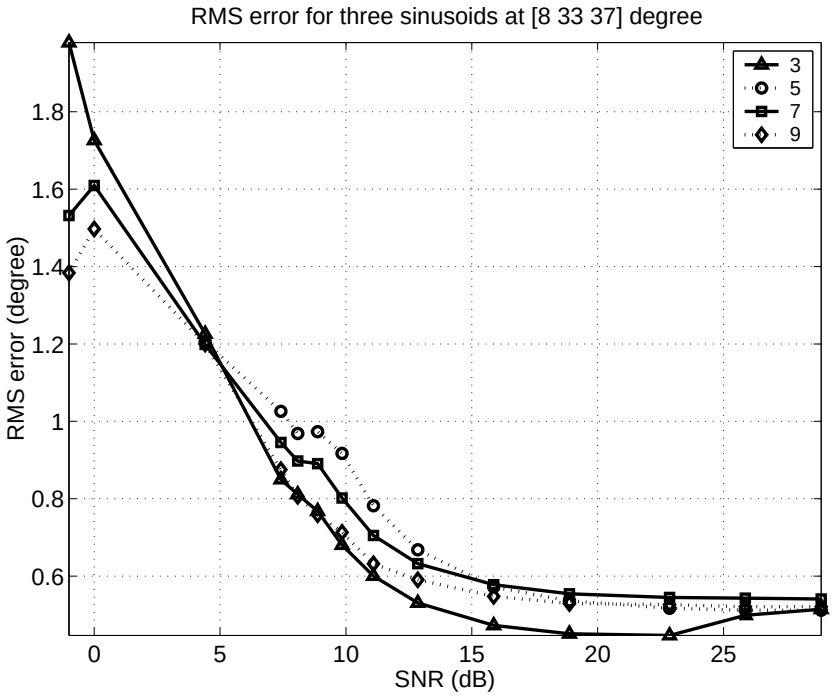

Figure 40: RMS error versus SNR of TOPS with different number of frequency bins for third sinusoid at 36°.

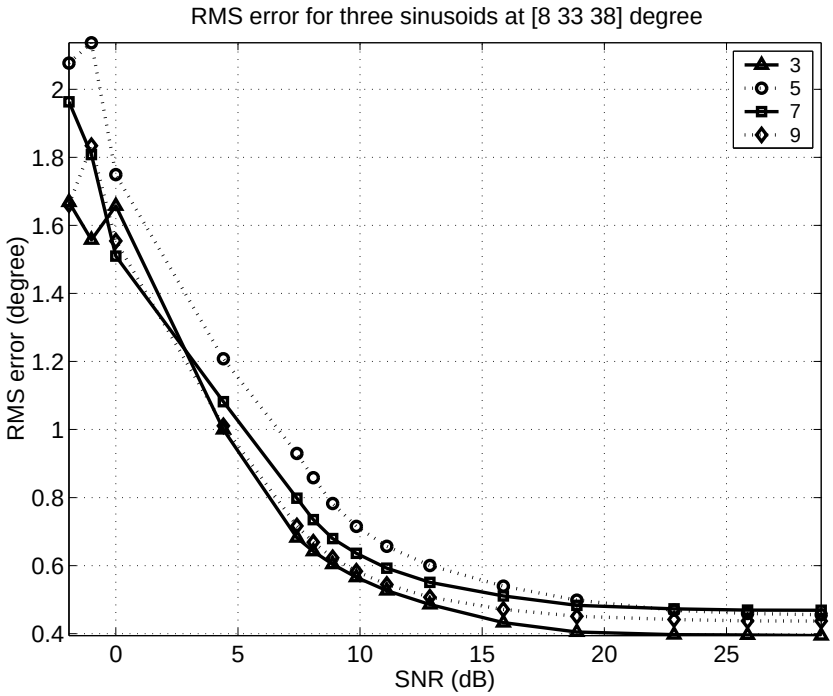

Figure 41: RMS error versus SNR of TOPS with different number of frequency bins for third sinusoid at 36°.

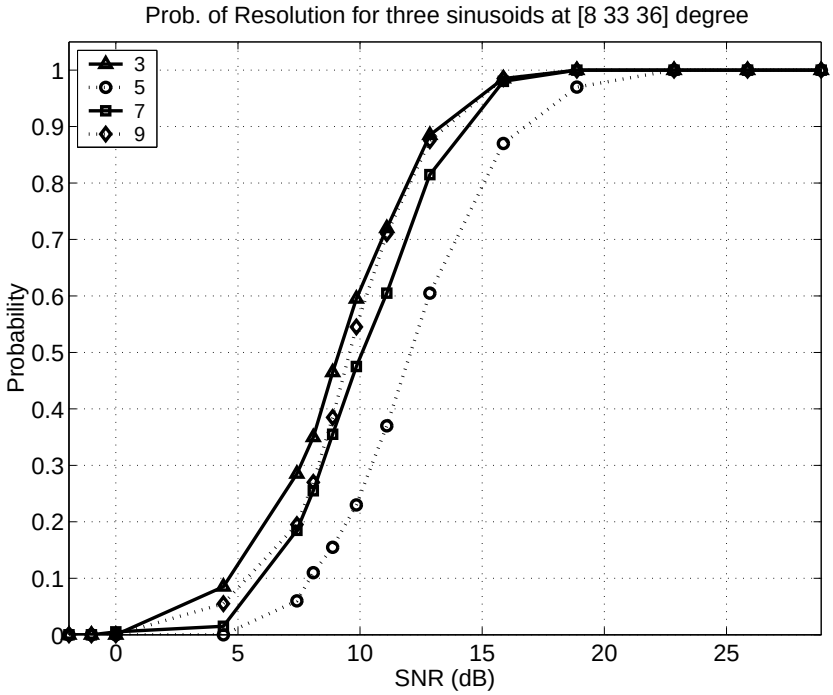

Figure 42: Probability of resolution versus SNR of TOPS with different number of frequency bins for third sinusoid at 36°.

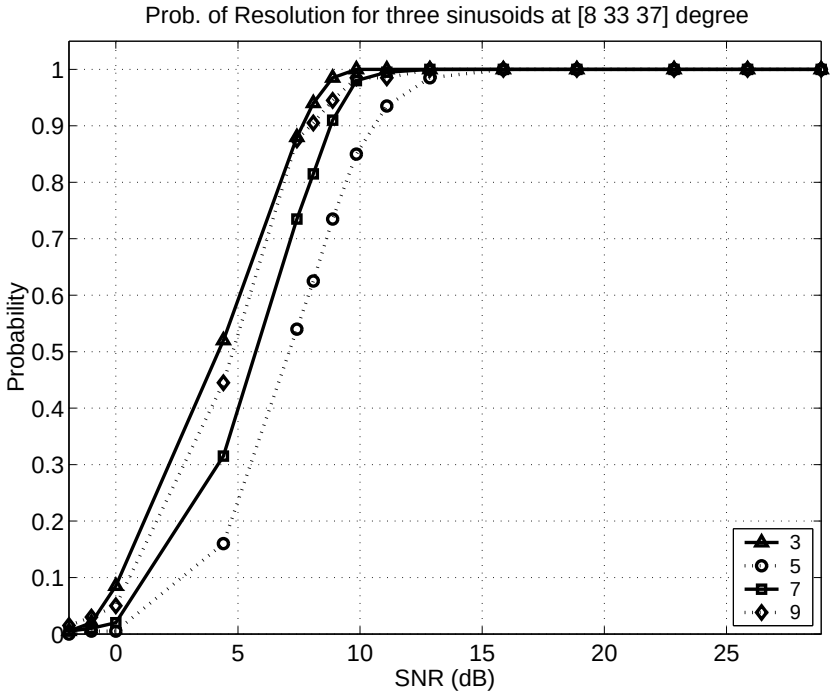

Figure 43: Probability of resolution versus SNR of TOPS with different number of frequency bins for third sinusoid at 36°.

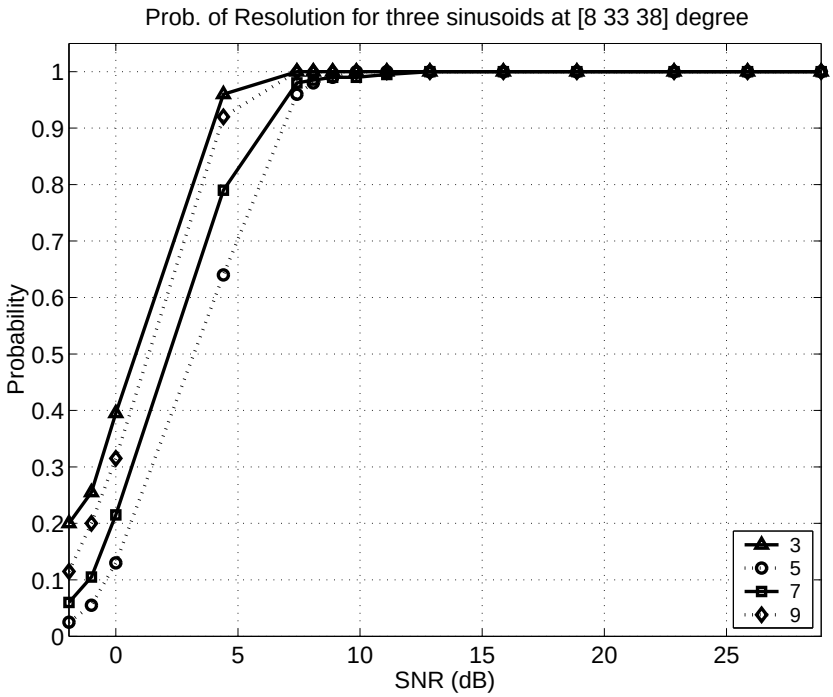

Figure 44: Probability of resolution versus SNR of TOPS with different number of frequency bins for third sinusoid at 36°.

CHAPTER 8

PROCESSING SEISMIC DATA

8.1 Seismic Signals

In applications such as medical imaging or nondestructive evaluation, active sensor arrays are used. Unlike passive sensor arrays discussed in the previous chapters, active sensor arrays not only receive but also transmit a signal. Seismic sensor arrays for buried landmine detection are used in one of those applications. In the seismic array system, multiple transmitters and multiple receivers are used. Each transmitter sends an acoustic pulse into the medium and all the receivers record the reflection at the same time. The time-domain duration of the transmitted pulse should be as short as possible in order to increase the range resolution, so its frequency bandwidth is wide. In this chapter, TOPS is tested with seismic sensor data.

8.2 Validity of TOPS

Assume that there are M_t transmitters and M_r receivers. When the j-th transmitter sends a signal and the k-th receiver receives the reflected signal from P objects, the received signal in the frequency domain, $k(\omega)$ is

$$k(\omega) = f(\omega) \sum_{l=0}^{P-1} \xi_l G(\omega, \vec{r}_l, \vec{r}_{t,j}) G(\omega, \vec{r}_l, \vec{r}_{r,k}),$$

where $f(\omega)$ is the Fourier transform of the transmitted signal, $G(\cdot)$ is the Green's function, ξ_l is the scattering coefficient of l-th target, $\vec{r}_i$ is the i-th target location, $\vec{r}_{t,j}$ is the j-th transmitter location, and $\vec{r}_{r,k}$ is the k-th receiver location (see Figure 45)

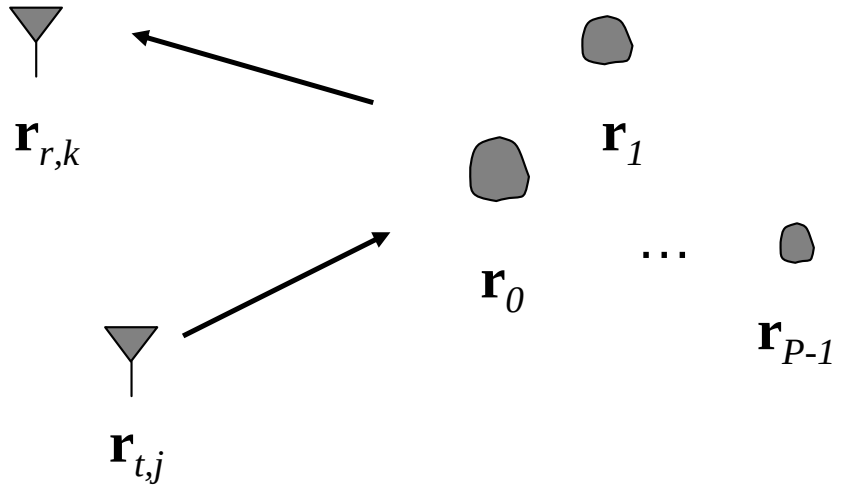

Figure 45: Schematic of the transmitter, receiver, and reflecting objects for a seismic system

[33]. Then, the transfer matrix can be represented in a matrix form as

$$\mathbf{K}(\omega) = f(\omega) \left[\begin{array}{ccc} \mathbf{g}_r(\omega, \vec{r}_0) & \cdots & \mathbf{g}_r(\omega, \vec{r}_{P-1}) \end{array} \right] \left[\begin{array}{ccc} \xi_0 & & 0 \\ & \ddots & \\ 0 & & \xi_{P-1} \end{array} \right] \left[\begin{array}{c} \mathbf{g}_t^T(\omega, \vec{r}_0) \\ \vdots \\ \mathbf{g}_t^T(\omega, \vec{r}_{P-1}) \end{array} \right], \tag{103}$$

where

$$\mathbf{g}_r(\omega, \vec{r}_i) = \left[\begin{array}{ccc} G(\omega, \vec{r}_i, \vec{r}_{r,0}) & \cdots & G(\omega, \vec{r}_i, \vec{r}_{r,M_r-1}) \end{array} \right]^T,$$

and

$$\mathbf{g}_t(\omega, \vec{r}_i) = \left[\begin{array}{ccc} G(\omega, \vec{r}_i, \vec{r}_{t,0}) & \cdots & G(\omega, \vec{r}_i, \vec{r}_{t,M_t-1}) \end{array} \right]^T.$$

The ij-th element of the transfer matrix $\mathbf{K}(\omega)$ is the transfer function between the j-th transmitter and the i-th receiver. The Green's function in two dimensions can be approximated as

$$G(\omega, \vec{r}, \vec{r'}) = \frac{j}{4} H_0^{(1)} \left\{ k(\omega) |\vec{r} - \vec{r'}| \right\},$$

where $H_0^{(1)}(\cdot)$ is the Hankel function of the first kind with zero order. Since the Green's function depends on only the distance between $\vec{r}$ and $\vec{r'}$, we can rewrite it as

$$G(\omega, \vec{r}, \vec{r'}) = G(\omega, \left| \vec{r} - \vec{r'} \right|).$$

If the transmitters and receivers are not co-located or the system is not reciprocal, then there are two autocorrelations of (103):

$$\begin{aligned} \mathbf{R}(\omega) &= \mathbf{K}(\omega)\mathbf{K}^H(\omega), \\ \mathbf{R}'(\omega) &= \mathbf{K}^H(\omega)\mathbf{K}(\omega). \end{aligned}$$

The first one is the $M_r \times M_r$ autocorrelation matrix from the receiver's point of view and the second one is an $M_t \times M_t$ matrix from the transmitter's point of view. Both are called time-reversal matrices since the complex conjugate in the frequency domain is equivalent to time-reversal $(-t)$ in the time domain [33]. The structure of both time-reversal matrices is the same as the correlation matrix of passive array signal processing. For $\mathbf{R}(\omega) = \mathbf{K}(\omega)\mathbf{K}^H(\omega)$, $\mathbf{g}_r(\omega, \vec{r}_j)$ plays the same role as the array manifold. So does $\mathbf{g}_t(\omega, \vec{r}_j)$ for $\mathbf{R}'(\omega)$. Therefore, signal subspace methods are applicable and so is TOPS.

In order to guarantee that TOPS is always working with seismic data, there are two conditions that should be satisfied as in Section 5.2. First, the transformation matrix $\mathbf{\Phi}$ should exist with seismic array manifolds. Second, the $\mathbf{D}(\phi)$ matrix should be singular only if the hypothesized ϕ matches the direction of one of the targets. Since the array manifold is different from that of previous chapters, it is necessary to check those conditions for the seismic data array manifold. The array manifold at frequency ω is

$$\mathbf{g}(\omega, \vec{r}) = \left[\begin{array}{ccc} G(\omega, z_0) & \cdots & G(\omega, z_{M-1}) \end{array} \right]^T$$

where $\vec{r} = (x, y)$ is the target's location, and z_i is the distance between $\vec{r}$ and the i-th receiver (transmitter). The asymptotic form for the 2-D Hankel function $H_0^{(1)}(z)$ along the real z axis is

$$H_0^{(1)}(z) \simeq \sqrt{\frac{2}{\pi z}} \exp\left\{ jz - j\mathrm{sgn}(z)\frac{\pi}{4} \right\}$$

for large z [7]. Since z is always positive for our case, it is possible to get rid of the

constant term $\exp(-j\pi/4)$. The simplified array manifold becomes

$$\mathbf{g}(\omega, \vec{r}) \simeq \left[\begin{array}{ccc} \frac{1}{k(\omega)z_1} e^{jk(\omega)z_1} & \cdots & \frac{1}{k(\omega)z_M} e^{jk(\omega)z_M} \end{array} \right]^T$$

Define the transformation matrix $\mathbf{\Phi}(\vec{r})$ as a diagonal matrix whose l-th diagonal element is

$$[\mathbf{\Phi}_j(\vec{r})]_l = \frac{k(\omega_0)}{k(\omega_j)} \exp\left\{j(k(\omega_j) - k(\omega_0))z_l\right\}$$

If it is multiplied with the array manifold of frequency ω_0,

$$\begin{aligned} [\mathbf{\Phi}_j(\vec{r})\mathbf{g}_0(\vec{r'})]_l &= \frac{1}{k(\omega_j)z'_l} \exp\left\{j(k(\omega_j) - k(\omega_0))z_l + jk(\omega_0)z'_l\right\} && (104) \\ &= \frac{z_l}{z'_l} \exp\left\{jk(\omega_0)(z'_l - z_l)\right\} \frac{1}{k(\omega_j)z_l} \exp\left\{jk(\omega_j)z_l\right\} && (105) \end{aligned}$$

Then,

$$\mathbf{\Phi}_j(\vec{r})\mathbf{g}_0(\mathbf{r}') = \mathbf{Q}_j(\vec{r}, \vec{r'})\mathbf{g}_j(\vec{r})$$

where $\mathbf{g}_j(\vec{r}) = \mathbf{g}(\omega_j, \vec{r})$ and $\mathbf{Q}_j(\vec{r}, \vec{r'})$ is the diagonal matrix whose l-th element is

$$\left[\mathbf{Q}_j(\vec{r}, \vec{r'})\right]_l = \frac{z_l}{z'_l} \exp\left\{jk(\omega_0)(z'_l - z_l)\right\}$$

where z_l and z'_l are the distances between the l-th sensor and $\vec{r}$ and $\vec{r'}$, respectively. If $\vec{r} = \vec{r'}$, $\mathbf{Q}_j(\vec{r}, \vec{r'})$ is the identity matrix and the transformation matrix successfully transforms the array manifold of frequency ω_0 to that of frequency ω_j. This ensures that the first condition is satisfied.

Lemma 4 *The estimator fails to work when*

$$\bigcap_{j=1}^{K} \mathcal{LN}\left\{\mathbf{g}_j^H(\vec{r})\mathbf{Q}_j^H(\vec{r}, \vec{r}_l)\mathbf{W}_j\right\} \neq \emptyset$$

for some $\vec{r}$ and $\vec{r}_l$ where $\vec{r} \neq \vec{r}_l$ and $\vec{r}_l$, $l = 0, \ldots, P-1$, where P is the number of target locations.

Above condition says that the $\mathbf{D}$ matrix loses its rank even if the hypothesized point $\vec{r}$ does not match any of the target locations. There is a possibility that the

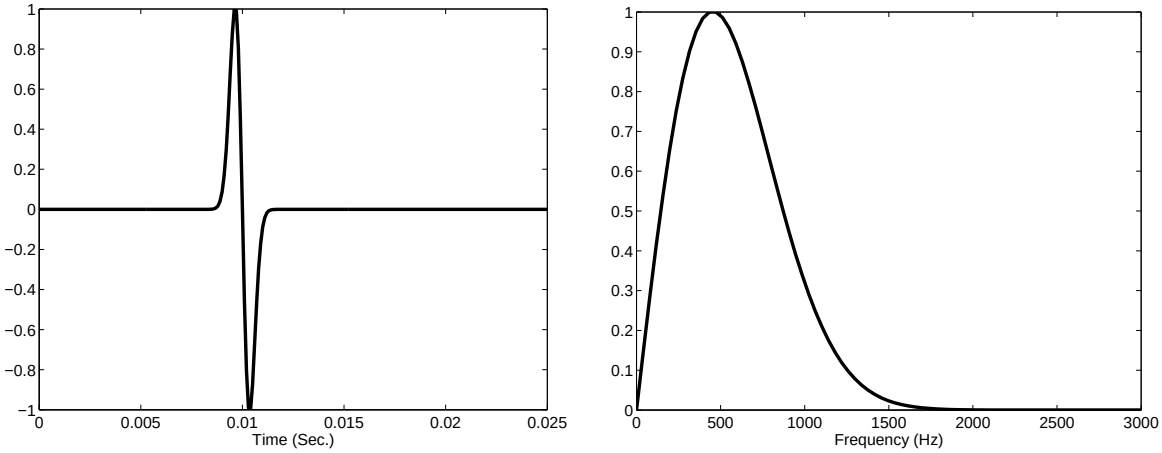

(a) Time domain (b) Frequency domain

Figure 46: Seismic pulse

above conditions are true. But, since it is a complicated condition that depends on the relative target locations, sensors, and the wavenumbers, it is hard to prove or disprove when the estimator is working. However, the failure of the estimator only means that there could be false alarms. There is no problem to find target's locations. Furthermore, if there is a single target, the first condition can not happen. The probability that the second condition is true decreases as the number of processing frequencies K increases or the number of targets decreases. This claim is supported by the results of following simulation.

8.3 Simulation

TOPS is tested with numerical data that is generated by the finite-difference time-domain (FDTD) model [42]. The medium is modelled as inhomogeneous meaning the speed of propagation depends on the frequency of the signal. The speed of propagation is assumed to be known for the processed frequency bins. The test area is 165 cm by 100 cm and a single mine whose diameter is 10 cm is buried at a depth of 2 cm. Six transmitters are placed on the y-axis with 9 cm displacement between the sensors. Fifteen receivers are also placed on the y-axis, but with 2 cm intersensor spacing. The

received data is processed so that it contains only reflections from the target, not the transmitted pulse. The transmitted pulse is a differentiated Gaussian pulse at 450 Hz. Figure 46 shows the pulse in both the time and frequency domains. Note that the target is not a point-target since its diameter is comparable to the wavelength at 450Hz. The correlation matrix is formed from the receiver's point of view making a 15×15 matrix. Although the landmine is not a point-target, only one significant eigenvalue appears among the 15 eigenvalues. Seven frequency bins around 450 Hz are processed for TOPS and IMUSIC since the power spectral density is high in those frequency bins. Figs. 47 and 48 shows the results of both methods. The image is normalized and everything below -20 dB has been removed. The white circle denotes the true location of the target at (125,40). The size of the circle also represents the actual size of the target. Although there seems to be a bias in the estimated range of target location for both methods, TOPS showed a higher resolution image in both cross-range and down-range than IMUSIC.

Note that the difference between these images and those in Figs. 19 and 20. Figures shown here are the results of target processing with a 1-D seismic sensor array. Therefore, the target is localized in the spatial domain. Since the array is linear, it shows lower down-range resolution than cross-range resolution. On the other hand, Figures 19 and 20 show the results of DOA estimation for far-field targets with 2-D array. The x-axis and y-axis in those figures represent the azimuth and the elevation angles, respectively while the axis in Figs. 47 and 48 represent down-range and cross-range.

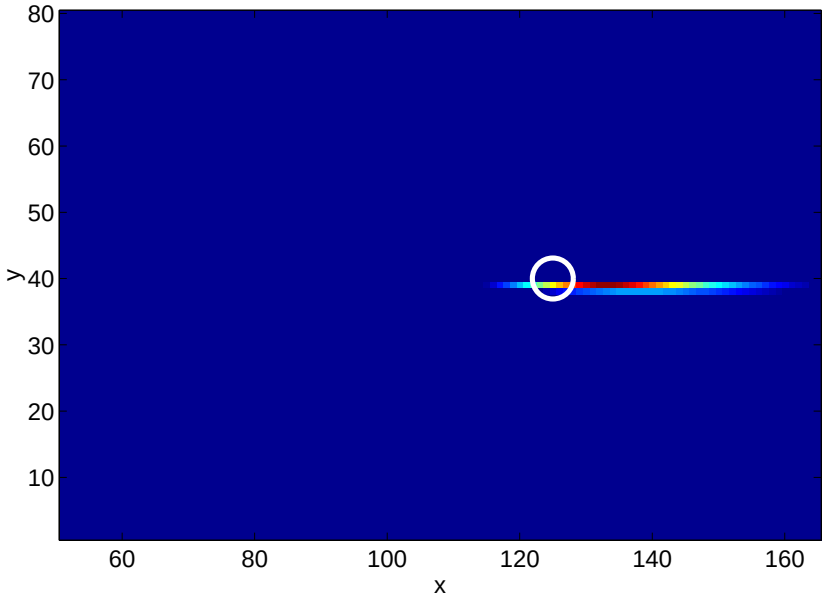

Figure 47: Result image of TOPS for seismic data

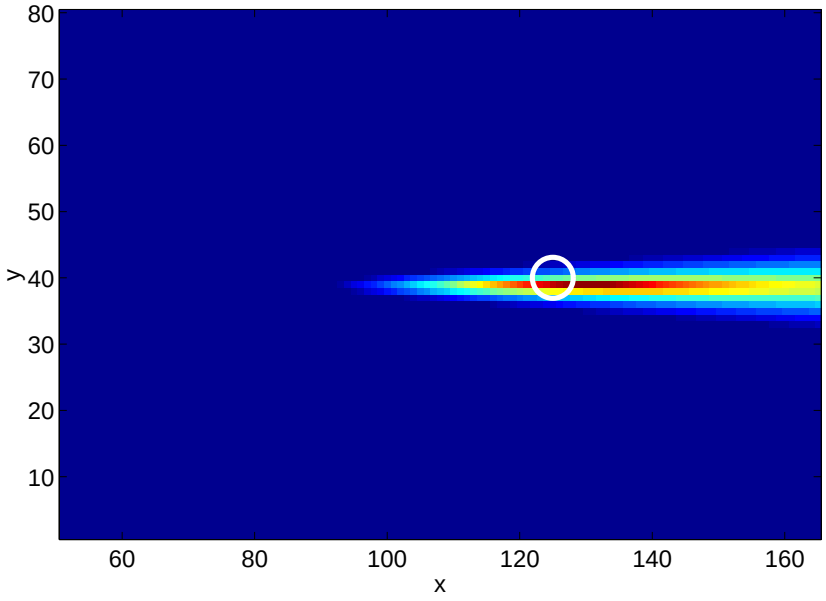

Figure 48: Result image of IMUSIC for seismic data

CHAPTER 9

CONCLUSIONS

9.1 Contributions

This thesis presents two methods of DOA estimation for wideband signals with sensor arrays. One is the pruned fast beamformer which is appropriate for low resolution estimation. The other is TOPS for high resolution estimation.

9.1.1 Pruned Fast Beamformer (PFB)

DS beamforming is a very intuitive beamforming method. Since it is implemented in the time domain, a DS beamformer is more robust to modelling errors than a frequency domain beamformer and it is also valid for both narrowband and wideband signals. One of the main disadvantages of DS beamforming is its high computational cost. Fast beamforming is one way to reduce the number of computations of a DS beamformer [34]. This multi-stage multi-resolution beamformer can reduce the number of computations from $O(n^3)$ to $O(n^2 \log n)$. The PFB can save processing time even more by integrating a signal detector into the pruning. This detection strategy in the intermediate stages can save computations by stopping further processing from resolving benign angular sectors that do not contain any coherent sources. The computer simulations in Chapter 4 showed the efficiency of the PFB when there is single target. The validity of the PFB was also validated by an error analysis. However, the PFB is not always efficient. When a large number of signals are distributed over a wide range of angles, the PFB loses its efficiency since, for this case, almost all sectors will pass the detector threshold and the PFB will have to compute the detection statistics for each sector without the benefit of pruning sectors. When the number of

signals is small, the DOA estimates from the PFB could be used as initial values for ML estimators or focusing angles in the coherent methods.

9.1.2 TOPS

DOA estimation is one of the main applications in using sensor arrays and many methods have been proposed to get better estimates. Most DOA methods are valid only for narrowband signals where the difference between received signals at each sensor can be modelled as just phase differences. If the signals are wideband, the difference between sensor outputs depends not only on the phase but also on the magnitude difference. The signals are more difficult to deal with than narrowband signals since the rank-one property does not hold. For this reason, there are relatively few wideband DOA algorithms compared to narrowband methods. Furthermore, most wideband methods focus on how to convert (transform) the received signals or statistics of those into a form such that narrowband techniques can be applied. Since errors in the conversion process are inevitable, the performance of those estimators has limits. Focusing angles, which are necessary to find transformation matrices, seem to dominate the overall performance of the estimator so that there is no processing gain when the focusing angles deviate a lot from the true DOAs. Sometimes, this makes coherent methods even worse than incoherent methods when the received signal is in favorable conditions, e.g., high SNR and well-separated sources.

On the other hand, incoherent methods which process decomposed narrowband signals independently suffer from inconsistency in the estimates from frequency to frequency. This may cause more errors in estimates than when single frequency bins are processed. Furthermore, in the low SNR case, all of the independent DOA estimates would fail to find sources. Even one outlier can make the final estimates far from the true DOAs.

The new DOA estimator, TOPS, introduces a new way to use multiple incoherent

signal subspaces at the same time without a focusing angle requirement. The strategy of TOPS is unique since its performance falls in between the incoherent and the coherent methods although its performance is closer to the incoherent methods. It would be fair to call TOPS a non-incoherent method. A comparison with other existing methods is given in the following sections.

9.1.2.1 Comparison with the coherent methods

There are two advantages of coherent methods. First, they seem to work better in the low SNR case. Since the correlation matrices of different frequency bins are coherently added and averaged, some of the noise is cancelled out and improves the estimators. Second, during the averaging process, correlation between sources and also spatial aliasing are reduced. On the other hand, the coherent methods require 'good' transformation matrices in order to transform one subspace into another (desired) subspace. However, it is impossible to avoid errors in the transformation matrix since we do have perfect knowledge of both the original subspace and the desired subspace. The subspaces are guessed from the focusing angles which are the result of preprocessing. TOPS avoids those subspace transformations and uses a basis transformation instead. Therefore, it does not require preprocessing and does not introduce transformation errors. This is the main advantage of TOPS over coherent methods.

9.1.2.2 Comparison with the incoherent methods

Incoherent methods show fairly good performance in favorable SNR situations. This is reasonable since most independent narrowband DOA estimators work well in those situations. In the comparisons shown in Chapter 7, the performance of IMUSIC was as good as that of TOPS in high SNR cases. However, sometimes, multiple peaks which cause misleading estimates appear even in well-separated sources. TOPS does not show those artifacts since it is not an average of multiple narrowband estimates.

9.2 Future Work

In this section, several directions for future work are suggested.

9.2.1 Wideband methods or Narrowband methods?

When the SNR is high enough, the DOA of wideband signals can be estimated by processing individual frequency bins. In this case, using multiple signals can even degrade the estimator performance. When we deal with wideband signals, first we need to decide which method should be used, wideband methods or narrowband methods (single frequency bins).

9.2.2 Improving Robustness

The singular value decomposition is very sensitive to errors in the correlation matrix. Since the TOPS estimator relies on the smallest singular value of the **D** matrix, the estimator performance could be degraded severely by small errors in **D**. If the array manifold vector has errors due to non-uniform sensor response or errors in the sensor locations, the estimator performance will be unpredictable. This robust problem exists not only for TOPS but for other coherent methods. Research is needed on methods of improving robustness.

APPENDIX A

SIMULATION RESULTS FOR SINC

Simulation results not shown in Chapter 7 are given in this Appendix. These are the estimation results when the source signal is a sinc and the number of signals is known to the processor. Three signals are present. Two signals are at 8° and 33° and the location of the third signal is varying from 35° to 38° depending on the scenario. 200 Monte-Carlo runs were done to find the performance statistics. The overall performances of the four different estimators are similar to the result shown in Figs. 21 through 28 in Chapter 7 where the source signal is sum of exponentials.

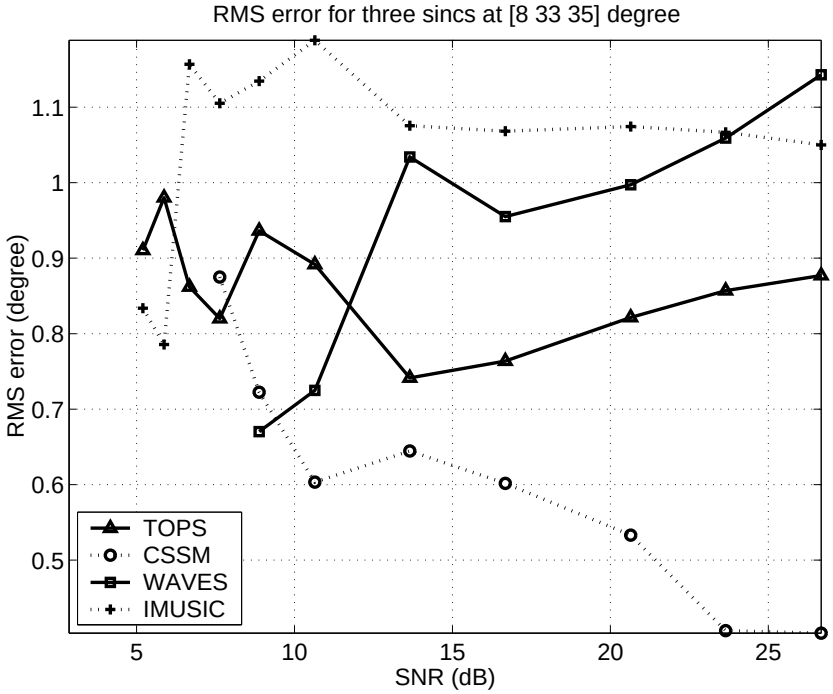

Figure 49: RMS error versus SNR of TOPS, CSSM, WAVES, and IMUSIC for third sinc at 35°.

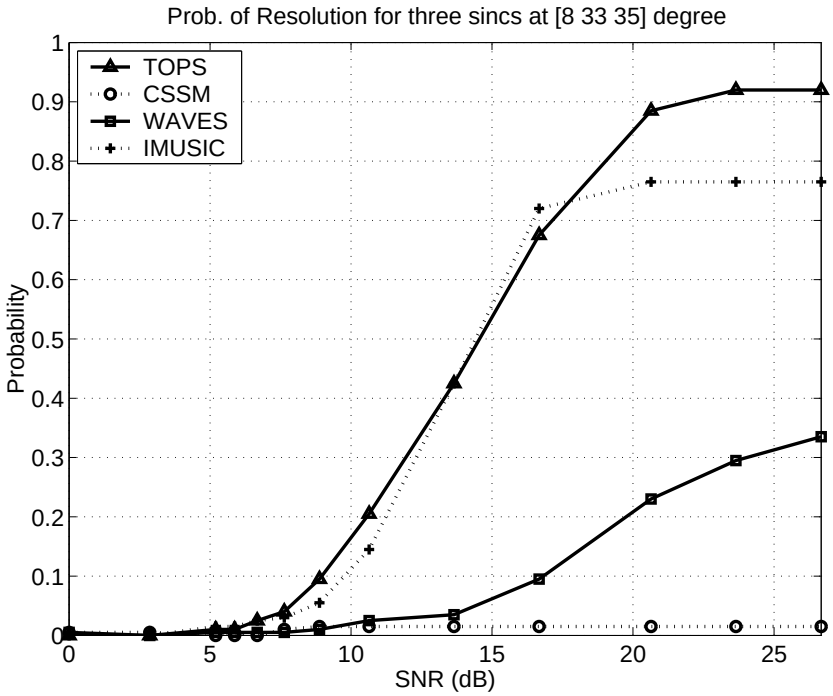

Figure 50: Probability of resolution versus SNR of TOPS, CSSM, WAVES, and IMUSIC for third sinc at 35°.

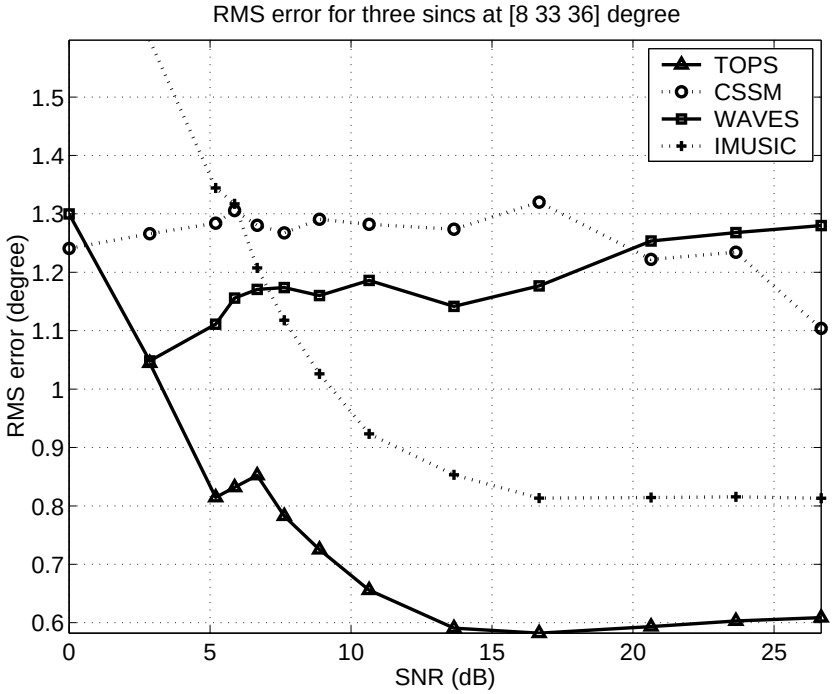

Figure 51: RMS error versus SNR of TOPS, CSSM, WAVES, and IMUSIC for third sinc at 36°.

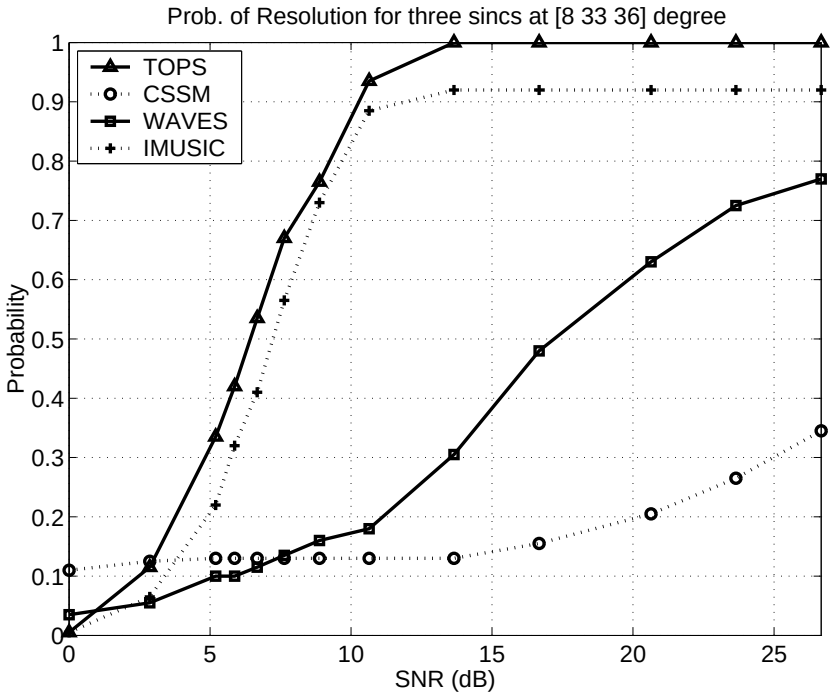

Figure 52: Probability of resolution versus SNR of TOPS, CSSM, WAVES, and IMUSIC for third sinc at 36°.

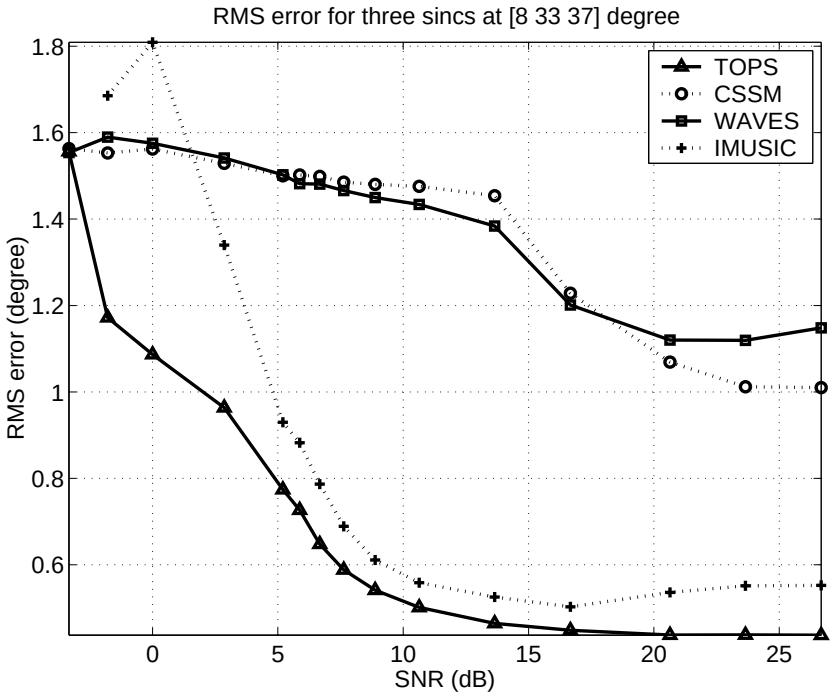

Figure 53: RMS error versus SNR of TOPS, CSSM, WAVES, and IMUSIC for third sinc at 37°.

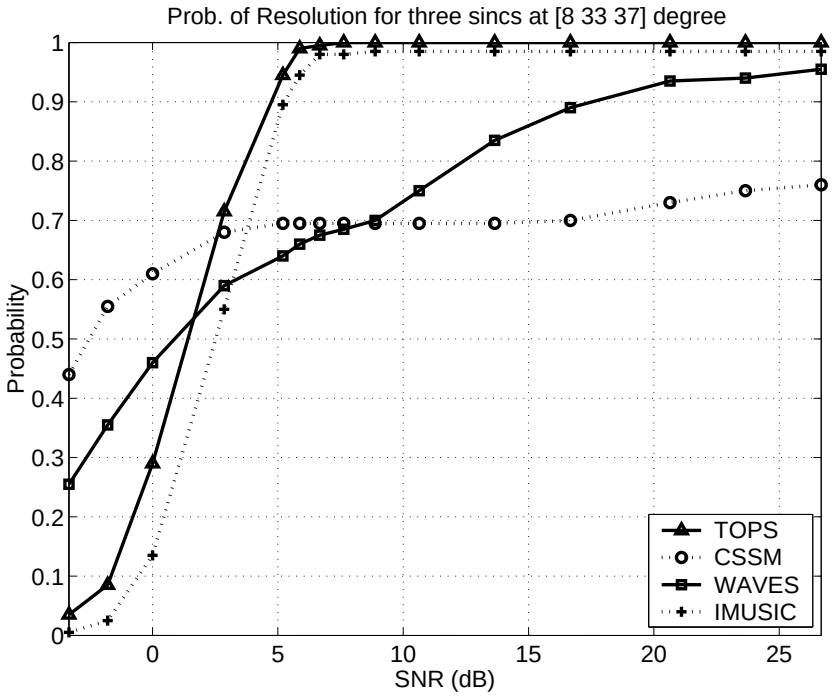

Figure 54: Probability of resolution versus SNR of TOPS, CSSM, WAVES, and IMUSIC for third sinc at 37°.

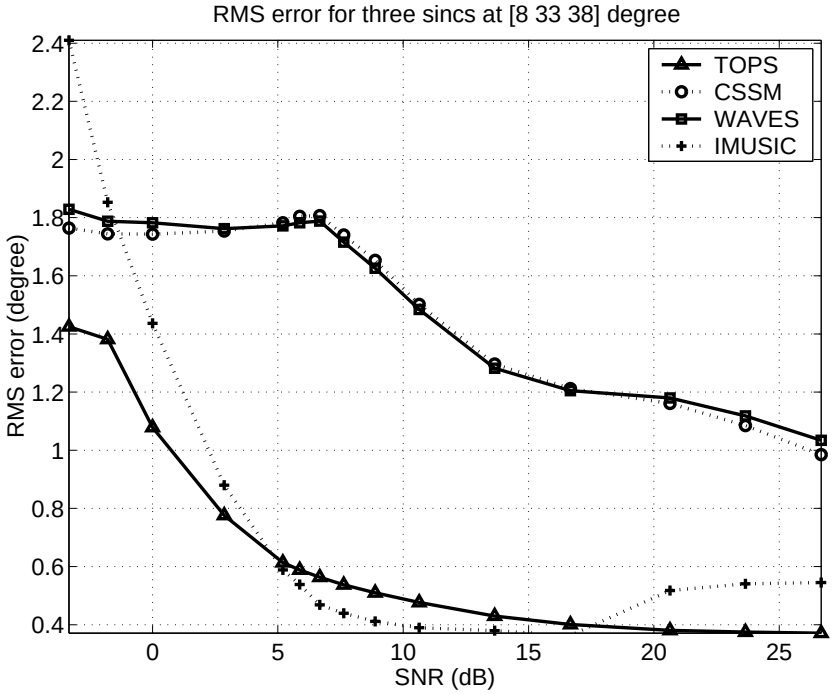

Figure 55: RMS error versus SNR of TOPS, CSSM, WAVES, and IMUSIC for third sinc at 38°.

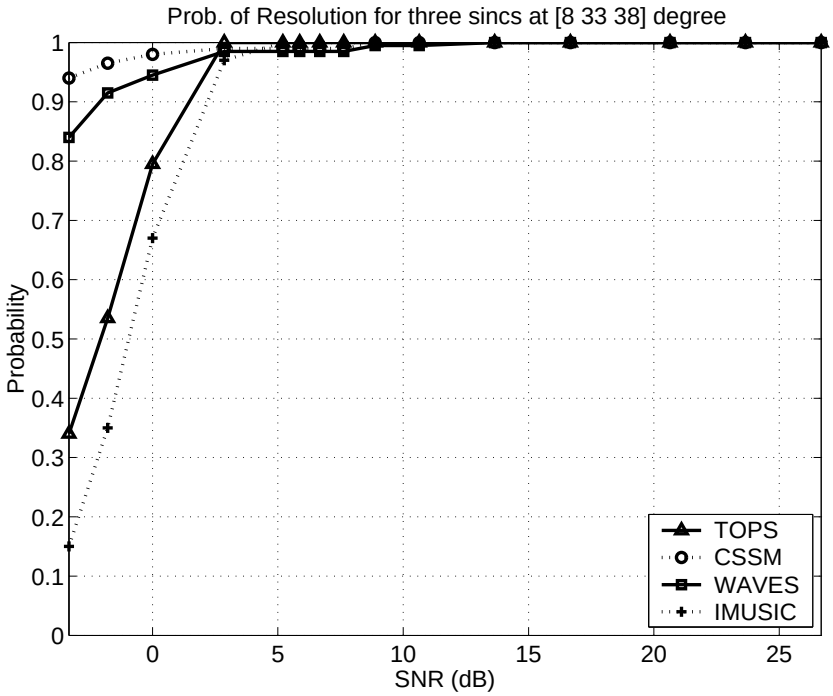

Figure 56: Probability of resolution versus SNR of TOPS, CSSM, WAVES, and IMUSIC for third sinc at 38°.

REFERENCES

[1] Agrawal, M. and Prasad, S., "DOA estimation of wideband sources using a harmonic source model and uniform linear array," *IEEE Trans. Signal Processing*, vol. 47, pp. 619–629, Mar. 1999.

[2] Agrawal, M. and Prasad, S., "Broadband DOA estimation using spatial-only modeling of array data," *IEEE Trans. Signal Processing*, vol. 48, pp. 663–670, Mar. 2000.

[3] Akaike, H., "A new look at the statistical model identification," *IEEE Trans. on Automatic Control*, vol. AC-19, pp. 716–723, Dec. 1974.

[4] Alam, M., McClellan, J., Norville, P., and Scott, W., "Time-reverse imaging for the detection of landmines," in *Proc. of SPIE Defense and Security Symposium*, (Orlando, FL), Apr. 2004.

[5] Barabell, A., "Improving the resolution performance of eigenstructure-based direction-finding algorithms," in *Proc. IEEE Acoustics, Speech, and Signal Processsing (ICASSP'83)*, (Boston, MA), May 1983.

[6] Bienvenu, G., "Eigensystem properties of the sampled space correlation matrix," in *IEEE Int. Conf. Acoustics, Speech, and Signal Processsing*, 1983.

[7] Bleistein, N., Cohen, J., and J. Stockwell, J., *Mathematics of multidimensional seismic imaging, migration, and inversion*. New York, NY: Springer, 2001.

[8] Buckley, K. and Griffiths, L., "Broad-band signal-subspace spatial-spectrum (BASS-ALE) estimation," *IEEE Trans. Acoust., Speech, Signal Processing*, vol. 36, pp. 953–964, July 1988.

[9] Buckley, K. and Griffiths, L., "Eigenstructure based broadband source location estimation," in *IEEE Int. Conf. Acoustics, Speech, and Signal Processsing*, pp. 1869–1872, 1986.

[10] Capon, J., "High-resolution frequency-wavenumber spectrum analysis," *Proc. IEEE*, vol. 57, Aug. 1969.

[11] Chen, C.-T., *Linear System Theory and Design*. Saunder College Publishing, 1984.

[12] Claudio, E. D. and Parisi, R., "WAVES: Weighted average of signal subspaces for robust wideband direction finding," *IEEE Trans. Signal Processing*, vol. 49, pp. 2179–2190, Oct. 2001.

[13] Doron, M. and Weiss, A., "On focusing matrices for wide-band array processing," *IEEE Trans. Signal Processing*, vol. 40, pp. 1295–1302, June 1992.

[14] Doron, M., Weiss, A., and Messer, H., "Maximum-likelihood direction finding of wide-band sources," *IEEE Trans. Signal Processing*, vol. 41, pp. 411–414, Jan. 1993.

[15] Friedlander, B. and Weiss, A., "Direction finding for wide-band signals using an interpolated array," *IEEE Trans. Signal Processing*, vol. 41, pp. 1618–1635, Apr. 1993.

[16] Gelli, G. and Izzo, L., "Cyclostationarity-based coherent methods for wideband-signal source location," *IEEE Trans. Signal Processing*, vol. 51, pp. 2471–2482, Oct. 2003.

[17] Gershman, A. and Amin, M., "Wideband direction-of-arrival estimation of multiple chirp signals using spatial time-frequency distributions," *IEEE Signal Processing Lett.*, vol. 7, pp. 152–155, June 2000.

[18] Gershman, A., Pesavento, M., and Amin, M., "Estimating parameters of multiple wideband polynomial-phase sources in sensor arrays," *IEEE Trans. Signal Processing*, vol. 49, pp. 2924–2934, Dec. 2001.

[19] Golub, G. and Loan, C. V., *Matrix Computations*. Baltimore,MD: Johns Hopkins Univ. Press, 1996.

[20] Ho, M. T., "A comparison of wideband subspace methods for direction-of-arrival estimation," Master's thesis, Ohio State University, Columbus, OH, 2002.

[21] Hung, H. and Kaveh, M., "Focusing matrices for coherent signal-subspace processing," *IEEE Trans. Acoust., Speech, Signal Processing*, vol. ASSP-36, pp. 1272–1282, Aug. 1988.

[22] Hung, H. and Kaveh, M., "Coherent wide-band esprit method for direction-of-arrival estimation of multiple wide-band sources," *IEEE Trans. Acoust., Speech, Signal Processing*, vol. ASSP-36, pp. 354–356, Aug. 1990.

[23] Hussain, M., "Ultra-wideband impulse radar - an overview of the principles," *IEEE AES Systems Magazine*, pp. 9–14, Sept. 1998.

[24] Johnson, D. and Dudgeon, D., *Array Signal Processing: Concepts and techniques*. Englewood Cliffs, NJ: Prentice Hall, 1993.

[25] Kaplan, L., Oh, S.-M., Cobb, M., and McClellan, J., "Error analysis for quadtree image formation," in *Proc. Intl. Conf. Image Processing*, 2000.

[26] Kaplan, L., McClellan, J., and Oh, S.-H., "Prescreening during image formation for ultra-wideband radar," *IEEE Trans. on Aerospace and Electronic Systems*, vol. 38, pp. 74–88, Jan. 2002.

[27] Kaveh, M. and Barabell, A., "Statistical performance of the MUSIC and minimum-norm algorithms in resolving plane waves in noise," *IEEE Trans. Acoust., Speech, Signal Processing*, vol. ASSP-34, pp. 331–340, Apr. 1986.

[28] Krim, H. and Viberg, M., "Two decades of array signal processing research: the parametric approach," *IEEE Signal Processing Mag.*, pp. 67–94, July 1996.

[29] Krolik, J. and Swingler, D., "Focused wideband array processing by spatial resampling," *IEEE Trans. Acoust., Speech, Signal Processing*, vol. 38, pp. 356–360, Feb. 1990.

[30] Krolik, J. and Swingler, D., "Multiple wide-band source location using steered covariance matrices," *IEEE Trans. Acoust., Speech, Signal Processing*, vol. 37, pp. 1481–1494, Oct. 1989.

[31] Lake, D., "Harmonic phase coupling for battlefield acoustic target identification," in *Proc. IEEE Acoustics, Speech, and Signal Processsing (ICASSP'98)*, (Seattle, WA), May 1998.

[32] Lee, T.-S., "Efficient wide-band source localization using beamforming invariance technique," *IEEE Trans. Signal Processing*, vol. 42, pp. 1376–1387, June 1994.

[33] Lehman, S. and Devaney, A., "Transmission mode time-reversal super-resolution imaging," *J. Acoust. Soc. Am.*, vol. 113, pp. 2742–2753, May 2003.

[34] Oh, S.-M. and McClellan, J., "Multiresolution quadtree beamformer," in *IEEE Int. Conf. Acoustics, Speech, and Signal Processsing*, (Orlando, FL), 2002.

[35] Oh, S.-M. and McClellan, J., "Multiresolution imaging with the quadtree backprojection," in *Proc. Asilomar Conference on Signals, Systems and Computers*, Nov. 1983.

[36] Oppenheim, A. and Schafer, R., *Discrete-time Signal Processing*. Upper Saddle River, NJ: Prentice Hall, 1999.

[37] Ottersten, B. and Kailath, T., "Direction-of-arrival estimation for wide-band signals using the ESPRIT algorithm," *IEEE Trans. Acoust., Speech, Signal Processing*, vol. ASSP-38, pp. xxx–yyy, Feb. 1990.

[38] Peebles, P., *Radar Principles*. New York, NY: John Wiley and Sons, 1998.

[39] Rau, R. and McClellan, J., "Analytic models and postprocessing techniques for UWB SAR," *IEEE Trans. Aerosp. Electron. Syst.*, vol. 36, pp. 1058–1074, Oct. 2000.

[40] Roy, R. and Kailath, T., "ESPRIT-estimation of signal parameters via rotational invariance techniques," *IEEE Trans. Signal Processing*, vol. 37, pp. 984–995, July 1989.

[41] Schmidt, R., "Multiple emitter location and singal parameter estimation," *IEEE Trans. Antennas Propagat.*, vol. AP-34, pp. 276–280, Mar. 1986.

[42] Schröder, C., *On the Interaction of Elastic Waves with Buried Land Mines: An Investigation Using the Finite-Difference Time-Domain Method*. PhD thesis, Georgia Institute of Technology, Atlanta, Georgia, 2001.

[43] Schwarz, G., "Estimating the dimension of a model," *The Annals of Statistics*, vol. 6, pp. 461–464, Mar. 1978.

[44] Sidiropoulos, N., Bro, R., and Giannakis, G., "Parallel factor analysis in sensor array processing," *IEEE Trans. Signal Processing*, vol. 48, pp. 2377–2388, Aug. 2000.

[45] Stoica, P. and Moses, R., *Introduction to Spectral Analysis*. Upper Saddle River, NJ: Prentice Hall, 1997.

[46] Stoica, P. and Nehorai, A., "MUSIC, maximum likelihood, and Cramer-Rao bound," *IEEE Trans. Acoust., Speech, Signal Processing*, vol. 37, pp. 720–741, May 1989.

[47] Strang, G., *Linear Algebra and Its Applications*. Thomson Learning, 1988.

[48] Strobach, P., "Bi-iteration multiple invariance subspace tracking and adaptive ESPRIT," *IEEE Trans. Signal Processing*, vol. 48, pp. 442–456, Feb. 2000.

[49] Su, G. and Morf, M., "The signal subspace approach for multiple wideband emitter location," *IEEE Trans. Acoust., Speech, Signal Processing*, vol. ASSP-31, pp. 1502–1522, Dec. 1983.

[50] Swindlehurst, A., Ottersten, B., Roy, R., and Kailath, T., "Multiple invariance ESPRIT," *IEEE Trans. Signal Processing*, vol. 40, pp. 867–881, Apr. 1992.

[51] Swingler, D. and Krolik, J., "Source location bias in the coherently focused high-resolution broad-band beamformer," *IEEE Trans. Acoust., Speech, Signal Processing*, vol. 37, pp. 143–145, Jan. 1989.

[52] Trees, H. V., *Optimum Array Processing*. New York: John Wiley, 2002.

[53] Valaee, S., Champagne, B., and Kabal, P., "Localization of wideband signals using least-squares and total least-squares approaches," *IEEE Trans. Signal Processing*, vol. 47, pp. 1213–1222, May 1999.

[54] Valaee, S. and Kabal, P., "Wideband array processing using a two-sided correlation transformation," *IEEE Trans. Signal Processing*, vol. 43, pp. 160–172, Jan. 1995.

[55] Valaee, S. and Kabal, P., "The optimal focusing subspace for coherent signal subspace proceesing," *IEEE Trans. Signal Processing*, vol. 44, pp. 752–756, Mar. 1996.

[56] Viberg, M. and Ottersten, B., "Sensor array processing based on subspace fitting," *IEEE Trans. Signal Processing*, vol. 39, pp. 1110–1121, May 1991.

[57] Viberg, M., Ottersten, B., and Kailath, T., "Detection and estimation in sensor arrays using weighted subspace fitting," *IEEE Trans. Signal Processing*, vol. 39, pp. 2436–2449, Nov. 1991.

[58] Wang, H. and Kaveh, M., "Coherent signal-subspace processing for the detection and estimation of angles of arrival of multiple wide-band sources," *IEEE Trans. Acoust., Speech, Signal Processing*, vol. ASSP-33, pp. 823–831, Aug. 1985.

[59] Wang, H. and Kaveh, M., "On the performance of signal-subspace processing-part ii: coherent wide-band systems," *IEEE Trans. Acoust., Speech, Signal Processing*, vol. ASSP-35, pp. 1583–1591, Nov. 1987.

[60] Wax, M. and Kailath, T., "Determining the number of signals by information theoretical criteria," in *Proc. ASSP Spectrum Estimation Workshop II*, (Tampa, FL), pp. 192–196, 1983.

[61] Wax, M. and Kailath, T., "Spatio-temporal spectral analysis by eigenstructure methods," *IEEE Trans. Acoust., Speech, Signal Processing*, vol. ASSP-32, pp. 817–827, Aug. 1984.

[62] Win, M. and Scholtz, R., "Ultra-wide bandwidth time-hopping spread-spectrum impulse radio for wireless multiple-access communications," *IEEE Trans. on Communications*, vol. 48, pp. 679–691, Apr. 2000.

[63] Yoon, Y.-S., Kaplan, L., and McClellan, J., "Pruned multi-angle resolution fast beamforming," in *Proc. IEEE Sensor Array and Multichannel Signal Processing Workshop (SAM'02)*, (Rosslyn, VA), pp. 490–494, Aug. 2002.

[64] Yoon, Y.-S., Kaplan, L., and McClellan, J., "Direction-of-arrival estimation of wideband signal sources using multiple subarrays," in *ARL CTA Symposium*, (College Park, MD), Apr. 2003.

[65] Yoon, Y.-S., Kaplan, L., and McClellan, J., "New signal subspace direction-of-arrival estimator for wideband sources," in *IEEE Int. Conf. Acoustics, Speech, and Signal Processsing*, (Hong Kong), Apr. 2003.

[66] Yoon, Y.-S., Kaplan, L., and McClellan, J., "Direction-of-arrival estimation of wideband signal sources using arbitrary shaped multidimensional arrays," in *IEEE Int. Conf. Acoustics, Speech, and Signal Processsing*, (Montreal, Canada), May 2004.

[67] Yoon, Y.-S., Kaplan, L., and McClellan, J., "Error analysis of the pruned multi-angle resolution beamformer," in *Digital Signal Processing Workshop*, Oct. 2002.

[68] Yoon, Y.-S., Kaplan, L., and McClellan, J., "Pruned multi-angle resolution fast beamforming," in *Sensor Array and Multichannel Signal Processing*, Aug. 2002.

[69] Zatman, M., "How narrow is narrowband?," *IEE Proc.-Radar, Sonar Navig.*, vol. 145, pp. 85–91, Apr. 1998.

[70] Zhang, Q., "Probability of resolution of the MUSIC algorithm," *IEEE Trans. Signal Processing*, vol. 43, pp. 978–987, Apr. 1995.

[71] Zoltowski, M., Kautz, G., and Silverstein, S., "Beamspace Root-MUSIC," *IEEE Trans. Signal Processing*, vol. 41, pp. 344–364, Jan. 1993.

VITA

Yeo-Sun Yoon was born in Seoul, Korea on May 4, 1972. He received Bachelor degree from Yonsei University, Seoul, Korea in 1995 and Masters degree from the university of Michigan, Ann Arbor in 1998, both in Electrical Engineering. In 1999, he went to Georgia Tech where he received PhD degree in 2004 from the school of Electrical and Computer Engineering. His research interest includes general array signal processing and detection and estimation techniques.